UNIVERSITY OF LIVERPOOL

ELUCIDATING THE STRUCTURE OF PEPTIDE SELF-ASSEMBLED MONOLAYERS ON GOLD NANOPARTICLES

Thesis submitted in accordance with the requirements of the University of Liverpool for the degree of Doctor in Philosophy

by

ELENA COLANGELO

September 2016

Ithaka gave you the marvelous journey.
Without her you would not have set out.

K. P. Kavafis, *Ithaka*, 1911

To my parents.

ACKNOWLEDGMENTS

First and foremost, I wish to thank my supervisors at the University of Liverpool, Raphaël Lévy and Martin Volk for their support, patience and guidance throughout these four years, even when I was struggling 7,000 miles away. I would like to say thank you to Raphaël not only for his guidance, but also for his inspiring views on science. A sincere thank you to Martin for his work and selfless enthusiasm that have contributed to the good outcome of this thesis and kept me motivated. I would like also to thank all members of Raphaël's group, old and new, especially Joan, Lara, Dan, Alex and Changye.

I also wish to thank my supervisor at the A*STAR Institute of Materials Research and Engineering (IMRE) in Singapore, David Paramelle, not only for his help and encouragements, but also for his friendship during my time there. I also thank Michael Sullivan for the rewarding collaboration at the A*STAR Institute of High Performance Computing (IHCP) in Singapore, but especially CHEN Qiubo for introducing me to molecular dynamics and because I really enjoyed working and learning from him.

I heartily thank my lunch buddies, each of them and all of them because my time in Liverpool would not have been the same without Friday treats, the banter and the ciders in AJ and of course, Krazy House. I thank Michael, for his superb skills at understanding me and translating for the others and for introducing me to Spaced; James, for some of the best conversations ever at lunch time and for the delightful chats in the office; Dominic, for his witty jokes, for asking for the Strokes at my leaving dos and for cheering me up the day before my departure to Singapore; Gaz, for making things look simple and straightforward; Edward, for being a lad yet someone I can count on, and becoming a friend in the meantime.

I would like to thank the people who were an important part of this journey, even if just for a bit. Andrea, for the extraordinary friendship and the myriad of good moments that we had together around the world. Tommas(in)o, for being my mind's safe haven all the way through this PhD, from the irradiation and f5 times up to now. Mohamed, for the insightful conversations at night time, for being caring, for the nights spent watching Bollywood movies and eating praline ice cream and for making me want to travel to India. David, for the support and for being exceptionally present every day of my second time in Singapore. Quentin, because he was right when saying I did not need to worry.

I would like to thank the Singapore crew: Davide and Serena, Alessandro, Teresa, Aled and Ann, Sam, Ola, Anna, for the exploring times as well as the supportive times. I also thank Gary, Dora and Zilu for the insightful and eye-opening conversations about Singapore.

I would also like to thank Liam, who tiptoed into my life when I thought there was no room for anyone, for the spontaneous times and making me look forward to the post PhD with a whole new perspective.

Finally, I would like to thank my family, especially my Mum and Dad, for never asking me to come back or considering giving up as an option; without their continual and unconditional support I would not have gotten to see land. I also thank my grandmothers, my auntie and uncle for the endless love.

My four years of PhD between Liverpool and Singapore have been extremely revealing and changed my way of thinking and seeing myself.

ELUCIDATING THE STRUCTURE OF PEPTIDE SELF-ASSEMBLED MONOLAYERS ON GOLD NANOPARTICLES

ELENA COLANGELO

Submitted for the degree of Doctor in Philosophy

September 2016

ABSTRACT

Controlling gold nanoparticles (GNPs) surface chemistry is a fundamental prerequisite to tailor their properties and envision their assembly into complex nanomaterials from a "bottom-up" approach. Short peptides have been specifically designed to form self-assembled monolayers on GNPs surface and used to increase their stability. However, their structural characterization is often poorly investigated and challenging to assess. This body of work examines different approaches to elucidate the structure and organization of peptide self-assembled monolayers on GNPs. First, the current knowledge and the methods available to characterize the GNPs surface are reviewed. Second, the attempt at using benzophenone-derivative peptides, to provide insights into the molecular organization and compactness of mixed monolayers self-assembled on GNPs, is reported. Under irradiation at 350 nm, the carbonyl group of the benzophenone moiety crosslinks to an adjacent molecule. However, the photo-cross-linking reaction, monitored by FTIR spectroscopy in solution, was not detected on the GNPs surface. Third, to probe the accessibility of a functional group at the GNPs surface, fluorescently labelled peptides, quenched when bound to the gold surface, and bearing a cleavage site for thrombin enzyme at different positions along the chain, were inserted into different peptide self-assembled monolayers on GNPs. The timings of the increase in fluorescence, upon cleavage by thrombin, probed the accessibility, and hence the molecular environment, of the site within the different monolayers investigated. Fourth, a computational model for peptide-capped GNPs was developed using experimentally characterized CALNN- and CFGAILSS-capped GNPs as a benchmark. The molecular dynamics simulations not only reproduced the experimentally observed dependence of the monolayer secondary structure on peptide capping density and on nanoparticle size, but provided also further insights into the monolayers and inter-peptide interactions at the molecular level.

TABLE OF CONTENTS

CHAPTER 1

TOPICAL REVIEW: CHARACTERIZING SELF-ASSEMBLED MONOLAYERS ON GOLD NANOPARTICLES

1.1 Preface

As introduction to this body of work, a Topical Review to be submitted to *Bioconjugate Chemistry* for the Issue 1 of 2017 is reported. It recapitulates the current knowledge and the methods available to characterize self-assembled monolayers on gold nanoparticles.

The elucidation of the structure and molecular organization of peptide self-assembled monolayers on gold nanoparticles is indeed the thread connecting all the investigations reported in this thesis.

In particular, in the experimental Chapter 2 and 3, the versatility of peptides was exploited to insert the benzophenone photo-activable molecule and a thrombin cleavage site (together with a fluorophore at the C-terminal) at different positions along the chain, respectively. In Chapter 2, upon UV-irradiation, the detection by FTIR spectroscopy of the benzophenone moiety cross-linked to an adjacent ligand or solvent molecule was meant to probe the molecular organization and compactness of a mixed self-assembled monolayer on gold nanoparticles. In Chapter 3, the accessibility of thrombin cleavage site at the surface of GNPs functionalized with different monolayers was demonstrated to be extremely sensitive to the precise position and surrounding environment by fluorescence measurements. In Chapter 4 a computational model, developed using CALNN- and CFGAILSS-capped gold nanoparticles, experimentally characterized with structural biology techniques, was validated on the basis of the experimental findings and thus, demonstrated to predict the secondary structure of peptide self-assembled monolayers on gold nanoparticles.

1.2 Characterizing Self-Assembled Monolayers on Gold Nanoparticles

Elena Colangelo,[a] Joan Comenge,[a] David Paramelle,[b] Martin Volk,[c,d] Raphaël Lévy[a,*]

[a]Institute of Integrative Biology, University of Liverpool, Crown Street, L69 7ZB Liverpool, United Kingdom

[b]Institute of Materials Research and Engineering, A*STAR (Agency for Science, Technology and Research), 2 Fusionopolis Way, #08-03 Innovis, Singapore 138634

[c]Department of Chemistry, University of Liverpool, Liverpool L69 7ZD, United Kingdom

[d]Surface Science Research Centre, Department of Chemistry, Abercromby Square, University of Liverpool, Liverpool L69 3BX, United Kingdom

ABSTRACT: A key aspect of nanoscience is to control the assembly of complex materials from a "bottom-up" approach. The self-assembly and self-organization of small ligands at the surface of nanoparticles represent a possible starting route for the preparation of (bio)nanomaterials with precise (bio)physical and (bio)chemical properties. However, surface characterization and elucidation of the structure-properties relationship, essentials to envision such control, remain challenging and are often poorly investigated. This Topical Review aims to discuss different levels of surface characterization, giving an overview of the experimental and computational approaches that are used to provide insights into the self-assembled monolayer with molecular details. The methods and strategies discussed focus on the characterization of self-assembled monolayers at the gold nanoparticle surface, but most of them could also be applied to other types of nanoparticles.

1. Introduction

The Bakerian Lecture given by Michael Faraday in 1857, describing for the first time the interaction of metal particles with light, has been a milestone in the development of the modern science of gold colloids.[1,2] The enticement of gold nanoparticles (GNPs) resides in the way their free electrons interact with light,[3] revealing both their and the environment's properties, together with the ease of synthesis[4,5] and functionalization with small ligands.[6] Thus, small thiolate ligands, including alkylthiols,[7] peptides,[8] oligonucleotides,[9,10] and polyethylene glycols,[11] bind readily to the surface and form self-assembled monolayers (SAMs),[7] imparting both stability[12,13] and desired functionality[14,15] to the nanoparticles. However, even though the literature is abounding with examples of functionalized gold nanoparticles for applications in biology,[16] catalysis[17] and sensing,[18] usually illustrated with inspiring schemes, the actual structure and organization of the SAMs at the gold na-

noparticle surface are challenging to assess and remain often poorly characterized. Such elucidation is a fundamental prerequisite to warrant data reproducibility and build knowledge of predictable properties on the basis of the nanomaterials' characteristics. Moreover, the investigation of the relationship between structure and function is necessary to fully exploit the possibility of engineering nano-objects with well-defined (bio)physicochemical and structural properties from a "bottom-up" approach, which could then be assembled into complex networks, potentially taking inspiration from nature.[19,20]

Starting from basic properties, such as overall chemical composition and thickness, and progressing to more advanced insights, such as molecular structure and phase separation of ligands, we review the current knowledge and the methods available to characterize these systems.

As the Topical Review is organized according to self-assembled monolayer properties, the same studies may appear in different sections. Overall, this Topical Review aims to highlight the web of connections existing between the different self-assembled monolayer characteristics.

2. Basic Characterization and Composition

As mentioned in the introduction and also highlighted in previous reviews,[7,21] many scientific articles lack basic characterization of functionalized GNPs. Thus, in this section, some of the chemical and analytical approaches and techniques adopted to characterize a SAM on GNPs and shed light on its composition are recapitulated.

Once the GNPs are synthesized, the stabilizing molecules at the surface, e.g., citrate ions[4] or simple thiols,[5] can be replaced by another thiol-containing molecule in a ligand exchange reaction, following a bimolecular nucleophilic substitution mechanism.[22] The stabilizing molecules ensure colloidal dispersion of the GNPs, typically by electrostatic (charged ligands) and/or steric repulsion (bulky ligands).

Scheme 1 lists the most common experimental methods used to characterize the ligands bound to the nanoparticle surface, which will be discussed throughout this Topical Review. Such methods can be divided into those that analyze directly the ligand-capped GNPs and those that require the release of the ligands.

The first category includes UV-visible spectrophotometry. Indeed, GNPs larger than 2 nm in diameter are characterized by the surface plasmon band (SPB),[23] theoretically described by Mie in his work dating from 1908;[24] the position of the

SPB maximum is deeply influenced by the GNP size and shape and the dielectric constant of the surrounding environment. Hence, the presence of ligands anchored onto the surface can be indirectly probed by a shift in the SPB maximum detected simply by UV-vis spectrophotometry.

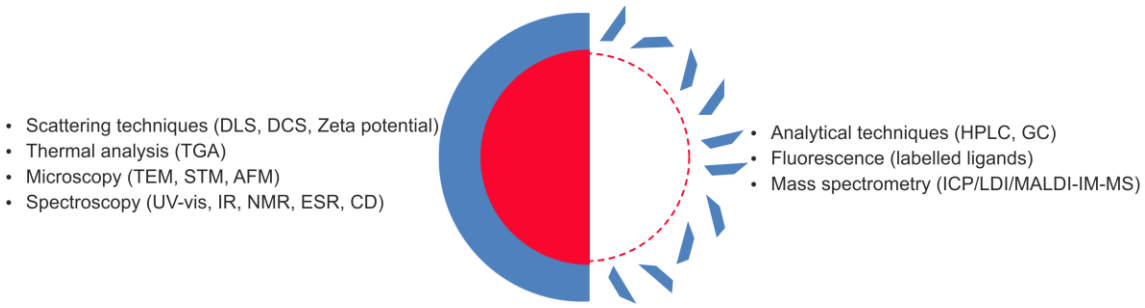

Scheme 1. Examples of experimental methods used to characterize the GNP' surface, analyzing ligand-capped GNPs (left) or ligands released upon gold decomposition or ligand exchange (right).

Also, indirect evidence of functionalization can be obtained from the increased colloidal stability in high ionic strength media that otherwise would lead to complete particle-to-particle aggregation, i.e., red-shift and broadening of the SPB.[25] Weisbecker et al., for instance, investigated the effect of capping citrate GNPs with alkanethiols of different chain lengths and terminal functional groups in various conditions of pH and ionic strength by monitoring the absorbance spectra over time;[26] Lévy et al. observed a 2 nm red-shift and protection to salt-induced aggregation resulting from the conjugation of the CALNN pentapeptide to citrate GNPs (Figure 1A).[8] Duchesne et al. observed different GNP stability against electrolyte-induced aggregation and ligand exchange upon varying the ligand concentration during the conjugation process, thus providing an indirect measurement of the ligand capping density on GNPs.[12] Evaluation of the resistance of capped GNPs to increasing concentrations of dithiotreitol, i.e., ligand exchange, was used to select combinations of ligands forming highly compact SAMs on GNPs, hence providing high stability in biological environments.[13] Similarly, indirect estimation of the capping density was gathered by Schulz et al. from assessing the resistance to cyanide etching of GNPs capped with SAMs constituted of PEG-thiol ligands with the same chain length, but progressively larger segments between the thiol group and the polymer moiety (Figure 1B).[27]

Furthermore, differential centrifugal sedimentation[28] (DCS) or dynamic light scattering (DLS) and zeta (ζ) potential measurements[29] are used to determine the hydrodynamic diameter and the charge of the ligand-capped GNPs, respectively, thus giving insight into their stability and properties, such as protein[30] or molecule[31] adsorption. Thermal gravimetric analysis (TGA), by monitoring changes in weight over a temperature ramp, gives an indication of the amount of ligands on the GNPs, but requires 1-10 mg of sample and assumptions and modelling for the shape of the gold cores.[32] IR and NMR spectroscopies are generally used not only to characterize the content of SAMs on GNPs, but also to investigate their structure and interactions existing between the ligands; thus, they will be further discussed in Section 4.

Examples of analytical methods to identify and quantify the amount of ligands upon cleavage from the GNPs surface include Zhou et al.'s work where SAMs constituted of up to three different ligands were first cleaved from the NP surface with I_2,[33] then identified with mass spectrometry and quantified by high-performance liquid chromatography with UV or chemiluminescent nitrogen detection (HPLC/MS/UV/CLND), using calibration curves constructed from the free ligands.[34] This provided a method to confirm the common assumption that the ratio of ligands on the GNP surface is the same as the one used during the conjugation process (Figure 1C). However, as Fisher et al. pointed out, this method is limited to disulfide ligands, since I_2 exposure leads to disulfide product formation.[35] Fisher et al. developed a method to quantify the amount of non-disulfide alkanethiol ligands in mixed SAMs on 2 nm GNPs using gas chromatography coupled to mass spectrometry (GC/MS/MS), upon I_2 exposure, and using a calibration curve constructed from free disulphide mixtures; ^{1}H-NMR spectroscopy was employed as an additional technique to corroborate their findings.[35] Hinterwirth et al.[36] described a method to determine the ligand capping density on the basis of the observed linear relationship between the NP diameter, measured by transmission electron microscopy (TEM), and the ratio between gold and sulfur atoms, measured by inductively coupled plasma mass spectrometry (ICP-MS), a powerful technique for elemental analysis.[37] The number of peptide ligands can also be measured using amino acid analysis.[8,12]

To quantify the amount of alkanethiol-oligonucleotides capping a GNP, Demers et al. modified the ligand by fluorescently labelling it, and then, after conjugation to the GNPs and removal of the ligand excess, incubated the capped GNPs in the presence of another thiolate ligand.

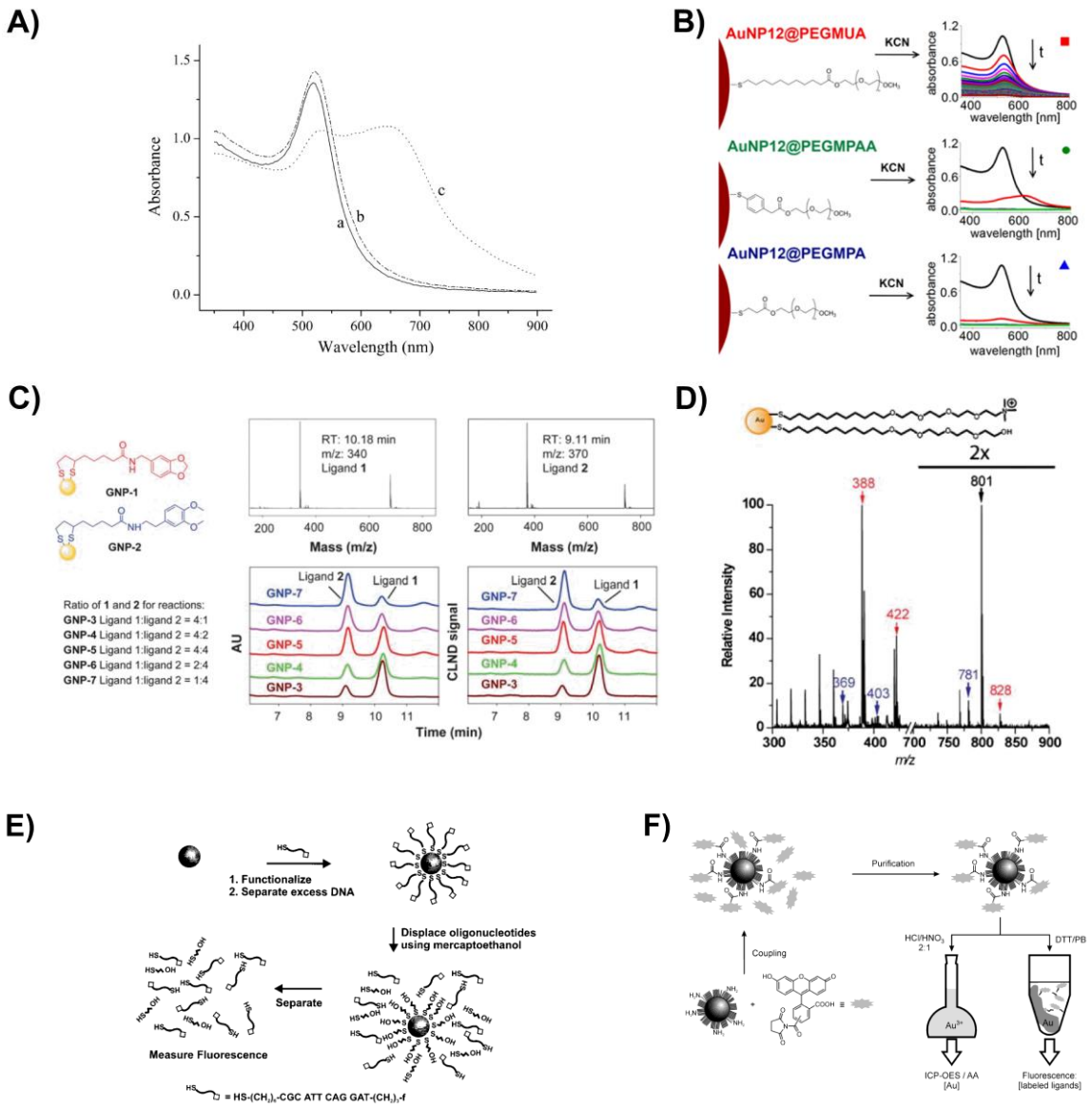

Figure 1. Measurements of the presence and composition of SAMs on GNPs; using GNP optical properties: A) UV-vis spectra of citrate GNPs before (a) and after addition of a volume of CALNN peptide (b) or phosphate-buffered saline (c) (Reprinted from ref. 8), B) Schematic drawings and UV-vis spectra recorded in 5- (top) or 2- (middle-bottom) min steps of differently capped 12 nm GNPs before (black lines) and after addition of KCN (Reprinted from ref. 27); using mass spectrometry techniques: C) Mass spectra of the thioctic acid ligands (shown on the left) cleaved from the GNPs and quantified by HPLC using two detectors (adapted from ref. 34), D) LDI-MS spectra of a mixed SAM on GNPs showing ions corresponding to both ligands (in blue and red) and mixed disulphide ions (in black) (Adapted from ref. 38); using fluorescence: E) GNPs functionalized with a fluorescently labelled ligand and purified from its excess. Upon ligand exchange and release of the ligand, the fluorescence is measured and the ligand quantified (Reprinted from ref. 39), F) Upon fluorescence labelling of a reactive group and removal of the fluorophore excess, the GNP concentration is determined by ICP upon dissolution in aqua regia, and the fluorescence corresponding to the amount of reactive group is measured upon ligand exchange (Reprinted from ref. 40).

Thus, the fluorescently labelled oligonucleotides were released by ligand exchange and quantified using fluorescence, based on calibration curves made from the free fluorescently-labelled ligand in solutions of same pH and ionic strength (Figure 1E).[39] The ligand exchange reaction was confirmed to be completed by an independent method, where the GNPs were dissolved by cyanide and the increase in fluorescence, associated with the fluorophore being released, monitored. Maus et al. used a similar method to quantify something conceptually different, i.e., the average amount of functionalizable reactive groups per GNP, where the GNPs were capped with a mixed SAM constituted of a ω-carboxylate and ω-amino thiols; the last one functionalizable with a fluorescently labelled NHS ester derivative (Figure 1F).[40]

Functionalized GNPs can also be characterized by laser desorption ionization mass spectrometry (LDI-MS).[41–43] The use of this technique for characterizing nanoparticles originates from Tanaka et al.'s work,[44] demonstrating the ability of metal nanoparticles to absorb laser light energy and thus desorb analytes and enhance their ionization. For instance, Yan et al. characterized GNPs capped with positively or negatively charged and neutral ligands by LDI-MS: in all cases, both thiol and disulphide ions were detected.[38] Moreover, when analyzing GNPs functionalized with two different ligands, not only thiol and disulphide ions corresponding to both ligands were identified, but also mixed disulphide ions (Figure 1D). The authors developed a procedure to provide a semi-quantitative measurement of two ligands on GNPs; since different ionization efficiencies are associated to different ligands, NMR spectroscopy was used as external technique for calibration.

Cliffel and McLean's group developed a strategy coupling MALDI to ion mobility-mass spectrometry (IM-MS), a gas-phase separation technique, to provide a measurement of the relative quantities of two ligands in a mixed SAM on GNPs.[45] This technique is more advantageous than NMR spectroscopy, since it does not require the two ligands to have different functionalities. Also, unlike traditional MS, IM is able to separate ions corresponding to clusters of gold atoms and ligands from those corresponding to ligands alone, thus proving that the ligands were actually attached to the GNP surface.

3. Compactness and Thickness

As discussed in the previous section, different approaches have been proposed in the literature to determine the amount of ligands on GNPs, hence the capping

density. Whilst not independent of the capping density, the SAM compactness and thickness also depends on the conformation of the ligands and on the amount of solvent present within the SAM. In this section, direct and indirect methods providing insights into these characteristics are detailed.

The compactness of a SAM does not only result from the number of ligands on the GNPs surface; Chen et al. have indeed reported the extremely high stability against ligand exchange of SAMs constituted of peptidols with aromatic amino acids, i.e., H-CFFFY-ol or H-CFFFT-ol, and PEGylated alkanethiol, indicating that aromatic and alkyl chains can form extremely compact SAMs through hydrophobic interactions and, possibly, well-defined secondary structure motifs.[13] Duchesne et al. highlighted that higher SAM compactness can be achieved by using modified peptides, i.e., peptidols, which bear a non-ionisable primary alcohol group, instead of a carboxyl group, at the C-terminus.[12] Schulz et al., as previously mentioned, probed the effect which segments of different sizes between the thiol group and a polymer chain had on protecting the GNPs from cyanide etching.[27] They showed that ligands with smaller spacers were leading to higher capping density, hence higher compactness and stability to etching (Figure 1B).

The packing of a SAM can be measured more directly via its thickness, which, however, can be challenging to assess. Since GNPs are electron dense materials, they have been used for over 60 years as contrast agents in transmission electron microscopy (TEM).[46] Even though TEM is mostly only used to size the gold cores only, Jürgens et al. measured the thickness of films of proteins adsorbed on GNPs with this technique.[47] Ardao et al. imaged by TEM samples of enzyme-adsorbed GNPs, not purified from the excess of enzyme, using the negative staining method.[48] The agent, by staining the enzymes' surface, conferred a grey background to the images. Since the enzymes at the GNPs' surface were highly packed and thus did not get stained, the ligand shells appeared as white rings in the TEM images. However, considering the drying of the sample and the often insufficient contrast, TEM images cannot provide quantitative information on the thickness of SAMs in solution.

As mentioned in Section 2, dynamic light scattering (DLS) is a common method to determine the hydrodynamic diameter of GNPs.[29] Its value depends on the length of the ligands and the compactness of the monolayer. Therefore, changes of these parameters can be reflected by DLS measurements. However, small changes in the hydrodynamic diameter (<5%) cannot be detected by DLS. Walkey et al., for instance, assessed by DLS the hydrodynamic volume occupied by one poly(ethylene

glycol) (PEG) molecule in SAMs of different capping densities on GNPs of different sizes.[49] Smaller volumes were found for higher capping densities, indicating both strengthening and dehydration of the ligands. On the other hand, for a given capping density, a larger volume was found for smaller GNPs, which was rationalized with the fact that a decrease in GNP size, i.e., an increase of curvature, frustrates the hydrophobic interactions between the PEG chains (Figure 2A). Belsey et al. described two approaches to measure the thickness and the number of either adsorbed proteins or conjugated peptides on GNPs of different sizes.[50] The first approach involved UV-Vis spectroscopy to indirectly prove the adsorption/conjugation of the biomolecules to the GNPs, by monitoring the surface plasmon band, DLS to measure the thickness of the monolayers, and differential centrifugal sedimentation (DCS) to prove the monodispersity of the GNPs. The second approach employed x-ray photoelectron spectroscopy (XPS) to measure the monolayer thickness in ultra-high vacuum. The authors concluded that in spite of the intrinsic differences between the two approaches, the results appeared to be consistent. Falabella et al.[51] and Krpetić et al.[28] highlighted the advantages of using analytical ultracentrifugation (AUC) techniques, determining the GNPs' sedimentation coefficients, as compared to DLS. In particular, contrarily to DLS, AUC measurements are not perturbed by the presence of small GNPs aggregates, which, in the case of DLS, would potentially dominate the analysis. Falabella et al. characterized GNPs of different sizes, functionalized with thiol-terminated single stranded DNA, to investigate the effect of capping density and chain length;[51] Krpetić et al. measured the shell thickness of a range of PEG-thiol and peptide ligands on GNPs of different sizes (Figure 2B).[28]

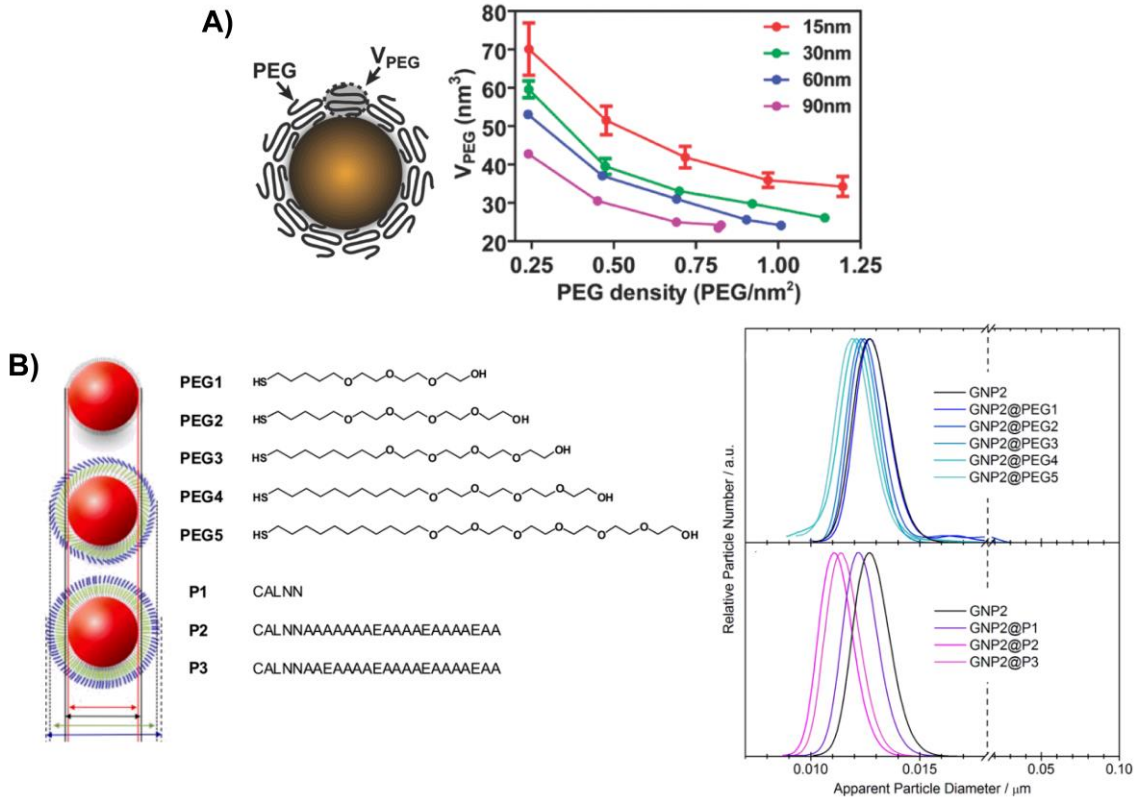

Figure 2. Compactness and thickness of SAMs on GNPs. A) Schematic representation and PEG chain hydrodynamic volume (V_{PEG}) determined by dynamic light scattering (DLS) as a function of PEG capping density on GNPs of different sizes (Adapted from ref. 49); B) Normalized number size distributions of the GNPs illustrated on the left and capped with different ligands. Analysis by differential centrifugal sedimentation (DCS) shows a shift to smaller apparent diameter with the increase in ligand shell thickness, which can be corrected, so that the actual shell thickness is obtained (Adapted from ref. 28).

4. Conformation

As discussed in the previous section, measurement of the SAMs' thickness and compactness also provides insights into the underlying ligands' conformation. However, determining the structure of ligand-capped GNPs at the molecular level remains highly challenging.

The work by Jadzinsky et al., dating from 2007, marked a breakthrough in terms of structural information on GNPs.[52] The authors determined the crystal structure at 1.1 Å resolution of *p*-mercaptobenzoic acid-capped 1.5 nm gold clusters and thus, shined light on the structure and geometry of a thiol monolayer. Also, for the first time, the atomic structure of the gold-thiol bond was revealed: each sulfur atom was found to bind to two gold atoms in a bridge conformation, and at least one gold atom was found to bind to two sulfur atoms. The observed conformation was

called by the authors "staple" motif. Azubel et al., in their work dating from 2014, solved the structure at atomic resolution of a smaller thiol-capped gold cluster by aberration-corrected transmission electron microscopy.[53] In the years in between these two works, capped GNPs in the 1-3 nm range were crystallized, but x-ray diffraction structures with high resolution were not obtained.

Therefore, even though the structures of gold clusters that have been effectively solved provide precious information, other approaches have to be sought to elucidate the conformation of ligands on GNPs larger than 2 nm. Examples of such attempts are described in this section.

Comenge et al. functionalized ~15 nm GNPs with different ratios of 11-mercaptoundecanoic acid (MUA) and thiolated PEG (MW 3.4 KDa) to modulate the biological responses that SAMs of either PEG or alkanethiols on GNPs trigger.[54] Using a combination of UV-vis and DLS techniques, the authors found that the changes in GNP properties were correlated with different PEG conformations. The hydrodynamic radius of the functionalized GNPs was found to suddenly increase at a ratio between PEG and MUA of ~0.7, marking the straightening of the PEG ligands into a brush-like conformation. The blue-shift of the surface plasmon band (SPB) maximum at this ratio corroborated the change in PEG conformation. On this note, Tagliazucchi et al. presented a theoretical method to correlate GNP optical properties to the refractive index of the monolayer (Figure 3A).[55] The model was applied to study the position of the SPB upon collapse, i.e., change in density and hence refractive index, of a thermoresponsive polymeric monolayer on GNPs. The theoretical results were found to well describe the experimental evidence, i.e., the red-shift of the SPB upon polymer collapse and the effect of capping density, chain length and GNP size on the extent of the shift. Xia et al. characterized by DLS gold nanocages with side lengths of 30, 50 and 60 nm, functionalized with PEGs of different molecular weights.[56] The largest hydrodynamic diameter corresponded to the GNPs capped with the PEG molecules of intermediate size. Hence, it was concluded that the SAM constituted of the largest PEGs assumed a mushroom-like conformation, i.e., chains back-folding on the GNPs.

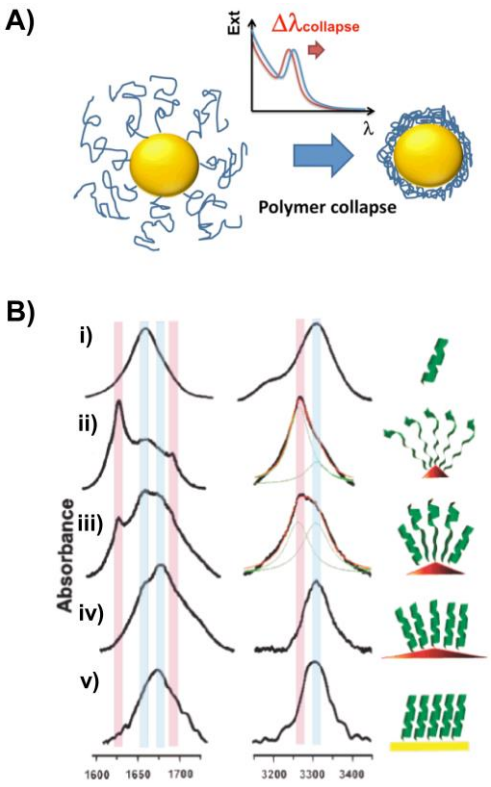

Figure 3. Conformation of SAMs on GNPs. A) Schematic representation of the surface plasmon band red-shift upon collapse of a thermoresponsive polymeric monolayer on GNPs (Reprinted from ref. 55); B) FTIR bands of a Leu-rich peptide (i) free in solution; (ii-iv) Leu-peptide-capped GNPs (5, 10, 20 nm diameter, respectively) and (v) on a planar gold surface. Blue and pink stripes are indicative of α-helix and β-sheet conformations, respectively (Adapted from ref. 57).

Spectroscopic techniques, such as IR and NMR, were cited in Section 2 as means to characterize the composition of SAMs on GNPs. However, these techniques provide information not only about the functionalization and the average ratio of ligands at the GNPs surface, but also about the structure of the ligands within the SAM and the intermolecular interactions existing between them.

Murray and co-workers characterized by FTIR GNPs from 1.5 to 5.2 nm in diameter capped with dodecanethiolate ligand.[32] The IR spectra were taken in solid-phase and allowed the investigation of the alkyl chain conformation. More ordered SAMs, corresponding to a *trans* zigzag structure, similar to the structure observed on planar gold surfaces, were found on the larger GNPs. However, considering the relatively small size of the largest GNPs and that ordered monolayers were already distinguished on 4.4 nm GNPs, the authors investigated the role of sample preparation in such observations. Therefore, the structure of alkanethiols of different chain lengths on ~2 nm GNPs was analyzed by FTIR both in solid-phase and in solution.[33]

It was found that shorter alkanethiols adopted a highly ordered conformation on these 2 nm GNPs in solid-phase, but became quite disordered in carbon tetrachloride, highlighting the importance of the sample preparation, as it can lead to changes in the ligands conformation. Moreover, Murray and co-workers listed the factors determining the broadening of thiolate-capped GNP ^{13}C and ^{1}H NMR spectra.[32,58] Importantly, since both the ligands' proximity to the gold surface and the density of packing contribute to spectral broadening, NMR analysis provides information about the ligands' environment and structural features. The spectra, however, can be difficult to interpret.

Peptide-capped GNPs have been described by us as building-blocks that could potentially be engineered into advanced nanoparticles with protein-like properties.[19] Hence, determining their structures is of crucial importance.

Fabris et al., prepared GNPs of ~1-2 nm size, capped with peptides made of α-aminoisobutyric acid residues.[59] Homooligomers of this residue (starting from the tripeptide) are known to form stiff secondary structure motifs, i.e., β-turns and 3_{10}-helices. IR analysis indicated the presence of 3_{10}-helices, stabilized by intra-peptides hydrogen bonds, both in solution and at the surface of GNPs, independently of the peptide length. Also, the authors judged inter-peptide hydrogen bonds, identified by NMR analysis, to underlie the rigid conformation observed in all the systems investigated. Thus, building-blocks characterized by a stiff monolayer and a precise secondary structure motif were provided. It is worth noting that the IR spectra of the capped GNPs, taken both in solid-phase and in solution, did not show any significant difference.

Shaw et al. investigated the effect of GNP size, i.e., curvature, on the secondary structure of CALNN and CFGAILSS peptide SAMs.[60] The authors used GNPs of 5, 10 and 25 nm in diameter, and a combination of FTIR and solid-state NMR (ssNMR) to elucidate these structures. The CALNN peptide was found to adopt a random coil conformation independent of the GNP size. The CFGAILSS peptide, which arranged in amyloid fibers with an antiparallel β-sheet conformation in solution, formed parallel β-sheets when attached to the gold surface, which were more pronounced on the largest GNPs. Hence, the number of adjacent peptides forming inter-peptide hydrogen bonds and thus, parallel β-sheets, is dictated by the nanoparticle curvature, which agrees well with a simple geometrical model. Moreover, ssNMR directly demonstrated the presence of inter-peptide hydrogen bonds only in the case of CFGAILSS and excluded the interdigitation between GNPs. Similarly, Mandal et al.

capped GNPs of 5, 10 and 20 nm in diameter, with a Leu-rich peptide.[57] FTIR analysis in solid-phase demonstrated the presence of a greater content of α-helix motif on the GNPs with a lower curvature, similar to the one observed for the free peptide or on a planar gold surface, whereas GNPs with high curvature were dominated by β-sheet structures (Figure 3B). The authors suggested that this was due to high capping densities at the edges and corners of GNPs, caused by the high unsaturation of the gold atoms. High capping densities, in turn, allow for the efficient formation of inter-peptide hydrogen bonds which are the prerequisite for forming β-sheet structures. Since in small GNPs, edges and corners dominate over planar faces, more β-sheet structures were found for these, whereas in 20 nm GNPs, binding to planar faces seemed to be predominant, leading to the native α-helical peptide structure. Thus, both works highlighted the importance of GNPs size and ligand sequence when designing nanomaterials with well-defined secondary structure motifs.

On a different note, Rio-Echevarria et al. confirmed by circular dichroism (CD) that the helical secondary structure of an undecapeptide was maintained after conjugation to GNPs of 1-2 nm.[61] However, measuring the CD of larger GNPs in the UV region (to elucidate the conformation of the peptide SAM) can be problematic due to the high absorbance of the gold cores.

5. Organization of Mixed Self-Assembled Monolayers

Since the ratio of ligands at the GNPs surface does not necessarily reflect the one used during conjugation, in Section 2 we summarized some of the efforts made to quantify the ligands constituting a mixed SAM on GNPs. However, questions related to the organization of mixed SAMs on GNPs should also be addressed.

In the 90s, studies of wetting, performed with ellipsometric and goniometric measurements, suggested that two alkanethiols of different chain length and with either a methyl or hydroxymethyl terminal functional group phase-separate on a planar gold surface, forming microscopic islands (Figure 4A).[62] Topological characterization with scanning tunneling microscopy (STM) by Stranick et al.[63] confirmed such phase separation into domains, whose shapes were found to be time-dependent, for two alkanethiols of the same length, but having different non-interacting terminal groups, i.e., methyl and methyl ester, on a gold surface. Tamada et al.[64] studied the segregation of ratios of two alkanethiols of different chain

lengths on gold with atomic force microscope (AFM) and observed clear phase separation.

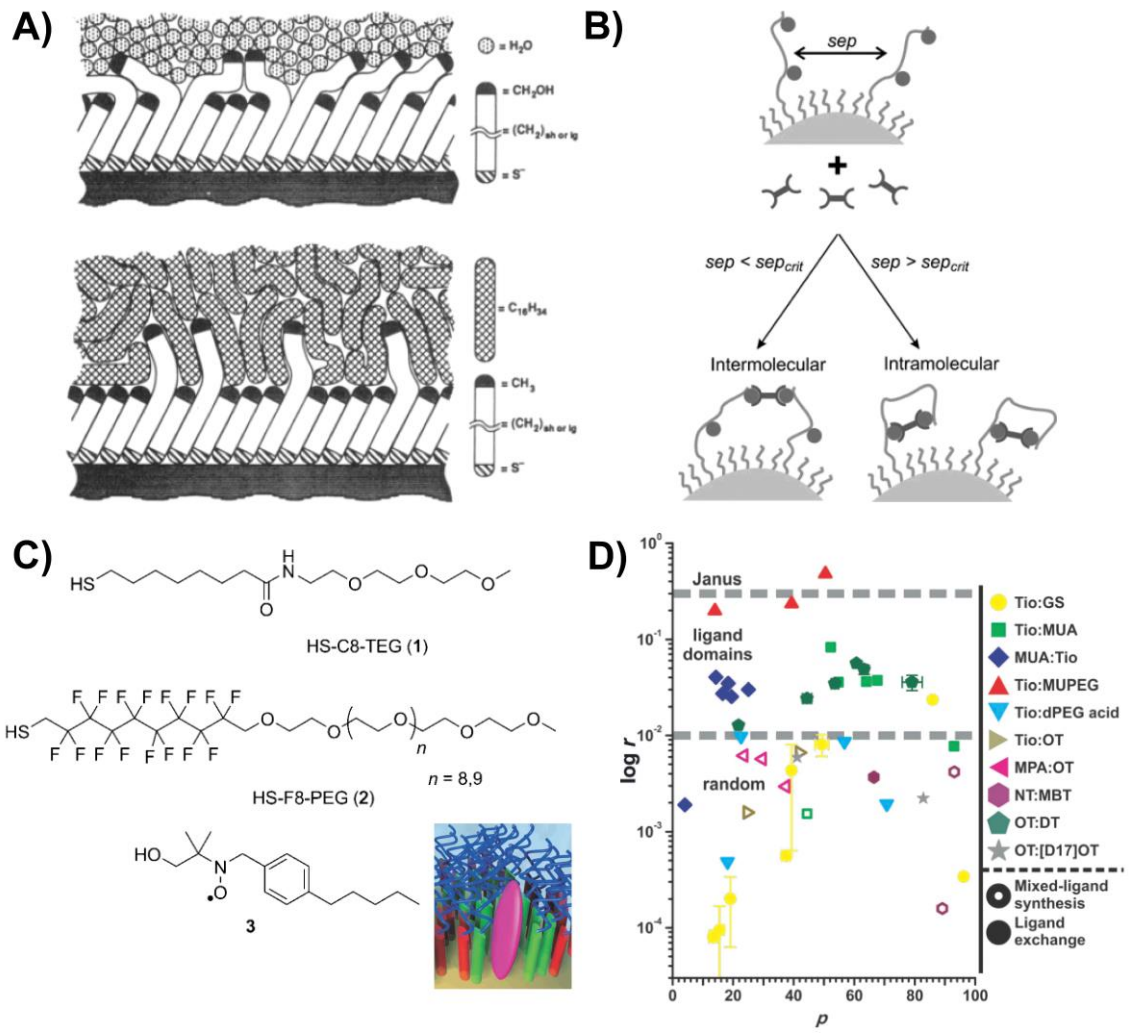

Figure 4. Organization of mixed SAMs. A) Schematized wettability on a planar gold surface of a mixed SAM of alkanethiols of different lengths with an hydroxymethyl or methyl terminal group in water (top) or hexadecane (bottom), respectively (Reprinted from ref. 62); B) Schematized proximity probes in a CALNN monolayer on GNPs forming, depending on their separation, either an inter- or intramolecular cross-link (Reprinted from ref. 65); C) Chemical and conceptualized structures of the ligands constituting the mixed SAM (1,2; red, green) and radical probe (3; magenta) (Adapted from ref. 66); D) Residual sums of squares versus different ratios of ligands for different mixed SAMs on GNPs, prepared following two different procedures, and characterized by MALDI-IM-MS, depicting different types and extents of ligands segregation (Reprinted from ref. 67).

In 2004 Jackson et al.[68] reported the first work on GNPs presenting a stripe-like arrangement of ligands. The authors claimed that STM images of GNPs capped by a mixture of an alkanethiol and a longer thiolate molecule with a terminal carboxylic

acid group demonstrated the presence of ordered domains of 5 Å in size within such SAMs. Moreover, such domains were described as parallel stripe-like patterns circling around the gold cores with shape and size tunable by selecting the composition of the ligand mixture and the GNP size, and with quite alluring properties arising from their small dimensions, such as avoiding the non-specific adsorption of proteins. However, this body of work has been subject of controversy and the published results, re-examined by Cesbron et al.[69] and Stirling et al.,[70] have been suggested to be the result of instrumental artefacts and erroneous analyses. Both of these analyses received a response from the authors of the original publication that addressed the arguments of invalidation of the results obtained.[71,72]

Other approaches to assess the organization of mixed SAMs include Duchesne et al.'s work where GNPs were capped with CALNN and a functional peptide, containing two reactive groups, and acting as a proximity probe.[65] Intermolecular cross-linking between two functional peptides was expected if their separation was lower than 4 nm; if greater, intramolecular cross-linking should have been detected (Figure 4B). Using this method, the authors showed that even if there were only two or three functional peptides on a GNP, they had the tendency to be close to each other on the GNP surface; i.e., they organized in a small domain. This packing was found to form during the self-assembly of the mixed monolayer, and not when the functional peptides were still free in solution. Prins' group used a range of probes to assess the organization of mixed SAMs.[73,74] In a first approach, the SAMs were constituted of different ratios of thiolate ligands with either a cationic or neutral terminal group, where the positively charged group was able to catalyse the transphosphorylation of a substrate, and the apparent catalytic rate constant k_{cat} was used to probe the SAMs' organization.[73] The GNPs' catalytic activity was found to gradually increase up to ligand ratios of ~0.4 and then to remain constant; this increase was ascribed to a random distribution of the ligands within the SAMs. In ref. 74, the same authors discussed the disavantages of k_{cat} as parameter and proposed a general methodology to assess the morphology of a mixed SAM, without the need of a catalytic ligand. A fluorescent anionic probe was used, whose fluorescence is quenched upon interaction with the GNP surface, thus allowing for easy determination of its binding to the cationic ligands, the extent of which depends on the ligands' organization on the GNP surface. A random distribution of the ligands up to ratios of ~0.4 was concluded from both methodologies and was supported by simulated saturation profiles. Gentilini et al. observed a different surface organization

and ordering in mixed SAM on GNPs they investigated. They used a radical probe to assess the organization of mixed SAMs constituted of perfluoroalkyl and alkyl amphiphilic thiolate ligands (Figure 4C) on GNPs by electron spin resonance (ESR) spectroscopy.[66] The radical probe was able to sense the hydrophobicity of the environment and was characterized by different hyperfine splitting constants when sensing a SAM constituted of either perfluoroalkyl or alkyl thiolate ligands. Thus, the authors showed that, up to a ratio of 2.5 between alkyl and perfluoroalkyl ligands, the probe sensed a fluorinated environment, indicating the packing within islands of such ligands.

Cliffel and McLean's group used MALDI coupled to ion mobility-mass spectrometry (IM-MS) to investigate the phase segregation of two ligands in a mixed SAM on GNPs.[67] Upon MALDI analysis, gold-thiolate ions were generated and, once separated from the ligands' ions by IM-MS, the information regarding a particular type of gold-thiolate clusters, i.e., Au_4L_4, was extracted and quantitatively compared to a theoretical model based on the binomial distribution. Using this method, the authors, characterizing several mixed SAMs of different compositions and ratios, observed various degrees of ligands segregation (Figure 4D).

Finally, efforts made to impart different chemical functionalities or polarity to the two hemispheres of an organic or inorganic core are worth mentioning. Such category of micro- and nanoparticles was described for the first time with the term "Janus" by De Gennes in 1991.[75] We refer the reader to past reviews highlighting the various procedures investigated to insert elements of dissymmetry within the monolayer.[76,77] The most common method involves an anisotropic environment, e.g., the interface between air/water or immiscible liquids, that drives the self-organization of a SAM constituted of hydrophilic and hydrophobic ligands.[78,79]

6. Modelling

We refer the reader to a recent review recapitulating the different computational methods available to gather a better description and understanding of the interactions between a gold surface or nanoparticle and the surrounding biological environment.[80] In particular, here we consider the limited insights into the SAM's structure and organization that can be obtained with experimental techniques, and the information about SAMs on GNPs that can be revealed with molecular details using a combination of experimental and computational approaches.

Considering that alkyl thiol-capped GNPs have been investigated since the early '90s, it is not surprising that several classical force fields (FF), describing the interactions of alkyl thiols on gold, are reported in the literature.[81–84] Glotzer and coworkers reported for the first time an atomistic molecular dynamics (MD) study investigating the structure of alkane thiols on gold nanoparticles as a function of temperature, length of the ligand and GNP size; the sulfur atoms were fixed at a distance of 0.238 nm from the gold surface.[85] Ligands with 13 carbons on a 7 nm GNP did not exhibit long-range order at high temperatures, i.e., 900 and 600 K, while they did group into bundles with the same angle to the surface normal at low temperatures, i.e., 450 and 300 K. At 300 K, long-range order was reported only for alkane thiols with more than nine carbons. At high temperatures, the monolayer constituted of the ligands with 13 carbons was found to be more ordered on the larger GNPs, as illustrated by a decrease in the smallest average distance between adjacent terminal groups with an increase in GNP size. Moreover, Glotzer and coworkers performed atomistic and mesoscale (using dissipative particle dynamics) simulations to investigate the morphology of GNPs capped with an equimolar mixture of immiscible alkanethiols, varying the length and the functional terminal group of the ligands, and the GNP size.[86] According to the authors, an increase in conformational entropy was associated with the formation of stripe-like patterns[68] from a Janus arrangement of the ligands. The entropy gain, due to the additional ligand-ligand interfaces, was found to be dependent on the difference in length between the ligands, on the terminal functional groups, and on the GNP curvature. Furthermore, the authors argued that in case of sufficient gain, the stripe-like patterns were corresponding to the morphology at the equilibrium. For instance, while stripe-like patterns were found on GNPs capped with a mixture of ligands with well-defined length ratios or with different terminal functional groups, a Janus organization was observed on small GNPs or in SAMs constituted of two short alkanethiols with small terminal functional groups and similar length.

Velachi et al.[87] and Van Lehn et al.[88] performed atomistic MD simulations at room temperature to elucidate the structural and hydration properties of mixed SAMs constituted of equimolar alkanethiols of different lengths with either a hydrophilic or hydrophobic terminal functional group on GNPs of different sizes. The ligands were fixed through the sulfur atom on the gold surface and arranged in a random or stripe-like or Janus organization. However, Fetisov et al. argued that the structures analyzed in these two studies did not reach the thermal equilibrium over

the time-scales accessed by MD simulations.[89] Thus, in order to analyze thermodynamically equilibrated structures, Fetisov et al. investigated the organization of mixed SAMs constituted of equimolar alkanethiols of different chain length on GNPs of different sizes using Monte Carlo simulations. In contrast to the other studies, the initially imparted random or stripe-like or Janus organization changed over equilibration. SAMs constituted of ligands differing in length by four methylene groups were found in a random organization at room temperature, whereas SAMs constituted of alkanethiols with 6 and 14 carbons did present a Janus arrangement. Moreover, the authors pointed out that a stripe-like organization was only transiently observed during the formation of the Janus arrangement.

Modeling strategies can help elucidating the structure of peptide-capped GNPs and contribute toward the design of new bio-nanomaterials and complex nanosystems. Despite the large number of publications regarding peptide-capped GNPs, not many MD computational studies investigating the SAM structure at the gold surface are reported in the literature. However, it is worth mentioning that the first classical FF, specifically designed for biomolecules on Au(111) surface, dates only from 2008.[90] In this FF and in its implemented version,[91] both the secondary interactions between the amino acids and the gold surface and the gold polarization induced by the biomolecules and surrounding solvent molecules are taken into account.

Simulated peptide-capped GNPs using simpler approximations include Duchesne et al.'s work, where MD simulations were used to assess the volume accessed by a functional peptide embedded in a CALNN monolayer, which was represented by only the C-terminal residues, reproducing a surface with a curvature appropriate for a CALNN layer on a 10 nm GNP.[65] Andresen et al. proposed an immunoassay based on GNPs tagged with peptide epitopes.[92] The authors performed molecular dynamics simulations using a five-layer gold (111) surface to provide insights into the conformation and arrangement of the peptide epitopes on GNPs and propose a mechanism underlying the experimental observations. Todorova et al. investigated the effect of TAT concentration, i.e., a cell-penetrating peptide, on the structure and compactness of a CALNN monolayer anchored through the cysteine sulfur atoms on a 3 nm GNP built from neutral carbon-type atoms.[93] The computational results indicated higher effective diameter of the capped GNP and higher water exposure of the TAT basic residues on GNPs capped with an intermediate TAT concentration. The authors tested the cell internalization of the differently capped GNPs and claimed that TEM images and inductively coupled plasma-atomic emission spectroscopy (ICP-AES)

provided evidence of higher internalization in the case of GNPs capped with an intermediate concentration of TAT, thus validating the properties foreseen by the computational model. A direct validation of the computational findings in terms of the hydrodynamic radius was prevented by the small size of the GNPs, though. Lee et al. looked at the effect that conjugating single peptides of different sequences to 5 nm GNPs had on their structure and dynamics, in comparison to when free in solution.[94]

On a different note, Hamad-Schifferli's group highlighted the importance of measuring both the structure and the function of a protein, after labelling it with a NP.[95] To investigate how NP binding affects protein structure and function, they systematically labelled cytochrome *c* (cyt *c*) by cysteine, mutating surface residues in different positions.[96] Thus, a negatively charged GNP of 1.5 nm diameter, capped with bis(*p*-sulfonatophenyl) phenylphosphine ligand, was covalently bound to cyt *c* through a gold-sulfur bond. The labelling effects on the protein structure were measured by circular dichroism, while MD simulations gave further insights into the structural changes.

7. Conclusions and Perspectives

The ability to control the self-assembly and self-organization of small molecules at the surface of nanoparticles could pave the way to the preparation of nanomaterials with well-defined structural and (bio)physicochemical properties, which could then be envisioned to form more complex systems. Whilst getting a detailed picture remains challenging, a number of characterization techniques are available.

For instance, the optical and electronic properties of the gold core can be exploited to gather indirect evidence of ligand conjugation with UV-vis spectroscopy, whereas, upon ligand removal, separation and mass spectrometry techniques can provide more direct information about the monolayer composition. Scattering techniques can give information about the whole self-assembled monolayer, thus tackling the questions of the nanoparticles' hydrodynamic radius, stability, size dispersion and monolayer thickness. The ligands' conformation is at the basis of these observations and attempts at assessing it involve structural biology techniques, such as NMR and IR spectroscopies; sample preparation procedures have to be carefully taken into account when interpreting the results, though.

However, the level of molecular details that can be obtained with direct methods of characterization is limited. Thus, using a combination of experimental and

theoretical approaches can provide a compelling description of the structure and organization of the monolayer. Nevertheless, advances in both areas of research are critical to work toward the rational design of nanoparticles with precise structural and (bio)physicochemical properties.

Author Information

Corresponding Authors

rapha@liverpool.ac.uk

Notes

The authors declare no competing financial interest.

Acknowledgements

D.P. acknowledges support from A*STAR Joint Council Office (Grant number 14302FG094).

References

(1) Faraday, M. (1857) AuNP117-The Bakerian Lecture: Experimental Relations of Gold (and Other Metals) to Light. *Philos. Trans. R. Soc. London 147*, 145–181.

(2) Edwards, P. P., and Thomas, J. M. (2007) Gold in a Metallic Divided State—From Faraday to Present-Day Nanoscience. *Angew. Chemie Int. Ed. 46*, 5480–5486.

(3) Link, S., and El-Sayed, M. A. (2003) Optical Properties and Ultrafast Dynamics of Metallic Nanoparticles. *Annu. Rev. Phys. Chem. 54*, 331–366.

(4) Turkevich, J., Stevenson, P. C., and Hillier, J. (1951) A study of the nucleation and growth processes in the synthesis of colloidal gold. *Discuss. Faraday Soc.* 55.

(5) Brust, M., Walker, M., Bethell, D., Schiffrin, D. J., and Whyman, R. (1994) Synthesis of thiol-derivatised gold nanoparticles in a two-phase Liquid-Liquid system. *J. Chem. Soc. Chem. Commun.* 801.

(6) Häkkinen, H. (2012) The gold-sulfur interface at the nanoscale. *Nat. Chem. 4*, 443–55.

(7) Love, J. C., Estroff, L. A., Kriebel, J. K., Nuzzo, R. G., and Whitesides, G. M. (2005) Self-assembled monolayers of thiolates on metals as a form of nanotechnology. *Chem. Rev. 105*, 1103–69.

(8) Lévy, R., Thanh, N. T. K., Doty, R. C., Hussain, I., Nichols, R. J., Schiffrin, D. J., Brust, M., and Fernig, D. G. (2004) Rational and combinatorial design of peptide capping ligands for gold nanoparticles. *J. Am. Chem. Soc. 126*, 10076–84.

(9) Mirkin, C. a, Letsinger, R. L., Mucic, R. C., and Storhoff, J. J. (1996) A DNA-based method for rationally assembling nanoparticles into macroscopic materials.

Nature 382, 607–609.

(10) Alivisatos, A. P., Johnsson, K. P., Peng, X., Wilson, T. E., Loweth, C. J., Bruchez, M. P., and Schultz, P. G. (1996) Organization of "nanocrystal molecules" using DNA. *Nature 382*, 609–11.

(11) Otsuka, H., Nagasaki, Y., and Kataoka, K. (2003) PEGylated nanoparticles for biological and pharmaceutical applications. *Adv. Drug Deliv. Rev. 55*, 403–419.

(12) Duchesne, L., Gentili, D., Comes-Franchini, M., and Fernig, D. G. (2008) Robust Ligand Shells for Biological Applications of Gold Nanoparticles. *Langmuir 24*, 13572–13580.

(13) Chen, X., Qoutah, W. W., Free, P., Hobley, J., Fernig, D. G., and Paramelle, D. (2012) Features of Thiolated Ligands Promoting Resistance to Ligand Exchange in Self-Assembled Monolayers on Gold Nanoparticles. *Aust. J. Chem. 65*, 266.

(14) Free, P., Shaw, C. P., and Lévy, R. (2009) PEGylation modulates the interfacial kinetics of proteases on peptide-capped gold nanoparticles. *Chem. Commun.* 5009–11.

(15) Nieves, D. J., Azmi, N. S., Xu, R., Lévy, R., Yates, E. A., and Fernig, D. G. (2014) Monovalent maleimide functionalization of gold nanoparticles via copper-free click chemistry. *Chem. Commun. 50*, 13157–60.

(16) Sperling, R. A., Rivera Gil, P., Zhang, F., Zanella, M., and Parak, W. J. (2008) Biological applications of gold nanoparticles. *Chem. Soc. Rev. 37*, 1896–908.

(17) Daniel, M.-C., and Astruc, D. (2004) Gold Nanoparticles: Assembly, Supramolecular Chemistry, Quantum-Size-Related Properties, and Applications toward Biology, Catalysis, and Nanotechnology. *Chem. Rev. 104*, 293–346.

(18) Saha, K., Agasti, S., Kim, C., Li, X., and Rotello, V. (2012) Gold Nanoparticles in Chemical and Biological Sensing. *Chem. Rev. 112*, 2739–2779.

(19) Shaw, C. P., Fernig, D. G., and Lévy, R. (2011) Gold nanoparticles as advanced building blocks for nanoscale self-assembled systems. *J. Mater. Chem. 21*, 12181.

(20) Boles, M. A., Engel, M., and Talapin, D. V. (2016) Self-Assembly of Colloidal Nanocrystals: From Intricate Structures to Functional Materials. *Chem. Rev.*

(21) Sapsford, K. E., Tyner, K. M., Dair, B. J., Deschamps, J. R., and Medintz, I. L. (2011) Analyzing nanomaterial bioconjugates: A review of current and emerging purification and characterization techniques. *Anal. Chem. 83*, 4453–4488.

(22) Hostetler, M. J., Templeton, A. C., and Murray, R. W. (1999) Dynamics of place-exchange reactions on monolayer-protected gold cluster molecules. *Langmuir 15*, 3782–3789.

(23) Ghosh, S. K., and Pal, T. (2007) Interparticle coupling effect on the surface plasmon resonance of gold nanoparticles: from theory to applications. *Chem. Rev. 107*, 4797–862.

(24) Mie, G. (1908) Beiträge zur Optik Trüber Medien, Speziell Kolloidaler Metallösungen. *Ann. Phys. 330*, 377–445.

(25) Enustun, B. V., and Turkevich, J. (1963) Coagulation of Colloidal Gold. *J. Am. Chem. Soc. 85*, 3317–3328.

(26) Weisbecker, C. S., Merritt, M. V., and Whitesides, G. M. (1996) Molecular Self-Assembly of Aliphatic Thiols on Gold Colloids. *Langmuir 12*, 3763–3772.

(27) Schulz, F., Vossmeyer, T., Bastús, N. G., and Weller, H. (2013) Effect of the Spacer Structure on the Stability of Gold Nanoparticles Functionalized with Monodentate Thiolated Poly(ethylene glycol) Ligands. *Langmuir 29*, 9897–9908.

(28) Krpetić, Z., Davidson, A. M., Volk, M., Lévy, R., Brust, M., and Cooper, D. L. (2013) High-resolution sizing of monolayer-protected gold clusters by differential centrifugal sedimentation. *ACS Nano 7*, 8881–90.

(29) Bhattacharjee, S. (2016) DLS and zeta potential – What they are and what they are not? *J. Control. Release 235*, 337–351.

(30) Gomes, I., Santos, N. C., Oliveira, L. M. A., Quintas, A., Eaton, P., Pereira, E., and Franco, R. (2008) Probing Surface Properties of Cytochrome *c* at Au Bionanoconjugates. *J. Phys. Chem. C 112*, 16340–16347.

(31) Comenge, J., Sotelo, C., Romero, F., Gallego, O., Barnadas, A., Parada, T. G.-C., Domínguez, F., and Puntes, V. F. (2012) Detoxifying Antitumoral Drugs via Nanoconjugation: The Case of Gold Nanoparticles and Cisplatin. *PLoS One* (Rozhkova, E. A., Ed.) *7*, e47562.

(32) Hostetler, M. J., Wingate, J. E., Zhong, C.-J., Harris, J. E., Vachet, R. W., Clark, M. R., Londono, J. D., Green, S. J., Stokes, J. J., Wignall, G. D., Glish, G. L., Porter, M. D., Evans, N. D., and Murray, R. W. (1998) Alkanethiolate Gold Cluster Molecules with Core Diameters from 1.5 to 5.2 nm: Core and Monolayer Properties as a Function of Core Size. *Langmuir 14*, 17–30.

(33) Templeton, A. C., Hostetler, M. J., Kraft, C. T., and Murray, R. W. (1998) Reactivity of Monolayer-Protected Gold Cluster Molecules: Steric Effects. *J. Am. Chem. Soc. 120*, 1906–1911.

(34) Zhou, H., Li, X., Lemoff, A., Zhang, B., and Yan, B. (2010) Structural confirmation and quantification of individual ligands from the surface of multi-functionalized gold nanoparticles. *Analyst 135*, 1210.

(35) Fisher, E. A., Duffy, S. J., and Meli, M.-V. (2015) The determination of ligand shell composition of bifunctional alkanethiol-capped gold nanoparticles using GC/MS/MS. *RSC Adv. 5*, 33289–33293.

(36) Hinterwirth, H., Kappel, S., Waitz, T., Prohaska, T., Lindner, W., and Lämmerhofer, M. (2013) Quantifying Thiol Ligand Density of Self-Assembled Monolayers on Gold Nanoparticles by Inductively Coupled Plasma–Mass Spectrometry. *ACS Nano 7*, 1129–1136.

(37) Scheffer, A., Engelhard, C., Sperling, M., and Buscher, W. (2008) ICP-MS as a

new tool for the determination of gold nanoparticles in bioanalytical applications. *Anal. Bioanal. Chem. 390*, 249–252.

(38) Yan, B., Zhu, Z. J., Miranda, O. R., Chompoosor, A., Rotello, V. M., and Vachet, R. W. (2010) Laser desorption/ionization mass spectrometry analysis of monolayer-protected gold nanoparticles. *Anal. Bioanal. Chem. 396*, 1025–1035.

(39) Demers, L. M., Mirkin, C. A., Mucic, R. C., Reynolds, R. A., Letsinger, R. L., Elghanian, R., and Viswanadham, G. (2000) A Fluorescence-Based Method for Determining the Surface Coverage and Hybridization Efficiency of Thiol-Capped Oligonucleotides Bound to Gold Thin Films and Nanoparticles. *Anal. Chem. 72*, 5535–5541.

(40) Maus, L., Spatz, J. P., and Fiammengo, R. (2009) Quantification and Reactivity of Functional Groups in the Ligand Shell of PEGylated Gold Nanoparticles via a Fluorescence-Based Assay. *Langmuir 25*, 7910–7917.

(41) Zhu, Z. J., Rotello, V. M., and Vachet, R. W. (2009) Engineered nanoparticle surfaces for improved mass spectrometric analyses. *Analyst 134*, 2183–2188.

(42) Harkness, K. M., Cliffel, D. E., and McLean, J. A. (2010) Characterization of thiolate-protected gold nanoparticles by mass spectrometry. *Analyst 135*, 868–874.

(43) Pilolli, R., Palmisano, F., and Cioffi, N. (2012) Gold nanomaterials as a new tool for bioanalytical applications of laser desorption ionization mass spectrometry. *Anal. Bioanal. Chem. 402*, 601–623.

(44) Tanaka, K., Waki, H., and Ido, Y. (1988) Protein and Polymer Analyses up to m/z 100 000 by Laser Ionization Time-of-Flight Mass Spectrometry. *Rapid Commun. mass Spectrom. 2*, 151–153.

(45) Harkness, K. M., Hixson, B. C., Fenn, L. S., Turner, B. N., Rape, A. C., Simpson, C. A., Huffman, B. J., Okoli, T. C., McLean, J. A., and Cliffel, D. E. (2010) A Structural Mass Spectrometry Strategy for the Relative Quantitation of Ligands on Mixed Monolayer-Protected Gold Nanoparticles. *Anal. Chem. 82*, 9268–9274.

(46) Harford, C. G., Hamlin, A., and Parker, E. (1957) Electron microscopy of HeLa cells after the ingestion of colloidal gold. *J. Cell Biol. 3*, 749–756.

(47) Jürgens, L., Nichtl, A., and Werner, U. (1999) Electron density imaging of protein films on gold-particle surfaces with transmission electron microscopy. *Cytometry 37*, 87–92.

(48) Ardao, I., Comenge, J., Benaiges, M. D., Álvaro, G., and Puntes, V. F. (2012) Rational Nanoconjugation Improves Biocatalytic Performance of Enzymes: Aldol Addition Catalyzed by Immobilized Rhamnulose-1-Phosphate Aldolase. *Langmuir 28*, 6461–6467.

(49) Walkey, C. D., Olsen, J. B., Guo, H., Emili, A., and Chan, W. C. W. (2012) Nanoparticle Size and Surface Chemistry Determine Serum Protein Adsorption and Macrophage Uptake. *J. Am. Chem. Soc. 134*, 2139–2147.

(50) Belsey, N. A., Shard, A. G., and Minelli, C. (2015) Analysis of protein coatings

on gold nanoparticles by XPS and liquid-based particle sizing techniques. *Biointerphases 10*, 19012.

(51) Falabella, J. B., Cho, T. J., Ripple, D. C., Hackley, V. A., and Tarlov, M. J. (2010) Characterization of gold nanoparticles modified with single-stranded DNA using analytical ultracentrifugation and dynamic light scattering. *Langmuir 26*, 12740–7.

(52) Jadzinsky, P. D., Calero, G., Ackerson, C. J., Bushnell, D. A., and Kornberg, R. D. (2007) Structure of a thiol monolayer-protected gold nanoparticle at 1.1 A resolution. *Science 318*, 430–3.

(53) Azubel, M., Koivisto, J., Malola, S., Bushnell, D., Hura, G. L., Koh, A. L., Tsunoyama, H., Tsukuda, T., Pettersson, M., Hakkinen, H., and Kornberg, R. D. (2014) Electron microscopy of gold nanoparticles at atomic resolution. *Science (80-.). 345*, 909–912.

(54) Comenge, J., and Puntes, V. F. (2015) The Role of PEG Conformation in Mixed Layers: From Protein Corona Substrate to Steric Stabilization Avoiding Protein Adsorption. *Sci. Res.* 1–10.

(55) Tagliazucchi, M., Blaber, M. G., Schatz, G. C., Weiss, E. A., and Szleifer, I. (2012) Optical Properties of Responsive Hybrid Au@Polymer Nanoparticles. *ACS Nano 6*, 8397–8406.

(56) Xia, X., Yang, M., Wang, Y., Zheng, Y., Li, Q., Chen, J., and Xia, Y. (2012) Quantifying the Coverage Density of Poly(ethylene glycol) Chains on the Surface of Gold Nanostructures. *ACS Nano 6*, 512–522.

(57) Mandal, H. S., and Kraatz, H.-B. (2007) Effect of the surface curvature on the secondary structure of peptides adsorbed on nanoparticles. *J. Am. Chem. Soc. 129*, 6356–7.

(58) Templeton, A. C., Wuelfing, W. P., and Murray, R. W. (2000) Monolayer-Protected Cluster Molecules Characterization of MPCs. *Accounts Chem. 33*, 27–36.

(59) Fabris, L., Antonello, S., Armelao, L., Donkers, R. L., Polo, F., Toniolo, C., and Maran, F. (2006) Gold nanoclusters protected by conformationally constrained peptides. *J. Am. Chem. Soc. 128*, 326–36.

(60) Shaw, C. P., Middleton, D. A., Volk, M., and Lévy, R. (2012) Amyloid-derived peptide forms self-assembled monolayers on gold nanoparticle with a curvature-dependent β-sheet structure. *ACS Nano 6*, 1416–26.

(61) Rio-Echevarria, I. M., Tavano, R., Causin, V., Papini, E., Mancin, F., and Moretto, A. (2011) Water-soluble peptide-coated nanoparticles: control of the helix structure and enhanced differential binding to immune cells. *J. Am. Chem. Soc. 133*, 8–11.

(62) Folkers, J. P., Laibinis, P. E., and Whitesides, G. M. (1992) Self-assembled monolayers of alkanethiols on gold: comparisons of monolayers containing mixtures of short- and long-chain constituents with methyl and hydroxymethyl terminal groups. *Langmuir 8*, 1330–1341.

(63) Stranick, S. J., Parikh, A. N., Tao, Y.-T., Allara, D. L., and Weiss, P. S. (1994) Phase Separation of Mixed-Composition Self-Assembled Monolayers into Nanometer Scale Molecular Domains. *J. Phys. Chem. 98*, 7636–7646.

(64) Tamada, K., Hara, M., Sasabe, H., and Knoll, W. (1997) Surface Phase Behavior of n-Alkanethiol Self-Assembled Monolayers Adsorbed on Au(111): An Atomic Force Microscope Study. *Langmuir 13*, 1558–1566.

(65) Duchesne, L., Wells, G., Fernig, D. G., Harris, S. A., and Lévy, R. (2008) Supramolecular domains in mixed peptide self-assembled monolayers on gold nanoparticles. *Chembiochem 9*, 2127–34.

(66) Gentilini, C., Franchi, P., Mileo, E., Polizzi, S., Lucarini, M., and Pasquato, L. (2009) Formation of Patches on 3D SAMs Driven by Thiols with Immiscible Chains Observed by ESR Spectroscopy. *Angew. Chemie Int. Ed. 48*, 3060–3064.

(67) Harkness, K. M., Balinski, A., McLean, J. A., and Cliffel, D. E. (2011) Nanoscale Phase Segregation of Mixed Thiolates on Gold Nanoparticles. *Angew. Chemie-International Ed. 50*, 10554–10559.

(68) Jackson, A. M., Myerson, J. W., and Stellacci, F. (2004) Spontaneous assembly of subnanometre-ordered domains in the ligand shell of monolayer-protected nanoparticles. *Nat. Mater. 3*, 330–336.

(69) Cesbron, Y., Shaw, C. P., Birchall, J. P., Free, P., and Lévy, R. (2012) Stripy Nanoparticles Revisited. *Small 8*, 3714–3719.

(70) Stirling, J., Lekkas, I., Sweetman, A., Djuranovic, P., Guo, Q., Pauw, B., Granwehr, J., Lévy, R., and Moriarty, P. (2014) Critical Assessment of the Evidence for Striped Nanoparticles. *PLoS One* (Shankar, S. S., Ed.) *9*, e108482.

(71) Yu, M., and Stellacci, F. (2012) Response to "Stripy Nanoparticles Revisited." *Small 8*, 3720–3726.

(72) Ong, Q. K., and Stellacci, F. (2015) Response to "Critical Assessment of the Evidence for Striped Nanoparticles." *PLoS One* (Sangaru, S. S., Ed.) *10*, e0135594.

(73) Zaupa, G., Mora, C., Bonomi, R., Prins, L. J., and Scrimin, P. (2011) Catalytic self-assembled monolayers on Au nanoparticles: The source of catalysis of a transphosphorylation reaction. *Chem. - A Eur. J. 17*, 4879–4889.

(74) Bonomi, R., Cazzolaro, A., and Prins, L. J. (2011) Assessment of the morphology of mixed SAMs on Au nanoparticles using a fluorescent probe. *Chem. Commun. 47*, 445–447.

(75) De Gennes, P. G. (1992) Soft matter. *Rev. Mod. Phys. 64*, 645–648.

(76) Perro, A., Reculusa, S., Ravaine, S., Bourgeat-Lami, E., and Duguet, E. (2005) Design and synthesis of Janus micro- and nanoparticles. *J. Mater. Chem. 15*, 3745.

(77) Walther, A., and Müller, A. H. E. (2013) Janus Particles: Synthesis, Self-Assembly, Physical Properties, and Applications. *Chem. Rev. 113*, 5194–5261.

(78) Nørgaard, K., Weygand, M. J., Kjaer, K., Brust, M., and Bjørnholm, T. (2004) Adaptive chemistry of bifunctional gold nanoparticles at the air/water interface. A synchrotron X-ray study of giant amphiphiles. *Faraday Discuss. 125*, 221–233.

(79) Andala, D. M., Shin, S. H. R., Lee, H.-Y., and Bishop, K. J. M. (2012) Templated Synthesis of Amphiphilic Nanoparticles at the Liquid–Liquid Interface. *ACS Nano 6*, 1044–1050.

(80) Charchar, P., Christofferson, A. J., Todorova, N., and Yarovsky, I. (2016) Understanding and Designing the Gold-Bio Interface: Insights from Simulations. *Small 12*, 2395–2418.

(81) Hautman, J., and Klein, M. L. (1989) Simulation of a monolayer of alkyl thiol chains. *J. Chem. Phys. 91*, 4994.

(82) Tupper, K. J., and Brenner, D. W. (1994) Molecular dynamics simulations of friction in self-assembled monolayers. *Thin Solid Films 253*, 185–189.

(83) Mahaffy, R., Bhatia, R., and Garrison, B. J. (1997) Diffusion of a Butanethiolate Molecule on a Au{111} Surface. *J. Phys. Chem. B 101*, 771–773.

(84) Gerdy, J. J., and Goodard, W. A. (1996) Atomistic Structure for Self-Assembled Monolayers of Alkanethiols on Au(111) Surfaces. *J. Am. Chem. Soc. 118*, 3233–3236.

(85) Ghorai, P. K., and Glotzer, S. C. (2007) Molecular Dynamics Simulation Study of Self-Assembled Monolayers of Alkanethiol Surfactants on Spherical Gold Nanoparticles. *J. Phys. Chem. C 111*, 15857–15862.

(86) Singh, C., Ghorai, P. K., Horsch, M. A., Jackson, A. M., Larson, R. G., Stellacci, F., and Glotzer, S. C. (2007) Entropy-Mediated Patterning of Surfactant-Coated Nanoparticles and Surfaces. *Phys. Rev. Lett. 99*, 226106.

(87) Velachi, V., Bhandary, D., Singh, J. K., and Cordeiro, M. N. D. S. (2015) Structure of Mixed Self-Assembled Monolayers on Gold Nanoparticles at Three Different Arrangements. *J. Phys. Chem. C 119*, 3199–3209.

(88) Van Lehn, R. C., and Alexander-Katz, A. (2013) Structure of Mixed-Monolayer-Protected Nanoparticles in Aqueous Salt Solution from Atomistic Molecular Dynamics Simulations. *J. Phys. Chem. C 117*, 20104–20115.

(89) Fetisov, E. O., and Siepmann, J. I. (2016) Structure and Phase Behavior of Mixed Self-Assembled Alkanethiolate Monolayers on Gold Nanoparticles: A Monte Carlo Study. *J. Phys. Chem. B 120*, 1972–1978.

(90) Iori, F., Di Felice, R., Molinari, E., and Corni, S. (2009) GolP: an atomistic force-field to describe the interaction of proteins with Au(111) surfaces in water. *J. Comput. Chem. 30*, 1465–76.

(91) Wright, L. B., Rodger, P. M., Corni, S., and Walsh, T. R. (2013) GolP-CHARMM: First-Principles Based Force Fields for the Interaction of Proteins with Au(111) and Au(100). *J. Chem. Theory Comput. 9*, 1616–1630.

(92) Andresen, H., Mager, M., Grießner, M., Charchar, P., Todorova, N., Bell, N., Theocharidis, G., Bertazzo, S., Yarovsky, I., and Stevens, M. M. (2014) Single-Step Homogeneous Immunoassays Utilizing Epitope-Tagged Gold Nanoparticles: On the Mechanism, Feasibility, and Limitations. *Chem. Mater. 26*, 4696–4704.

(93) Todorova, N., Chiappini, C., Mager, M., Simona, B., Patel, I. I., Stevens, M. M., and Yarovsky, I. (2014) Surface presentation of functional peptides in solution determines cell internalization efficiency of TAT conjugated nanoparticles. *Nano Lett. 14*, 5229–37.

(94) Lee, K. H., and Ytreberg, F. M. (2012) Effect of Gold Nanoparticle Conjugation on Peptide Dynamics and Structure. *Entropy 14*, 630–641.

(95) Aubin-Tam, M.-E., and Hamad-Schifferli, K. (2008) Structure and function of nanoparticle–protein conjugates. *Biomed. Mater. 3*, 34001.

(96) Aubin-Tam, M.-E., Hwang, W., and Hamad-Schifferli, K. (2009) Site-directed nanoparticle labeling of cytochrome c. *Proc. Natl. Acad. Sci. U. S. A. 106*, 4095–100.

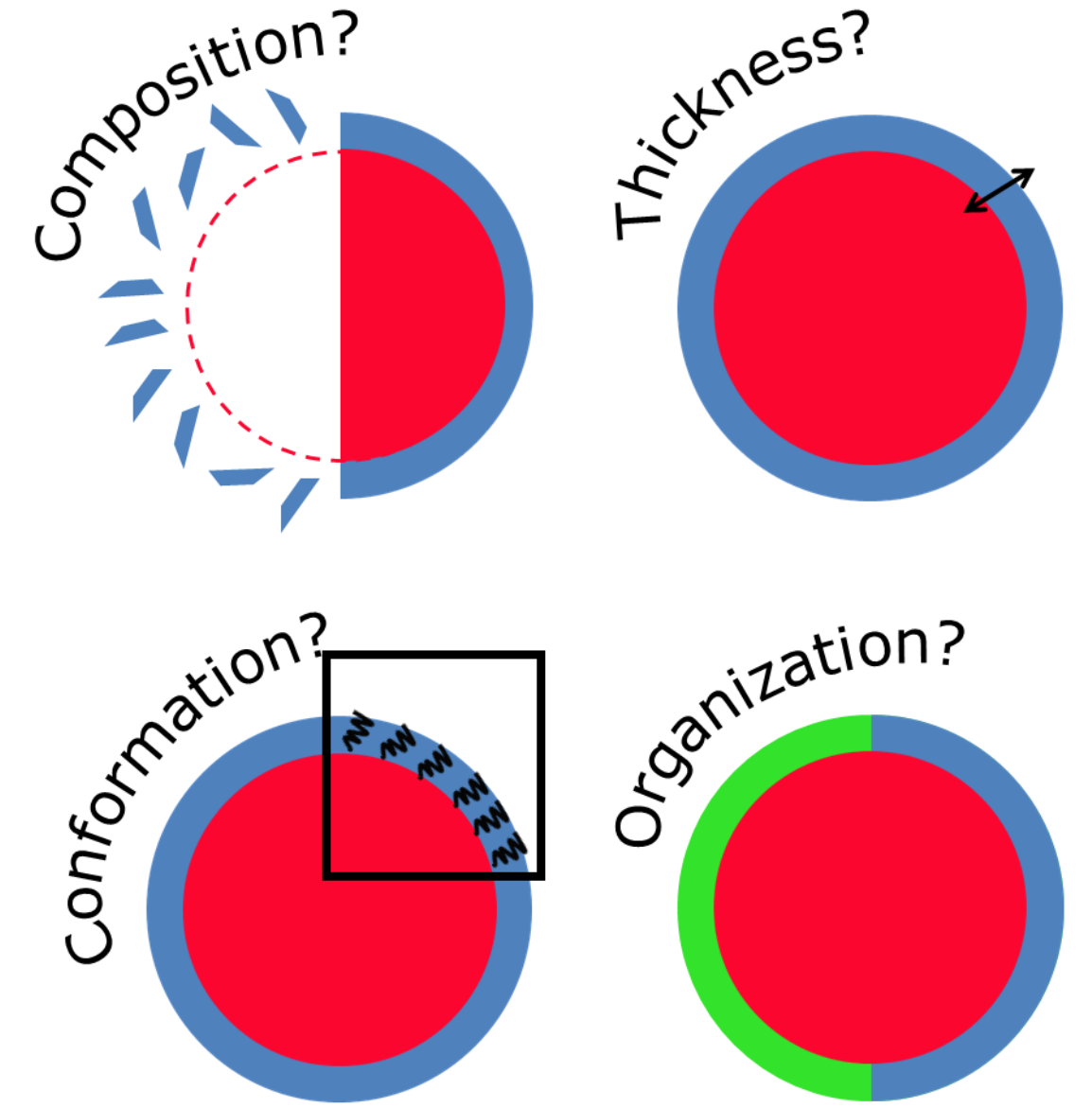

Insert Table of Contents artwork here

CHAPTER 2

ATTEMPT TO CHARACTERIZE THE ORGANIZATION OF A MIXED SELF-ASSEMBLED MONOLAYER ON GOLD NANOPARTICLES WITH BPA-CONTAINING PEPTIDES

2.1 Introduction

As previously discussed in Chapter 1, the structural characterization of self-assembled monolayers at the gold nanoparticles (GNPs) surface is critical to envision the design of bio-nanomaterials with well-defined biophysical and structural properties.

For this work, gold nanoparticles were functionalized with a mixed self-assembled monolayer consisting of benzophenone-containing pentapeptide, specifically designed for this study, and polyethylene glycol alkanethiol molecule. Upon irradiation at ~350 nm, the carbonyl group of the benzophenone moiety is expected to cross-link to an adjacent C-H bond.[1] Hence, analysis of the capping SAM on the GNPs surface before and after irradiation aims to validate the photo-cross-linking reaction, evaluate the extent of cross-linking within the ligand shell and identify the photo-cross-linked ligands. Also, by using dimethyl sulfoxide (DMSO) as solvent, the benzophenone moiety is expected to cross-link to its methyl groups, thus probing the solvent accessibility within the monolayer.

Thus, the experiments were conceived to provide an insight into the molecular organization and compactness of mixed monolayers self-assembled on gold nanoparticles.

This chapter reports first, proofs of successful photo-cross-linking between benzophenone-containing peptide and DMSO; second, it details the methodology developed to functionalize the GNPs and the techniques adopted to characterize them; third, it describes the investigation of the occurrence of the photo-cross-linking on the GNPs surface, that however was not detected in the conditions in which was expected to take place.

2.1.1 Benzophenone

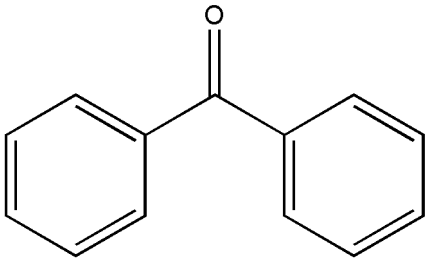

Fig. 2.1 - Benzophenone molecule (BP)

Benzophenone (BP, **Fig. 2.1**) has been reported as photo-cross-linker in biological systems for the first time in 1974.[2] In the 1980s, BP has been progressively used to map the conformation of several biological objects, e.g. membranes and nucleotide binding sites. In the following decades, the use of photo-activable aryl ketone derivatives massively increased because of the successful synthesis of the BP-containing amino acid p-benzoyl-L-phenylalanine (L-Bpa).[3,4] Bpa can be easily inserted into polypeptide chains and allows the mapping of protein-peptide interactions by photo-controlling the excitation of BP photo-phore and therefore the protein-binding site modifications. Dorman and Prestwich[1] asserted in their 1994 review that BP photo-probes have quickly replaced aryl azide and diazirine photo-phores, which were employed for the same purposes, for four main reasons. Firstly, aryl ketone derivatives are chemically more stable than azo-compounds, i.e. diazo esters, aryl azides and diazirines. Secondly, the triplet state of BPs is generated by light at 350-360 nm, which does not cause damage to proteins. Thirdly, BPs are quite selective reactants; they react with C-H bonds, even in the presence of bulk nucleophiles, such as water molecules. Fourthly, the protein-binding site modifications are quite efficient and specific.

Before discussing the mechanism of the benzophenone photo-chemical cross-linking reaction, it is necessary to consider the electronic configuration of a carbonyl group. The formaldehyde molecule can be an example of compound bearing the carbonyl group; it consists of two C-H sigma bonds, a C-O sigma bond, a C=O π-bond and two non-bonding oxygen electron pairs. The representation of the oxygen atom as a sp-oxygen arises from molecular orbital calculations (**Fig. 2.2**).[5] The two allowed electronic transitions are depicted in the formaldehyde energy level diagram below (**Fig. 2.3**). The molecule has 12 electrons in total; the first level, corresponding to the C-O sigma bond, is not shown in the diagram below. The next two sigma bonding orbitals are associated with the two C-H bonds; the lower nonbonding orbital refers to the electron pair

in the sp-oxygen orbital (colored in orange in **Fig. 2.2**), while the second nonbonding electron pair is found in the energetically higher oxygen p-orbital (colored in green in **Fig. 2.2**).

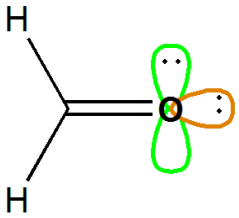

Fig. 2.2 – Lewis structure of formaldehyde depicting a sp-hybridized oxygen atom, adapted from ref. 5

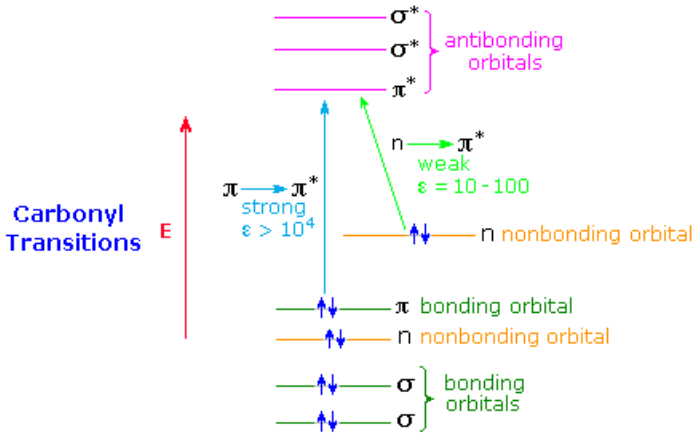

Fig. 2.3 – Diagram of the carbonyl group's electronic transitions, adapted from ref. 5

In the UV-Vis spectrum of a molecule bearing the carbonyl group, two broad bands, associated with the two electronic excitations shown in Fig. 2.2, will be observed. The wavelengths of the carbonyl transitions depend on the extent of conjugation with carbon double bonds; with an increase of conjugation the carbonyl functional group shows a red-shift in its absorbance bands (**Table 2.1**).[6] The reason of this phenomenon can be graphically explained by molecular orbital diagrams. Basically, with an extension of conjugation, the energy levels of molecular orbitals get closer and therefore the energy needed for electron transitions is smaller.

Table 2.1 - Carbonyl functional group maximum absorbance for different extension of conjugation with carbon double bonds

Functional Group	λ_{max} (nm) $\pi \rightarrow \pi^*$	λ_{max} (nm) $n \rightarrow \pi^*$
C=O	166	280
C=C-C=O	240	320
C=C-C=C-C=O	270	350

Moreover, the two bands have different intensity due to the major or minor spatial overlap between orbitals. In the case of benzophenone, the $n \rightarrow \pi^*$ transition is in the region of 320-370 nm[7] and it is very weak ($111 < \varepsilon < 151$ M^{-1} cm^{-1})[8] because of the insignificant overlap between the oxygen p-orbital and the π^* antibonding orbital; the electron wavefunction is promoted from the plane of the molecule to a plane that is perpendicular to it. On the other hand, the π bonding orbital and the π^* antibonding orbital overlap almost entirely, thus the probability of a $\pi \rightarrow \pi^*$ transition is quite high and the UV-Vis absorption band in the region of 240-300 nm[7] has a high intensity ($16600 < \varepsilon < 21800$ M^{-1} cm^{-1}).[8] Both bands are deeply influenced by the solvent chosen.[7–9] The $n \rightarrow \pi^*$ transition shows a blue-shift of approximately 2200 cm^{-1} from n-hexane to water because H-bond donor solvents and also solvents with great dipole moments stabilize the ground state of benzophenone more than the excited one. As for the $\pi \rightarrow \pi^*$ transitions, they show a redshift of up to 1600 cm^{-1} when using more polar solvents, because the excited state is more stabilized than the ground state by hydrogen bonds and dipole-dipole forces.

For what concerns the photo-chemical cross-linking reaction mechanism of aryl ketone derivatives, it is the $n \rightarrow \pi^*$ transition that induces the triplet state necessary for the photo-cross-linking reaction to take place.[10] A simplified scheme (**Scheme 2.1**) of benzophenone photo-chemistry is shown below.

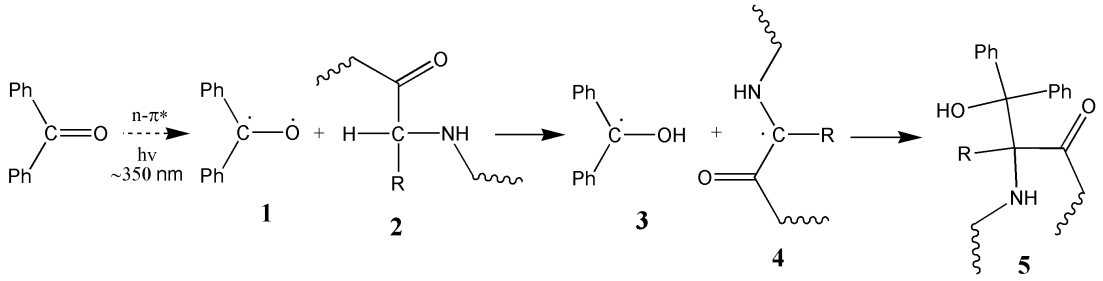

Scheme 2.1 – Photo-chemistry of benzophenone molecule, adapted from Dorman et al.[1]

One electron is excited from the p-nonbonding oxygen orbital to the π*-antibonding carbonyl group orbital by absorption of a photon at ~ 350 nm. Once the diradicaloid triplet state is formed (**1**), the oxygen becomes electrophilic because of the resulting electron deficiency and therefore interacts with adjacent C-H bonds (**2**). A hydrogen atom is then abstracted from the C-H bond by the oxygen atom that becomes a hydroxy group. The ketyl (**3**) and alkyl (**4**) radicals then recombine, forming a new C-C covalent bond in benzopinacol-type compounds (**5**). The triplet state is necessary for efficient cross-linking to a target macromolecule, but the life time of this excited state depends on the availability of geometrically accessible C-H bonds; it relaxes to the ground state after 80-120 μs in the absence of a proton suitable for abstraction.[1] Thus, BP photo-probes may go through several excitation-relaxation cycles before successfully covalently binding the substrate. However, the lifetime can be 100 times shorter in the presence of a weak C-H bond.[1] The efficiency of a photo-cross-linking reaction carried out by BP derivatives relies therefore on two main factors. Firstly, the photo-probe and the substrate should spend enough time at an interactive distance. Theoretical calculations and experimental data[10] suggest that the BP oxygen reacts with substrates within a reactive distance of 3.1 Å. Secondly, the molecules' geometry has to be suitable for chemical, steric and electronic interactions and, therefore, H-abstraction. Moreover, the strength of the C-H sigma bond being broken and the stability of the out-coming radical are determinants for the H-abstraction success.

2.1.2 Bpa-containing Peptides

In the 1980s, due to the increased use of benzophenone derivatives for photo-affinity labeling purposes, Kauer et al.[3] designed a modification of the essential amino acid phenylalanine and conceived the artificial amino acid benzoyl-L-phenylalanine (Bpa), shown in **Fig. 2.4**. The idea underlying their work was to synthesize a BP-containing amino acid that could be easily incorporated in polypeptide chains. Thus, Bpa-containing peptides have been successfully used to map active site domains to probe protein-peptide interactions.[1]

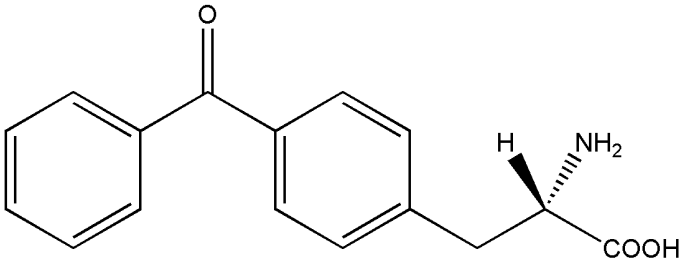

Fig. 2.4 - Benzoyl-L-phenylalanine (Bpa) amino acid

In this project, in order to characterize the molecular organization of and assess the solvent accessibility into mixed self-assembled monolayers on GNPs, Bpa-containing pentapeptides (**Fig. 2.5-2.7**) were designed to functionalize the gold nanoparticles. The Bpa amino acid was inserted at different positions along the chain of three pentapeptides. All polypeptides have an N-terminal cysteine residue, because the thiol group is necessary to anchor the peptide to the gold surface, and a modified C-terminal threonine residue to have a polar head without charged residues, which would be likely to cause non-specific interactions and reduced monolayer compactness.[11] Two valine residues are present along the chain in order to drive the packing and stabilize the peptide monolayer by hydrophobic interactions. Moreover, the BP photo-phore is linked to the peptide backbone through a CH_2 unit, conferring a moderate flexibility to the BP molecule; in principle, the position of the Bpa amino acid along the peptide chain should provide information on the compactness of the monolayer through the regioselectivity of H-abstraction.

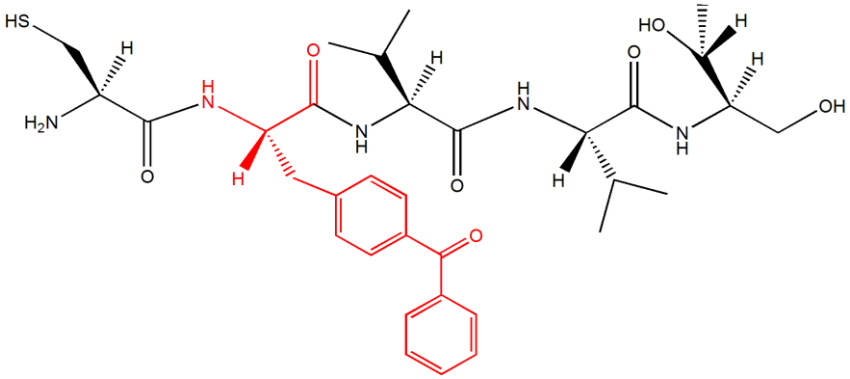

Fig. 2.5 – H-C(Bpa)VVT-ol pentapeptide structure; Bpa amino acid is highlighted in red.

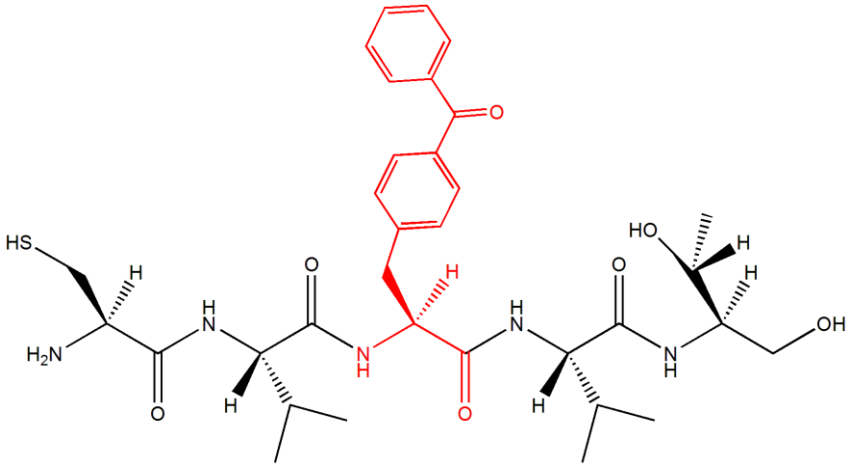

Fig. 2.6 – H-CV(Bpa)VT-ol pentapeptide structure; Bpa amino acid is highlighted in red.

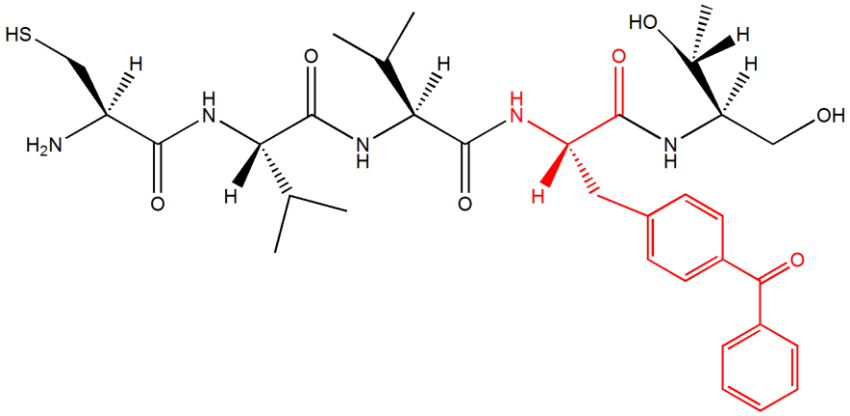

Fig. 2.7 - H-CVV(Bpa)T-ol pentapeptide structure; Bpa amino acid is highlighted in red.

The Bpa amino acid was chosen not only because it allows a highly modular synthesis, but also because the products of the photo-chemical reaction triggered by the benzophenone moiety are chemically stable and therefore, it is possible to determine qualitatively and quantitatively the efficiency of the photo-chemical reaction.

2.2 Experimental Outline

The experimental work was developed as follows. First, a Bpa-containing peptide was dissolved in dimethyl sulfoxide (DMSO) and characterized by Fourier Transform Infrared (FTIR), Ultraviolet-Visible (UV-Vis) spectroscopies and Electron Spray Ionization Mass Spectrometry (ESI-MS). DMSO is a suitable solvent since it is polar aprotic, dissolves well both polar and non-polar substances and its main absorbance bands do not overlap with those of benzophenone. Second, the peptide in DMSO was irradiated at ~350 nm to

selectively excite the BP into the diradicaloid triplet state, in which the oxygen abstracts a proton from the methyl groups of DMSO and therefore cross-links to it. The UV-induced photo-chemical modifications occurring at different irradiation times were monitored by UV-Vis, FTIR and ESI-MS techniques. The irradiation conditions for the peptide to achieve full cross-linking were established both at the University of Liverpool and at the Institute of Materials Research and Engineering (IMRE) in Singapore, using different UV-light sources and set-ups (see **Instruments** section for details).

GNPs were then functionalized with a mixed self-assembled monolayer consisting of Bpa-containing pentapeptide and polyethylene glycol alkanethiol molecule; the presence of both ligands on the gold surface was proven by FTIR spectroscopy and Laser Desorption Ionization Mass Spectrometry (LDI-MS). The functionalized GNPs were suspended in DMSO, in order to characterize not only the molecular organization, but also to assess the solvent accessibility into mixed self-assembled monolayers, and irradiated for the time periods in which the photo-cross-linking reaction was expected to take place.

The occurrence of the photo-cross-linking reaction on the gold surface was investigated by FTIR in solution.

2.3 Photo-Irradiation of Bpa-Containing Peptide in DMSO

2.3.1 UV-Vis Spectra

The UV-Vis spectrum at the **top** of **Fig. 2.8** shows that H-CV(Bpa)VT-ol peptide in DMSO is characterized by two absorbance bands: a strong one between 265 and 300 nm and a weaker one between 315 and 370 nm, corresponding to the π-π* and n-π* transitions of benzophenone, respectively.[7,8] In Dilling's work,[8] the UV-Vis spectra of benzophenone were determined in different solvents; in DMSO, due to its absorption, only the wavelength associated to the maximum absorbance of the n-π* transition was reported, i.e. 340.5 nm. An extinction coefficient of ~180 M^{-1} cm^{-1} at 340 nm was calculated from the spectrum shown in **Fig. 2.8, top**, in reasonable agreement with the range reported in Dilling's work for the n-π* transition in the solvents investigated, i.e. ε = 111-151 M^{-1} cm^{-1}.[8]

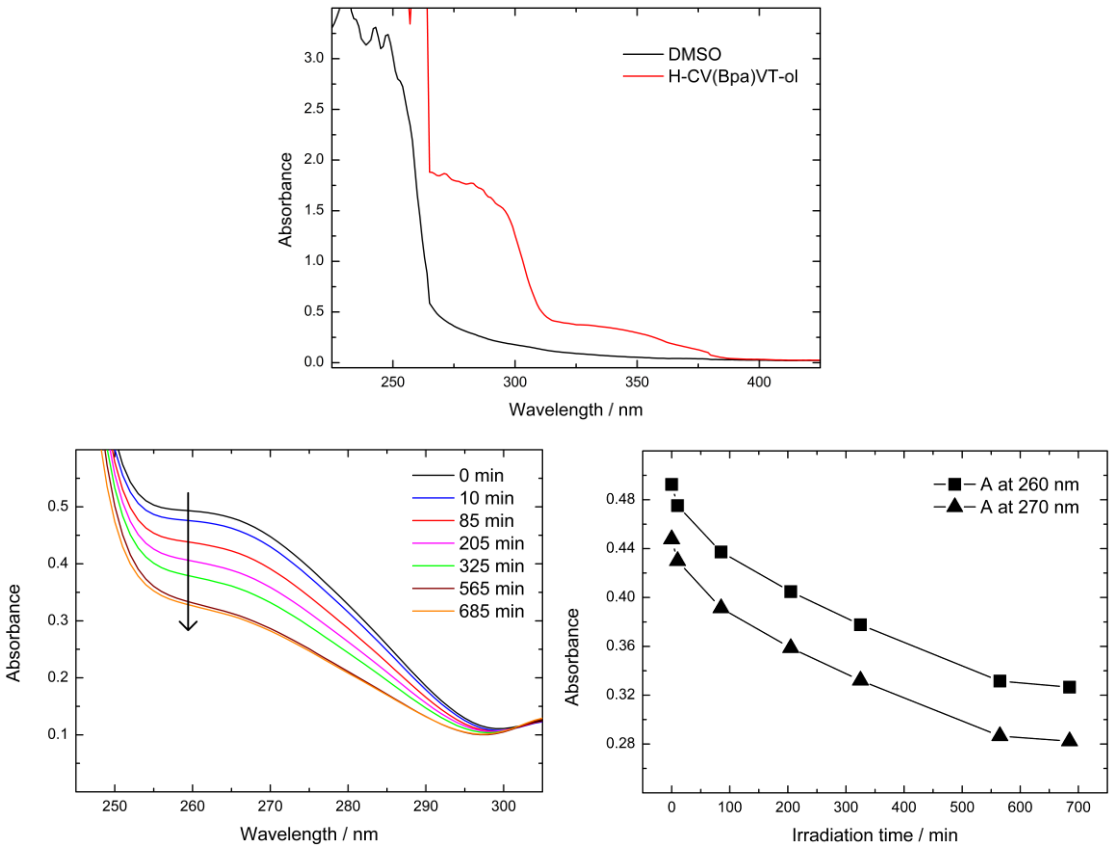

Fig. 2.8 - UV-Vis spectra of **top left:** 1.9 mM H-CV(Bpa)VT-ol peptide in DMSO and DMSO solvent (path length of 1 cm); **bottom left:** 1.9 mM H-CV(Bpa)VT-ol peptide after different irradiation times (path length of 0.02 cm). **Bottom right:** changes in absorbance at 260 and 270 nm after different irradiation times. Irradiation was performed at UoL using a Xenon lamp with an intensity of ~60 mW/cm^2 between 340 and 380 nm.

Upon UV irradiation the π-π* transition band in the UV-Vis spectra (**Fig. 2.8, bottom left**) decreases; it has not been possible to monitor the changes in the n-π* transition band because the absorbance is too weak to be observed with the path length used, i.e. 0.02 cm. Such decrease in absorbance of the π-π* transition band is in agreement with the decrease in conjugation that occurs when the benzophenone molecule cross-links to an adjacent carbon atom (**Scheme 2.1**), in this case the DMSO methyl group.

The panel at the **bottom right** of **Fig. 2.8** suggests that the photo-chemical reaction is almost completed after ~600 min of irradiation. Hence, a very low quantum yield for the photo-cross-linking reaction is estimated, i.e. lower than 0.3%, in agreement with Woodward at al.'s findings.[12]

2.3.2 FTIR Spectra

Several polymer studies[13–15] used the benzophenone molecule as photo-initiator for the polymerization and monitored the reaction at different

polymerization steps by FTIR spectroscopy. They used the benzophenone molecule because it is easily detectable by infrared spectroscopy. The carbonyl stretching band is indeed very strong and sensitive to any interaction with neighboring groups. In the crystalline phase[16] the molecule is planar, the conjugated system extended and the carbonyl stretching vibration is at 1650 cm^{-1}. In solution, where the molecule is free to rotate and therefore loses co-planarity, the C=O character is reinforced and it is possible to observe a shift to higher wavenumbers, i.e. 1667 cm^{-1}. When the molecule is involved in interactions, such as hydrogen bonds, the carbonyl stretching mode is shifted back to values closer to 1650 cm^{-1}.

Moreover, if the carbonyl group photo-cross-links and turns into a tertiary alcohol group, a different functional group will be detected by FTIR spectroscopy.

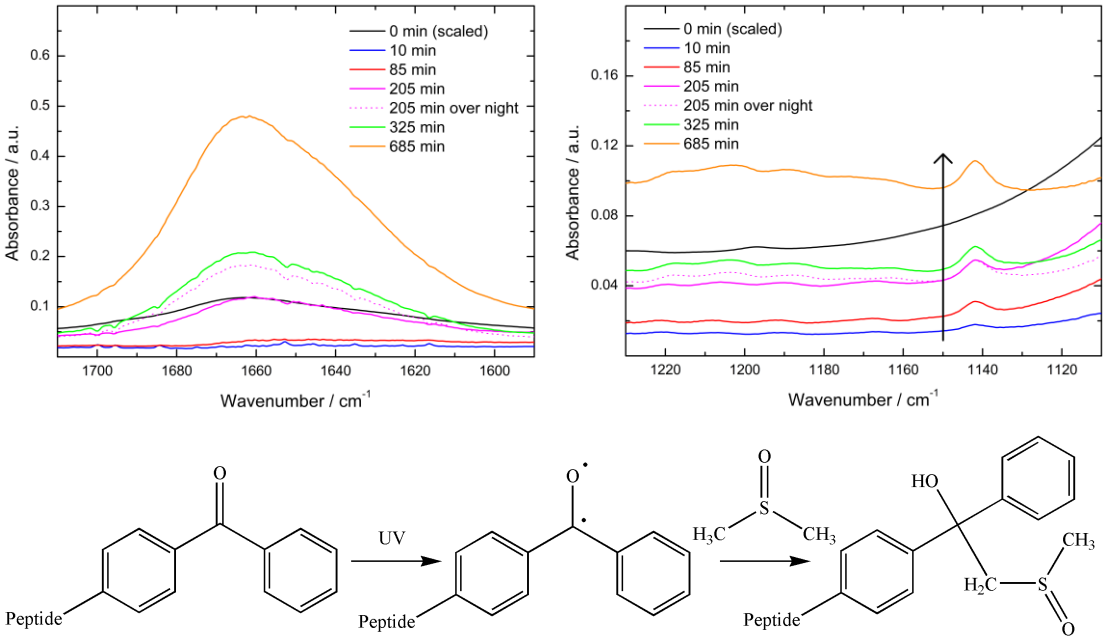

Fig. 2.9 – Difference FTIR spectra, i.e. spectrum of the sample before irradiation (0 min) subtracted from the spectra at different irradiation times, of 1.9 mM H-CV(Bpa)VT-ol peptide in DMSO in the carbonyl (**top left**) and tertiary alcohol group (**top right**) regions. The "over night" comment refers to the spectrum of the sample irradiated for 205 min taken after night. **Bottom:** scheme of the benzophenone photo-cross-linking reaction with DMSO.

According to the mechanism proposed by Dorman et al.,[1] a decrease in the band at 1650 cm^{-1}, associated with the carbonyl group, and an increase in a band associated with the hydroxyl group, were expected.

An increase in the band at 1650 cm^{-1} has been observed (**Fig. 2.9, top left**) though. However, this increase was found to be time dependent and not irradiation time dependent, as the magenta curves, corresponding to spectra of

the same sample taken before (solid line) and after night (dashed line), show. It is worth noting that the bending vibration of water is at this frequency and that DMSO solvent is highly hygroscopic hence, it absorbs water vapor from the surrounding environment. Indeed, this peak was found to increase even when taking spectra of neat DMSO. Thus, even though the spectra were taken in a FTIR spectrophotometer purged with dry air, the amount of water in the solution was probably increasing over time by leakage from the CaF_2 windows, an effect which has been previously observed in the group, but despite efforts (e.g. windows left in the oven for two weeks) and control experiments, it was not possible to prevent the water contamination. Therefore, the uptake of water completely hides the C=O band, preventing to draw any conclusions from the results in this region.

Nevertheless, the band at ~1140 cm^{-1} (**Fig. 2.9, top right**), corresponding to the C-O stretch of a tertiary alcohol group,[17] gives indication that the cross-linking reaction between the H-CV(Bpa)VT-ol peptide and DMSO occurred as shown in the scheme in **Fig. 2.9**.

It is worth remarking how well the time dependent increase in absorbance of the band at ~1140 cm^{-1} correlates with the decrease of the absorbance in the UV-Vis spectra reported in **Fig. 2.8, bottom left**: the gradual decrease in conjugation is reflected in the gradual increase of the tertiary alcohol group formation.

2.3.3 MS Spectra

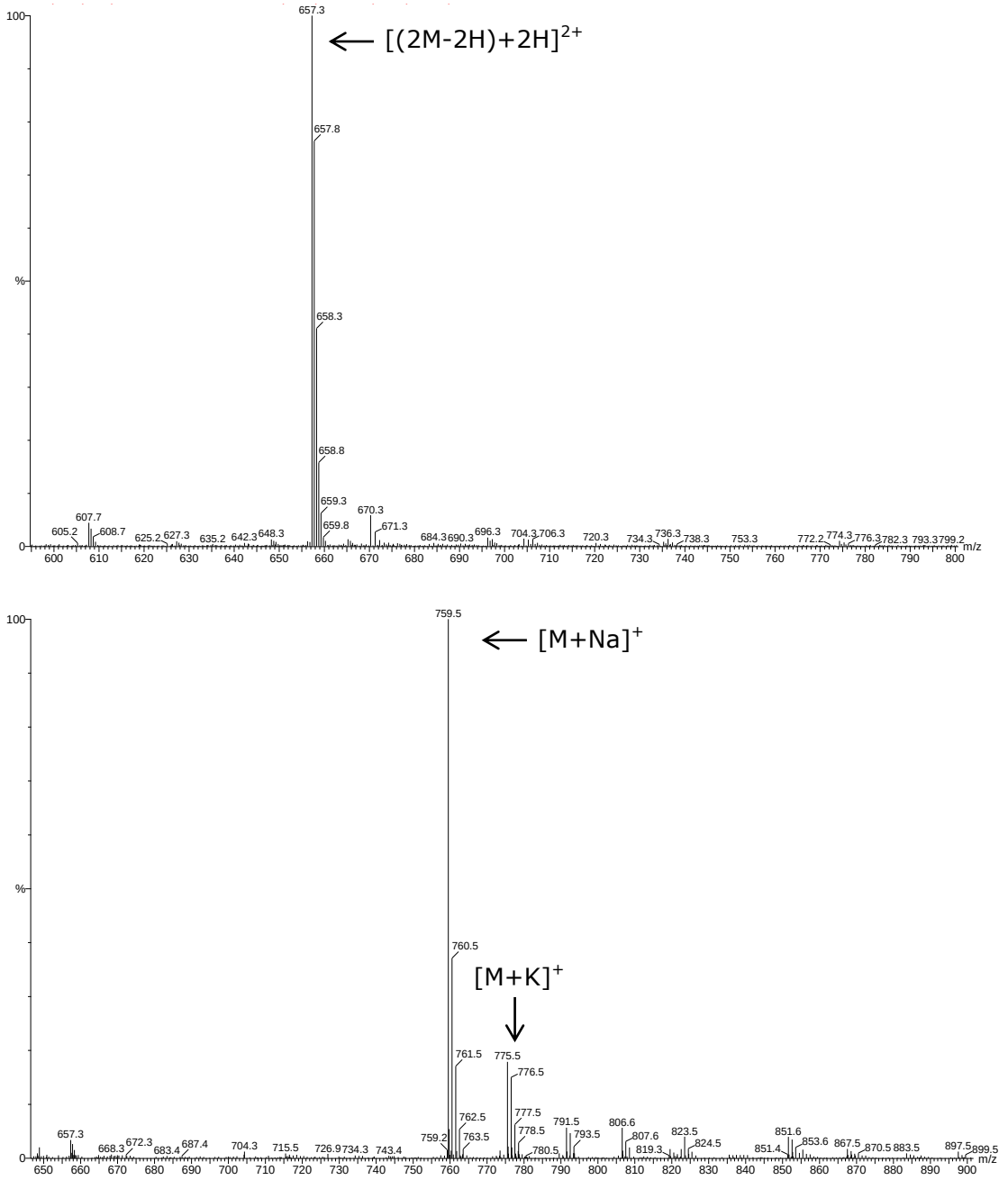

Fig. 2.10 – Time-of-flight mass spectrometry electrospray ionization in positive mode (TOF MS ES^+) of H-CV(Bpa)VT-ol peptide in DMSO; **top:** before irradiation; **bottom:** after 685 min of irradiation. M refers to the neutral peptide hence, $[M+H]^+$ refers to the protonated species. (2M-2H) refers to two peptides covalently bound together through a disulfide bond, hence $[(2M-2H)+H]^+$ refers to the protonated dipeptide.

The exact mass of the H-CV(Bpa)VT-ol peptide is 657.32 Da, whereas the exact mass of the peptide covalently bound to DMSO, as shown in **Fig. 2.9**, is 735.33 Da. In the spectrum before irradiation (**Fig. 2.10, top**), the ion at m/z 657.3 corresponds to a doubly charged dimer, i.e. two peptides bound together

through a disulfide bond with two protons; the isotope peaks have indeed a separation of only 0.5.

In the spectrum after irradiation (**Fig. 2.10, bottom**), there are peaks at 759.5 and 775.5 m/z which correspond to the H-CV(Bpa)VT-ol peptide covalently bound to the DMSO plus a sodium or potassium ion, respectively. The peak at 657.3 is also found in the spectrum after irradiation, but it is much weaker than those at 759.5 and 775.5 m/z.

Thus, ES-MS further confirms that the cross-linking reaction between H-CV(Bpa)VT-ol peptide and DMSO has occurred.

2.3.4 Conclusions

UV-Vis spectra, but especially FTIR and MS spectra demonstrate that the photo-cross-linking between H-CV(Bpa)VT-ol peptide and DMSO occurred and the results, over the different irradiation times, correlate well in all of the techniques. They are also in agreement with the benzophenone photo-chemical reaction mechanism suggested by Dorman et al.[1]

It is worth noting that the irradiation conditions for the free peptides were established both at the University of Liverpool and at the Institute of Materials Research and Engineering (IMRE) in Singapore using different UV-light sources and set-ups. The results presented in Section **2.3** were obtained at the University of Liverpool using a Xenon lamp (~60 mW/cm^2 between 340 and 380 nm) and the photo-chemical reaction appeared to be completed after more than 9 hours of irradiation. At the Institute of Materials Research and Engineering a quasi-cw 355 nm laser (70 mW/cm^2) was used and the photo-cross-linking between H-CV(Bpa)VT-ol peptide and DMSO proven by mean of UV-Vis and FTIR spectroscopies; the photo-chemical reaction took about 6 hours to complete.

2.4 Photo-Irradiation of Bpa-Containing Peptide Capped Gold Nanoparticles

2.4.1 Conjugation with Bpa-Containing Peptide

Once the conditions for the photo-cross-linking reaction to take place had been established, gold nanoparticles were functionalized with a mixed self-assembled monolayer (SAM) consisting of H-CVV(Bpa)T-ol peptide and polyethylene glycol alkanethiol molecule. GNPs functionalization was done aiming to have nanoparticles stable under the irradiation conditions in which the photo-cross-linking reaction was expected to take place (based on the experiments with the H-CV(Bpa)VT-ol peptide in DMSO), while inserting the highest possible amount of Bpa-containing peptide into the ligand shell.

Duchesne et al.[11] designed self-assembled monolayers (SAMs) for GNPs functionalization constituted of polyethylene glycol alkanethiol and peptidol, i.e. a modified peptide bearing on the C-terminal carbon an alcohol functional group instead of a carboxylic group. The peptide modification was introduced in order to avoid nonspecific interactions between the otherwise negatively charged carboxylic acid and positive charges on biological molecules. Moreover, for negatively charged groups, because of the repulsion between them, the SAM packing density, hence compactness, on the gold surface is lower. In the manuscript, several peptidol and polyethylene glycol alkanethiol combinations were tried and their stability tested in different ways, e.g. electrolyte-induced aggregation. It was found that a mix-layer, constituted of H-CVVVT-ol (i.e. Cys-Val-Val-Val-Thr-ol) and HS-EC_{11}-EG_4 (referred to hereafter as PEG) in 70:30 ratio, called "mix-matrix", provides the GNPs with a highly packed monolayer resistant to electrolyte-induced aggregation and ligand exchange.

This self-assembled monolayer "mix-matrix" was used as reference for the functionalization of GNPs with Bpa-containing peptide; a mixed SAM consisting of H-CVV(Bpa)T-ol and PEG in a 70:30 ratio was found to be stable.

First, GNPs of 5 nm in diameter were chosen because small nanoparticles are generally easier to stabilize. Second, the Bpa-containing peptide with the Bpa amino acid further away from the gold surface, i.e. H-CVV(Bpa)T-ol, was the first one tested in order not only to avoid quenching by the gold core, but also to maximize the chances of photo-cross-linking either with other ligands or with DMSO solvent. Third, because of the molecules' hydrophobicity, 1X phosphate buffered saline (PBS) and 0.005% Tween20 (T20) (v/v) were used to obtain well-dispersed solutions of GNPs and the monolayer resistance to ligand exchange was tested in their presence (**Fig. 2.12**). However, PBS and Tween20

prevented the use of MS and IR techniques to detect the ligands onto the gold surface (see **Sections 2.4.2** and **2.4.3**) thus, to characterize the gold surface, H-CVV(Bpa)T-ol:PEG (70:30) capped GNPs were conjugated in the presence of 1X PBS, but then purified from the ligand excess using just water. The two conjugation strategies are described in the **Methods** section.

As previously observed,[18] when forming a SAM on the gold surface, a shift in the plasmon band is observed because of the change in surface dielectric constant (here of 6 nm for the GNPs in the presence of 1X PBS and 0.005% T20 v/v, **Fig. 2.11**). The normalized UV-Vis spectrum of H-CVV(Bpa)T-ol:PEG (70:30) capped GNPs in water (**Fig. 2.11**) shows a more broadened plasmon band in comparison to the one corresponding to the GNPs in the presence of 1X PBS and 0.005% Tween20 v/v, suggesting that Tween20 prevents the hydrophobic interactions between the peptides. The pictures in **Fig. 2.11** (**bottom**) show nanoparticles just in water kept in a glass vial (**A**) to avoid adhesion to plastic walls and illustrate a sedimentation over 3-4 hours (**B-C**), possibly driven by hydrophobic interactions and formation of β-sheets among the peptides; the nanoparticles were resuspended by shaking (**D**).

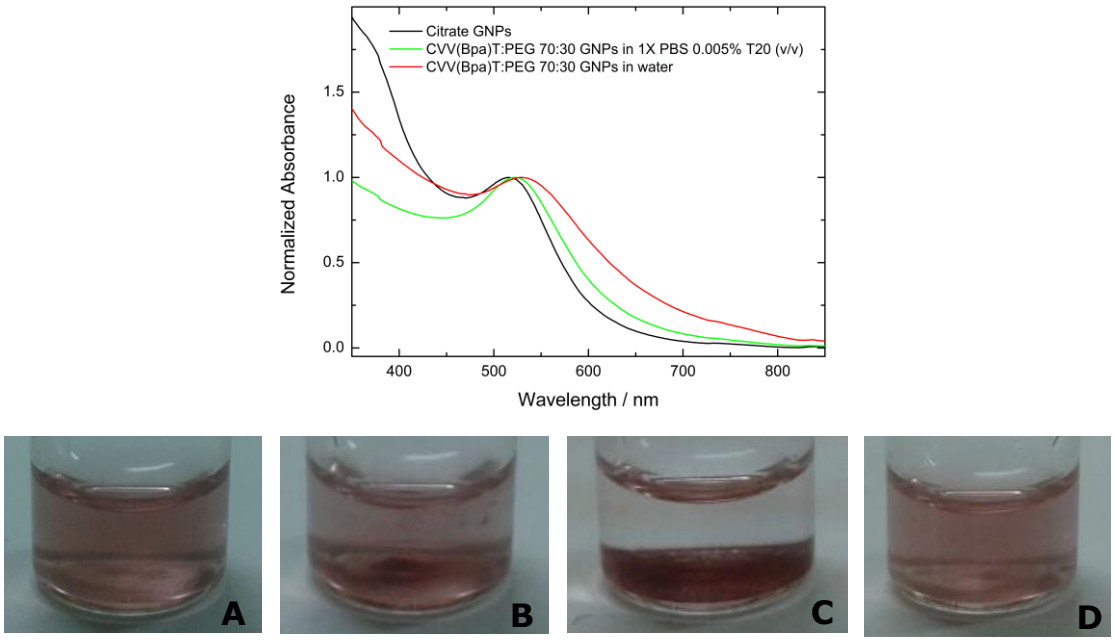

Fig. 2.11 – Normalized UV-Vis spectra of citrate and H-CVV(Bpa)T-ol:PEG (70:30) capped GNPs in the presence or absence of 1X PBS and 0.005% Tween20 (final concentration, v/v). **Bottom:** pictures illustrating H-CVV(Bpa)T-ol:PEG (70:30) capped 5 nm GNPs in water sedimenting over 3-4 hours (**A-C**) and resuspended by shaking (**D**).

It is well known that the SAM, bound to the gold surface through a covalent Au-S bond,[19] can dissociate when the particles are incubated in the presence of

an excess of free thiol ligand, such as mercaptoethanol (ME) and dithiothreitol (DTT), which will replace the initial SAM.[20] If the GNPs are incubated in the presence of NaCl, they will eventually aggregate during the ligand exchange process.

Demers et al.[21] and Nicewarner Pena et al.[22], for example, incubated fluorophore labeled oligonucleotides-capped GNPs in mercaptoethanol and PBS. ME was used to displace the oligonucleotides from the GNPs in a ligand exchange reaction, whereas the NaCl in PBS was necessary to trigger the GNPs' aggregation during the ligand displacement process. After removal of the GNPs aggregates, they quantified the fluorophore labeled oligonucleotides previously bound to the gold surface. Wilson et al.[23] tested the stability of biotinylated dextran-capped GNPs in typical PCR (polymerase chain reaction) conditions, i.e. a DTT containing buffer. GNPs are indeed interesting labels for biological applications, but their use can be limited by their instability in the presence of endogenous free thiol-containing molecules. In Chen et al.,[24] GNPs ligand shell resistance to ligand exchange was assessed by incubation of capped GNPs with different concentrations of dithiothreitol (DTT) in the presence of 0.5 M NaCl.

The resistance to ligand exchange of the H-CVV(Bpa)T-ol:PEG (70:30) monolayer was compared to the one of "mix-matrix" and PEG SAMs on 5 nm GNPs. The UV-Vis spectra of each sample were taken after different incubation times in a range of DTT concentrations and 0.5 M NaCl; an aggregation parameter (AP) was defined as A_{650nm}/A_{520nm} where A_{650nm} and A_{520nm} were the absorbance at 650 and 520 nm, respectively. The normalized aggregation parameters, corresponding to the AP divided by the AP of the control experiment, i.e. using neat water instead of DTT, are shown in **Fig. 2.12** (see **Methods** section for details).

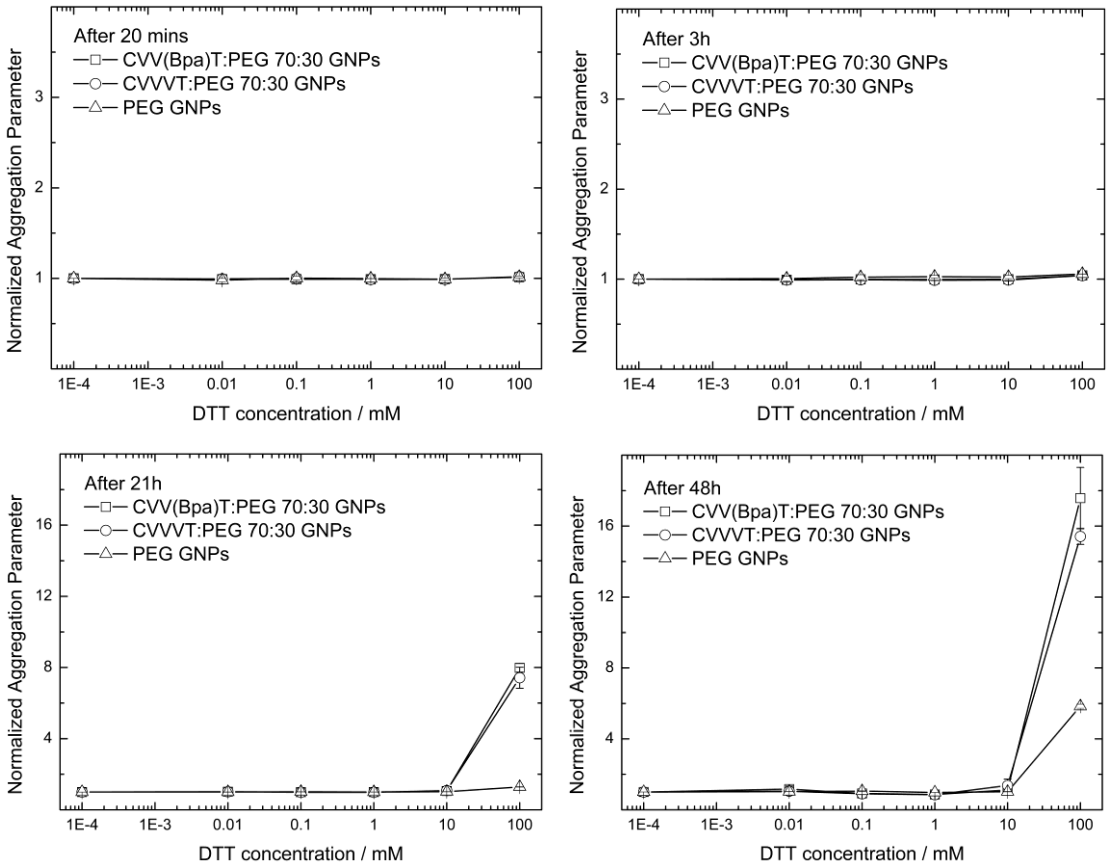

Fig. 2.12 – Resistance to ligand exchange of H-CVV(Bpa)T-ol:PEG (70:30), H-CVVVT-ol:PEG (70:30) and PEG capped 5 nm GNPs in 1X PBS and 0.005% Tween20 v/v after different incubation times (20 min, 3h, 21h, 48h) in a range of DTT concentrations (from 0.01 mM to 100 mM, final concentrations) and 0.5 M NaCl. The Normalized Aggregation Parameter is defined as the ratio between the absorbance at 650 and 520 nm divided by the corresponding ratio of the control experiment, i.e. using neat water instead of DTT.

The "mix-matrix" GNPs aggregated at the highest concentration of DTT after 21h. The results obtained for the "mix-matrix" GNPs are in agreement with those previously reported in literature,[24] where the high stability given by this mixed SAM is explained by its high packing density, i.e. H-CVVVT-ol is at 3.6 peptides/nm^2.[11] Considering that disruption of the SAM by the large benzophenone group would be expected, it is interesting that the H-CVV(Bpa)T-ol:PEG (70:30) monolayer has a stability, and should therefore have a packing density, comparable to "mix-matrix". A possible explanation for the similar stability, despite the larger size of the side chain of Bpa-containing peptide, could be that the benzene rings of the Bpa amino acid lead to the formation of β-sheets that drive the self-assembly and stabilize the hydrophobic core of the monolayer. Chen et al. have indeed previously reported the extremely high stability (even higher than the "mix-matrix" SAM) to ligand exchange of SAMs constituted of peptidols with aromatic amino acids, i.e. H-

CFFFY-ol or H-CFFFT-ol, and PEG, indicating that aromatic and alkyl chains can form an extremely compact monolayer through hydrophobic interactions and, possibly, well-defined secondary structure motifs.[24] Moreover, the fact that the resistance to ligand exchange of a SAM constituted of only PEG is greater than that of the mixed SAMs suggests that the peptidols are indeed within the monolayer.

2.4.2 Characterization by LDI-MS

As discussed in Chapter 1, Laser Desorption Ionization Mass Spectrometry (LDI-MS) is a powerful technique to characterize the gold nanoparticles' surface. When Yan et al. analyzed GNPs functionalized with two different molecules, they identified not only thiol and disulfide ions corresponding to both ligands, but also mixed disulfide ions.[25]

Therefore, based on Rotello's papers,[25,26] LDI-MS is an interesting technique to further demonstrate the presence of both H-CVV(Bpa)T-ol and PEG ligands within the SAM and, potentially, to understand whether the photo-cross-linking reaction of the benzophenone molecule did occur.

In order to characterize the surface of capped GNPs by LDI-MS, different samples and conditions (e.g. different concentrations and pHs) were tested. Importantly, GNPs solutions had to be in the absence of Tween20, otherwise a multitude of peaks corresponding to several oligomers was observed and prevented the identification of the ions of interest.

First, MALDI-MS analysis, i.e. without the gold, but with α-CHCA organic matrix, of H-CVV(Bpa)T-ol peptide and PEG molecule, was performed (**Fig 2.13**) and the ions' molecular structures, corresponding to the peaks found, identified (**Scheme 2.2** and **2.3**).

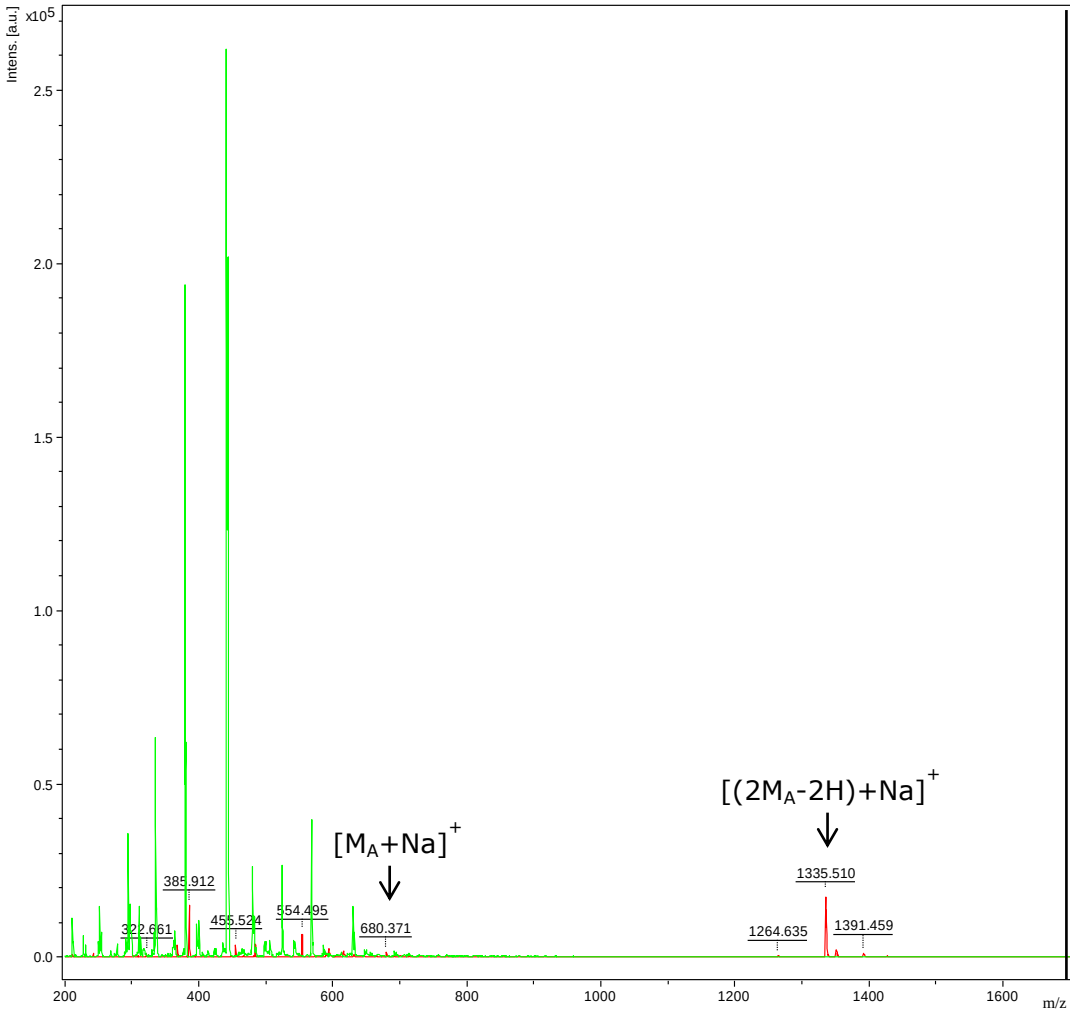
Intens. [a.u.]
x10^5
2.5
2.0
1.5
1.0
0.5
0.0
200
400
600
800
1000
1200
1400
1600
m/z
[M_A+Na]^+
[(2M_A-2H)+Na]^+
385.912
322.661
455.524
554.495
680.371
1335.510
1264.635
1391.459

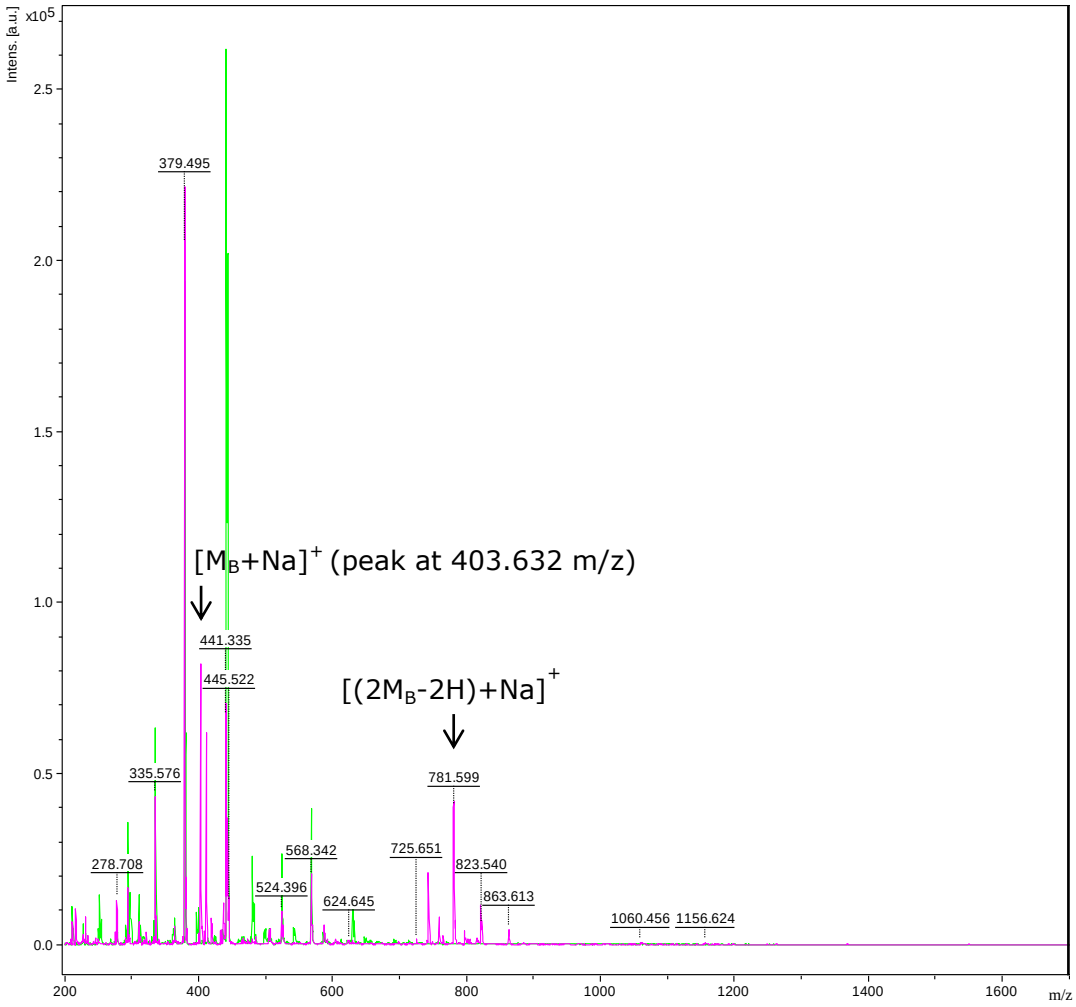

Fig. 2.13 – Top: MALDI-MS spectra of H-CVV(Bpa)T-ol peptide (M_A) mixed with an organic matrix (red) and α-CHCA organic matrix (green). **Bottom:** MALDI-MS spectra of HS-$EC_{11}EG_4$ (M_B) molecule mixed with an organic matrix (magenta) and α-CHCA organic matrix (green). M_A and M_B refer to the neutral peptide and PEG molecule, respectively. Hence, $[M_{A/B}+H]^+$ refers to the protonated species. $(2M_{A/B}-2H)$ refers to two molecules covalently bound together through a disulfide bond, hence $[(2M_{A/B}-2H)+H]^+$ refers to the protonated dimer.

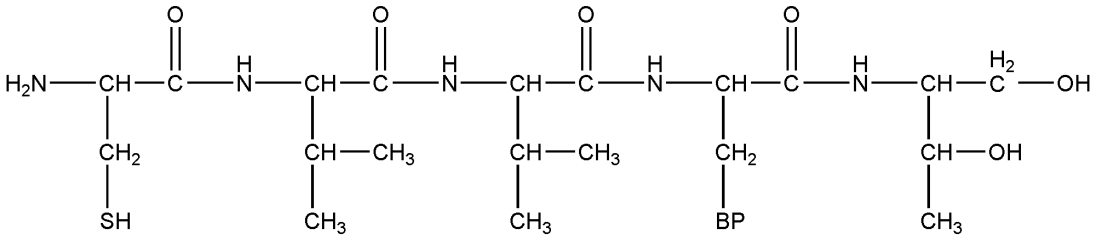

H-CVV(Bpa)T-ol peptide (M_A); Exact Mass: 657.32 Da

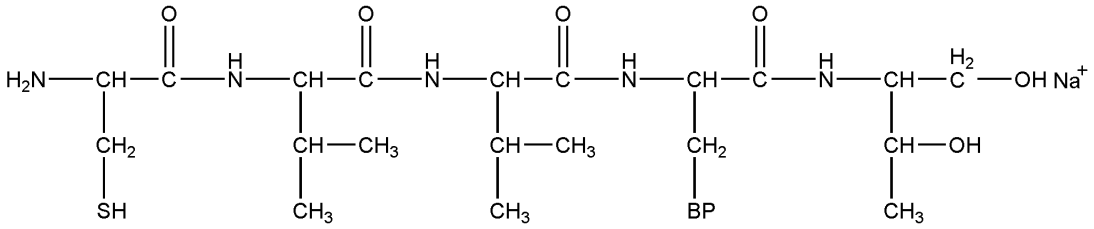

$[M_A+Na]^+$; Exact Mass: 680.31 Da

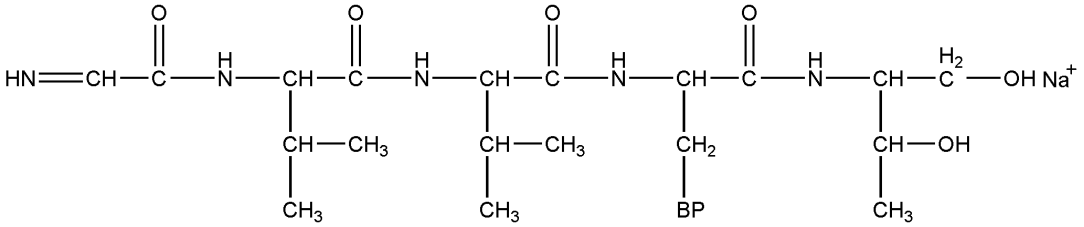

$[M_A+Na-CH_3SH]^+$; Exact Mass: 632.31 Da

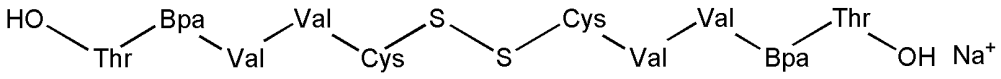

$[(2M_A-2H)+Na]^+$; Exact Mass: 1335.61 Da

Scheme 2.2 – Predominant ligand ions of H-CVV(Bpa)T-ol peptide observed in MALDI and LDI spectra. BP stands for benzophenone molecule.

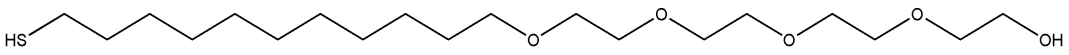

$HS\text{-}EC_{11}\text{-}EG_4$ (M_B); Exact Mass: 380.26 Da

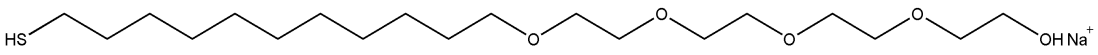

$[M_B+Na]^+$; Exact Mass: 403.25 Da

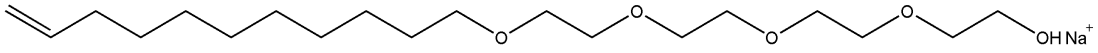

$[M_B+Na\text{-}H_2S]^+$; Exact Mass: 369.26 Da

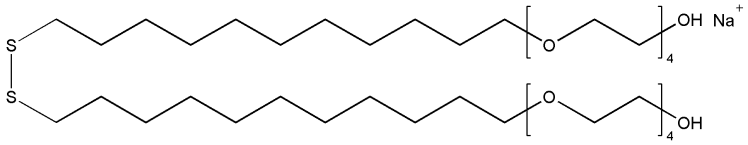

$[(2M_B\text{-}2H)+Na]^+$; Exact Mass: 781.49 Da

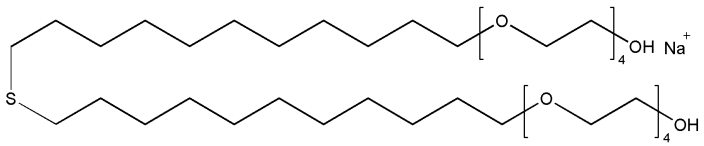

$[2M_B+Na\text{-}SH\text{-}H]^+$; Exact Mass: 749.52 Da

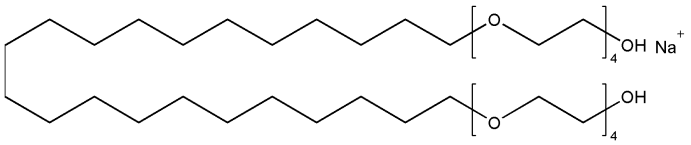

$[2M_B+Na\text{-}2SH]^+$; Exact Mass: 717.55 Da

Scheme 2.3 – Predominant ligand ions of $HS\text{-}EC_{11}\text{-}EG_4$ molecule observed in MALDI and LDI spectra.

H-CVV(Bpa)T-ol:PEG (70:30) capped ~5 nm GNPs were then analyzed by LDI-MS (**Fig. 2.14**).

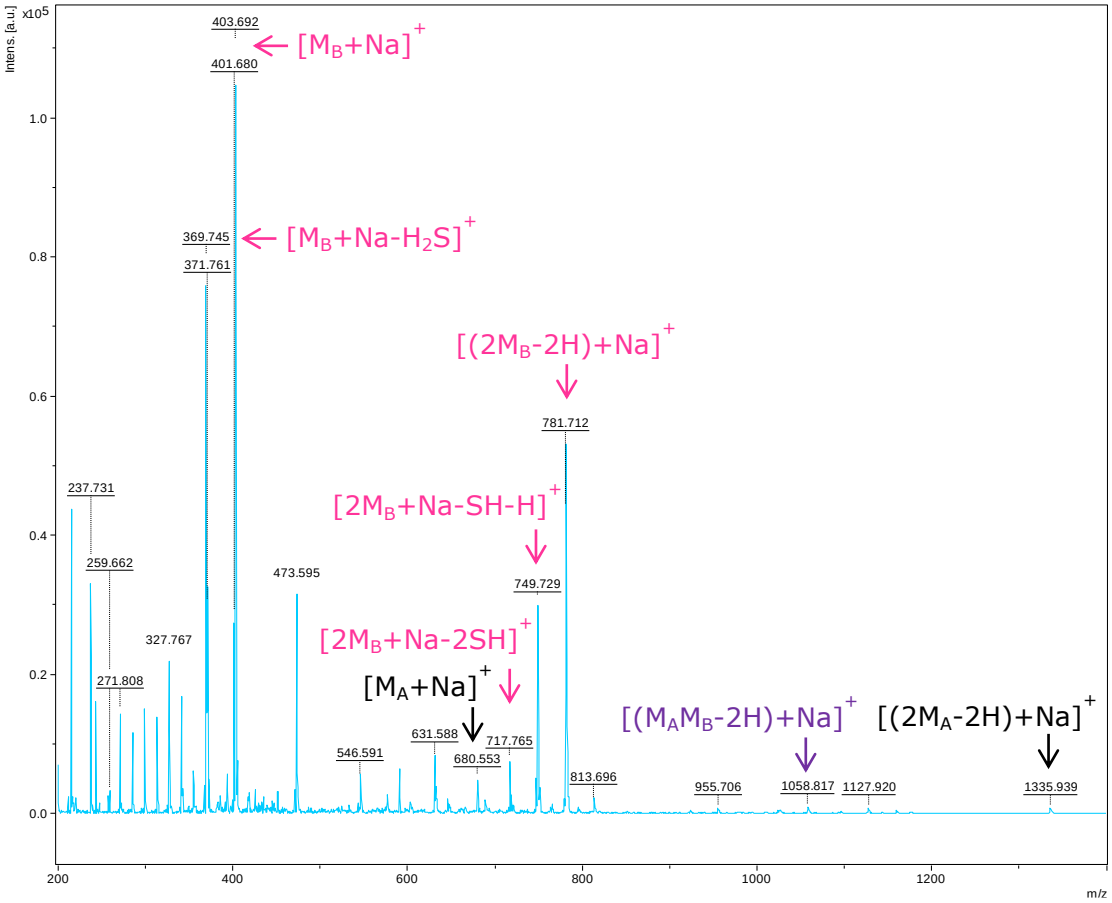

Fig. 2.14 – LDI-MS spectrum of H-CVV(Bpa)T-ol:PEG (70:30) capped ~5 nm GNPs in water with citrate buffer (pH=4.6). PEG (M_B) ions are shown in pink, peptide (M_A) ions in black and mixed disulphide peptide-PEG in purple. (M_AM_B-2H) refers to a peptide and PEG molecule bound together through a disulfide bond, hence $[(M_AM_B\text{-}2H)+H]^+$ refers to the protonated mixed peptide-PEG dimer.

Some observations can be made on the spectrum shown in **Fig. 2.14**. First, ions corresponding to each ligand have been identified, but the signal intensities of the two molecules are not what is expected based on the ratio used during the synthesis, i.e. H-CVV(Bpa)T-ol:PEG (70:30). However, this is not necessarily an indication for the ratio of ligands to be different, since ionization efficiency could be different. Yan et al. have in fact observed something similar.[25] They analyzed GNPs capped by a mixed monolayer consisting of two PEG molecules bearing either a terminal alcohol or ammonium group, called TEGOH and TTMA, respectively. NMR was used to independently determine the ratio of the two ligands on the GNPs surface: 17% TTMA and 83% TEGOH. However, MS analysis revealed signal intensities significantly higher for TTMA ligand, suggesting not only that the ionization efficiency of two ligands can be different, but also that

the more ionized one might suppress the ionization of the other ligand. Also, it is worth noting that TEGOH molecule is the same PEG molecule used in this study and that the ions found by Yan et al. are the same ones identified here. Furthermore, in order to enhance the peptide ionization, citrate acidic buffer (pH=4.6) was added to the sample because positively charged species fly better to the detector. Also, it is not surprising that the ions observed are mainly sodium adducts, especially for the PEG molecule, since ethylene glycol units have a great affinity for sodium.[25,27] Second, and more interestingly, the spectrum shows disulfide ions for both peptide and PEG ligands, but also a mixed disulfide peak at 1058.8 m/z, i.e. $[(M_AM_B\text{-}2H)+Na]^+$. This peak confirms that these two molecules are on the same gold core (maybe adjacent?) because, as previously reported,[25] mixed disulfide ions can be observed only when two molecules are on the same gold core; they have not been detected when a sample of GNPs capped by the molecule "A" was mixed to one capped by the molecule "B".

LDI-MS was chosen not only to demonstrate the presence of both H-CVV(Bpa)T-ol and PEG ligands within the SAM, but also to detect any photo-chemical modification which may have occurred upon UV irradiation. Hence, UV-irradiated H-CVV(Bpa)T-ol:PEG (70:30) capped ~5 nm GNPs were analyzed by LDI-MS (spectra not shown). However, it should be noted that it is not possible to distinguish between disulfides with or without an additional cross-link formed by the benzophenone group upon photo-cross-linking reaction; in other words the exact mass of disulfides in which the photo-cross-linking reaction did or did not occur is the same (see benzophenone cross-linking mechanism in **Scheme 2.1**). The photo-cross-linking reaction would be verified if two peptides or one peptide and one PEG molecule were cross-linked together and were coming off the gold surface as non-disulfide ions. These ions would have a mass of 2 Da higher than the disulfides, but because of the isotopic distribution of carbon atoms their main peak would overlap with the signal corresponding to the disulfide ion having two ^{13}C atoms; however, in the spectra, no clear indication for the formation of photo-cross-linked non-disulfide ions was observed. Also, it is highly probable that, if photo-cross-linking occurred, the two molecules covalently bound together would also have formed a disulfide bond upon ionization. Thus, LDI-MS can characterize the GNPs' surface and potentially answer the question of ligand proximity on the gold surface, but cannot prove the photo-cross-linking upon UV irradiation.

2.4.3 Characterization by FTIR

In order to use FTIR spectroscopy, it was found that the GNPs had to be just in water, otherwise peaks corresponding to Tween20 and phosphate species were dominating over those associated with the molecules on the gold surface.

To characterize H-CVV(Bpa)T-ol:PEG (70:30) capped GNPs, several drops (0.12 μM GNPs) were successively dried on the same spot on a CaF_2 window (for sample preparation and measurement details, see **Instruments** section). Picture in **Fig. 2.15, bottom** shows part of the dried sample as it looks in the visible microscope. In the GNPs spectra shown in the **top** of **Fig. 2.15**, bands corresponding to both H-CVV(Bpa)T-ol and PEG are present. For the H-CVV(Bpa)T-ol peptide, the amide II, corresponding to coupled C-N stretch and N-H bend, is at ~1550 cm^{-1}, whereas the benzophenone ketone carbonyl[16] it at ~1650 cm^{-1} and strongly overlaps with the amide I band (1630-1660 cm^{-1} region), corresponding to C=O stretch. The peak at ~1630 cm^{-1} could indicate the formation of β-sheets between aggregates of peptides upon drying. For the PEG molecule, the multiple bands at ~2800 cm^{-1} correspond to alkyl C-H stretch and those between 1350 and 1480 cm^{-1} to alkyl C-H bending. The bands between 1060 and 1280 cm^{-1} correspond to C-O stretch in ethers.

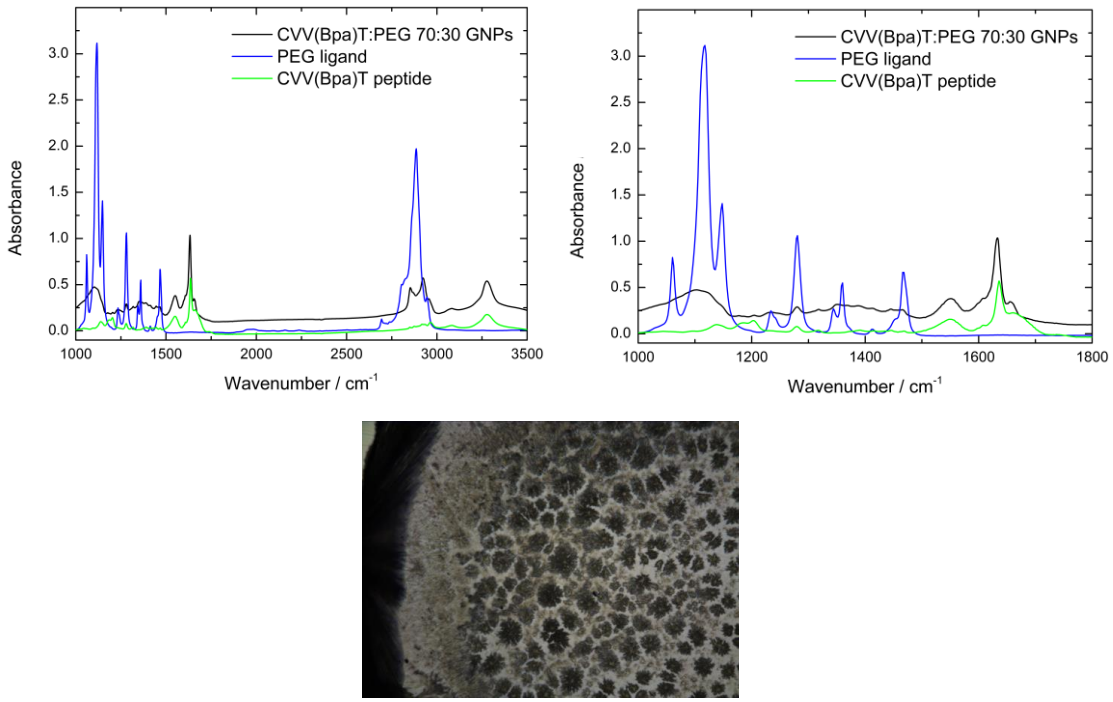

Fig. 2.15 – Top left: FTIR spectra of H-CVV(Bpa)T-ol:PEG (70:30) capped ~5 nm GNPs, dried from a water suspension, and of free PEG and H-CVV(Bpa)T ligands. **Top right:** Zoom of the region between 1000 and 1800 cm^{-1}. **Bottom:** Image of random 125 μm x 125 μm area of the dried H-CVV(Bpa)T-ol:PEG (70:30) capped ~5 nm GNPs spot.

Therefore, FTIR spectroscopy allowed the characterization of the surface of GNPs functionalized by two different molecules. However, because the inhomogeneous drying of the sample causes peaks intensity fluctuations, this technique is not suitable to detect the photo-cross-linking reaction occurring over time, i.e. a decrease in the carbonyl band of the benzophenone molecule at 1650 cm^{-1} and/or an increase in the band at 1140 cm^{-1}, corresponding to the formed tertiary alcohol group.

2.4.4 Characterization by FTIR in Solution

As previously discussed, if upon UV irradiation the photo-cross-linking reaction occurs, the ketone carbonyl in the benzophenone molecule gets modified into a tertiary alcohol group (**Scheme 2.1**). Therefore, in the FTIR spectrum, a decrease in the band associated with the benzophenone ketone carbonyl and the development of a band corresponding to a tertiary alcohol group are expected. As for the former, literature values[16] and FTIR spectra of H-CVV(Bpa)T-ol:PEG (70:30) capped 5 nm GNPs (**Fig. 2.15, top**) have shown that it strongly overlaps with the peptide amide I band (1630-1660 cm^{-1} region), i.e. it is at 1650-1670 cm^{-1}. Moreover, from the FTIR spectra of H-CV(Bpa)VT-ol peptide in DMSO (**Fig. 2.9, top left**), it was evident that CaF_2 windows absorbed moisture from the surrounding environment over time, which was then released to DMSO, and caused a strong absorbance at the very same position. Thus, the photo-cross-linking reaction cannot be validated by the benzophenone ketone carbonyl band. As for the tertiary alcohol group band, FTIR spectra of H-CV(Bpa)VT-ol peptide in DMSO (**Fig. 2.9, top right**) clearly showed a band corresponding to the product of the photo-cross-linking reaction, i.e. a tertiary alcohol group, whose C-O stretch is at ~1140 cm^{-1}. Hence, the photo-cross-linking reaction on the gold nanoparticles' surface could be demonstrated by the detection of this band.

DMSO was chosen as a solvent for H-CVV(Bpa)T-ol:PEG (70:30) capped 5 nm GNPs not only because the GNPs were found to resuspend in DMSO better than in water after lyophilisation (see sample preparation details in **Methods** section), probably because of the otherwise strong hydrophobic interactions among nanoparticles (**Fig. 2.11, bottom**), but also because it has only weak absorbance at 1140 cm^{-1}, i.e. the wavelength corresponding to the tertiary alcohol photo-reaction product. Moreover, the use of DMSO solvent was judged to maximize the chances to demonstrate a photo-cross-linking on the GNPs' surface, since the Bpa-containing peptide, upon UV irradiation, could cross-link

not only to adjacent ligands, but also to DMSO, as observed in solution (**section 2.3**). Such cross-linking of DMSO with Bpa-containing peptides bearing the Bpa amino acid at different positions along the peptide chain (**Fig. 2.5-2.7**) could potentially probe the accessibility of the solvent within the monolayer.

Similarly to the results obtained at the University of Liverpool and discussed in **section 2.3**, with the light source used at the Institute of Materials Research and Engineering in Singapore (see **Instruments** section for details), the photo-cross-linking reaction between H-CV(Bpa)VT-ol peptide and DMSO took about 6 hours to complete and was validated by means of UV-Vis and FTIR spectroscopies. Considering that the quantum yield of the photo-reaction on the gold nanoparticle surface could be significantly lower than in solution (i.e. lower than 0.3%), longer UV irradiation was carried out.

The UV-Vis spectra of H-CVV(Bpa)T-ol:PEG (70:30) capped 5 nm GNPs in DMSO upon UV irradiation (**Fig. 2.16**) show a decrease in absorbance, hence concentration, over time, most likely due to some sample sedimentation. More interestingly, the nanoparticles were found not to aggregate over UV irradiation: the plasmon band is not broadening and not shifting (small shifts are difficult to quantify because of the noise).

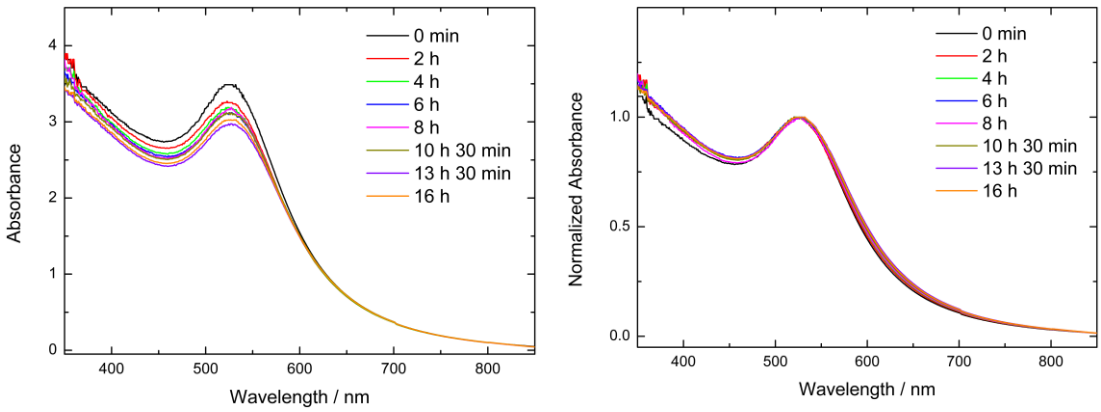

Fig. 2.16 – Not normalized (**left**) and normalized (**right**) UV-Vis spectra at different irradiation times of 25.5 μM H-CVV(Bpa)T-ol:PEG (70:30) capped 5 nm GNPs in DMSO (path length 150 μm). Irradiation was performed at IMRE in Singapore using a quasi-cw 355 nm laser with 7 ns pulse duration and 10 kHz repetition rate.

From the UV-Vis spectrum of the sample before irradiation, a gold nanoparticle concentration of 25.5 μM was calculated; therefore, assuming a peptide capping density of 3.6 peptides/nm^2, i.e. the same as H-CVVVT-ol peptide,[11] since both "mix-matrix" and H-CVV(Bpa)T-ol:PEG (70:30) monolayers showed comparable resistance to ligand exchange (**Fig. 2.12**), and that the ratio of peptide and PEG ligands reflected the one used during the conjugation, i.e.

70:30, a peptide concentration of ~5 mM was estimated. Hence, the IR band at ~1140 cm^{-1} corresponding to the photo-reaction product, which was clearly visible with a peptide concentration of 1.9 mM, as shown in **Fig. 2.9, top right**, should be detectable. It is worth noting that only part of the sample was effectively irradiated (see large absorbance at 350 nm), but that both the high peptide concentration and long irradiation time did probably compensate for the non-uniform irradiation.

The IR spectra, resulting from the subtraction of the spectrum before irradiation (0 min) from the spectra at different irradiation times and in the region of the C-O stretch of a tertiary alcohol group,[17] are reported in **Fig. 2.17, top**. The band at ~1140 cm^{-1} is ascribed to spectral features associated to the disappearance of the band at 1150 cm^{-1}, corresponding to the C-O stretch in the PEG molecule's ether groups (also observed in the FTIR spectra reported in **Fig. 2.15**); this band is more clearly visible in **Fig. 2.17, bottom**, where the DMSO spectrum was subtracted from all the spectra. As shown by the UV-Vis spectra in **Fig. 2.16**, the GNP concentration decreased over time hence, caused the decrease in absorbance at 1150 cm^{-1}, leading to artifacts when subtracting the spectrum before irradiation from the spectra at different irradiation times. Moreover, the fact that spectra taken after night show an increase in the band at ~1140 cm^{-1} rule out the possibility that this band is actually illustrating the occurrence of the photo-cross-linking reaction.

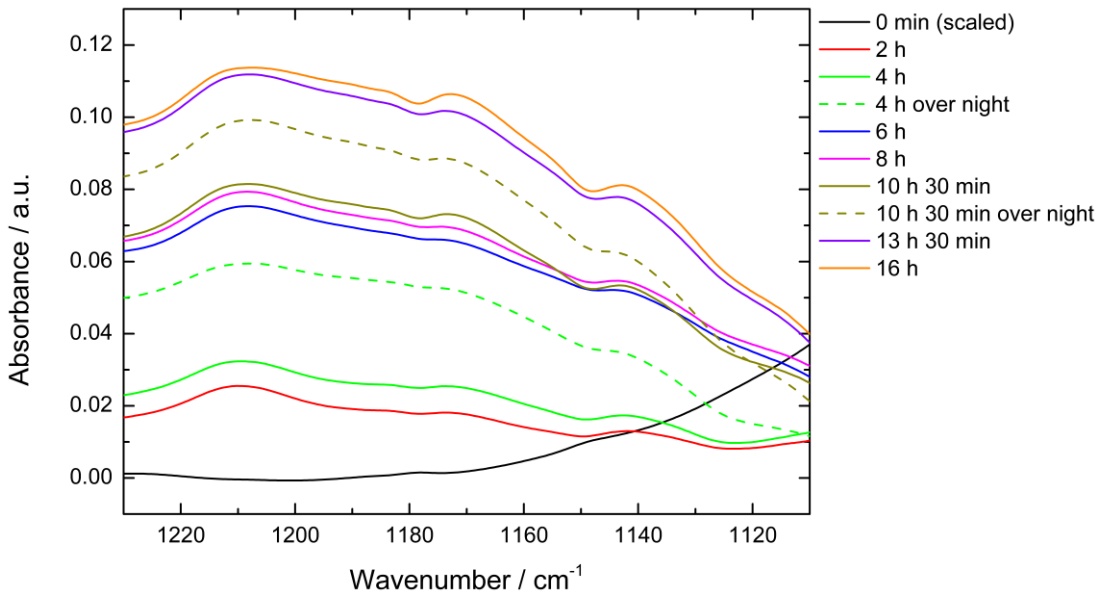

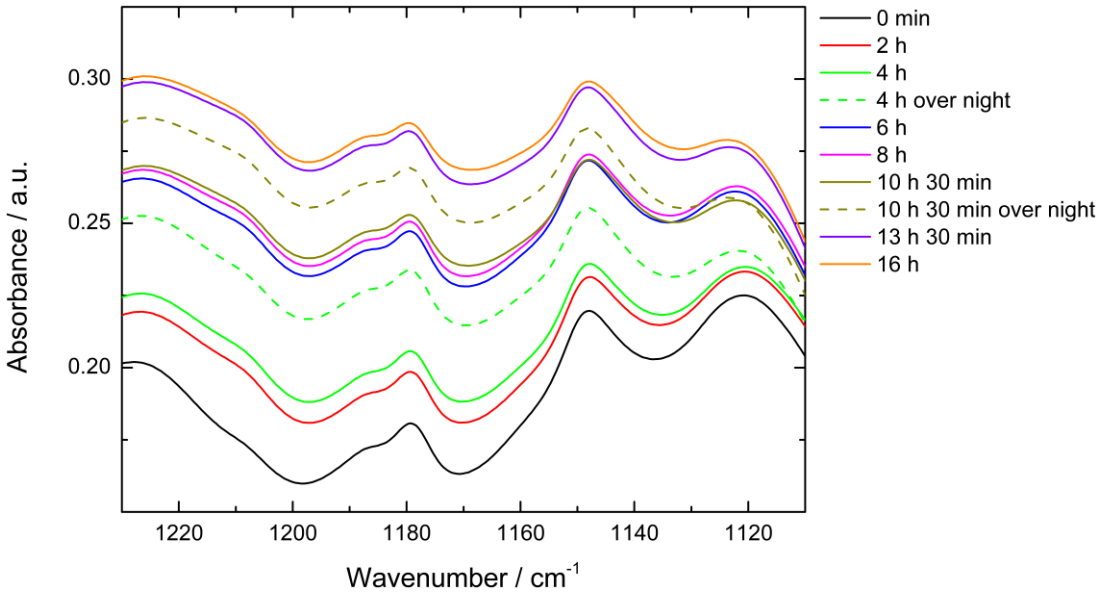

Fig. 2.17 – Difference FTIR spectra of 25.5 μM H-CVV(Bpa)T:PEG (70:30) 5 nm capped GNPs in DMSO after different irradiation times in the tertiary alcohol group region. **Top:** Spectrum of the sample before irradiation (0 min) subtracted from the spectra at different irradiation times; **Bottom:** DMSO spectrum subtracted from all the spectra. The "over night" comment refers to the spectra of the sample irradiated for 4h and 10h 30 min taken after night.

Thus, the tertiary alcohol band was not detected in the FTIR spectra of H-CVV(Bpa)T-ol:PEG (70:30) 5 nm capped GNPs in DMSO even after 16 hours of irradiation, indicating that no significant photo-cross-linking had taken place.

2.4.5 Conclusions

In this chapter, the photo-cross-linking reaction between H-CV(Bpa)VT-ol peptide and DMSO was demonstrated by means of UV-Vis, FTIR and MS techniques; all the results, over the different irradiation times, correlated well and the quantum yield was found to be very low, i.e. lower than 0.3%. The appropriate protocol to functionalize GNPs with a mixed monolayer constituted of H-CVV(Bpa)VT-ol peptide and PEG in a 70:30 ratio was developed, and FTIR spectroscopy and Laser desorption Ionization Mass Spectrometry (LDI-MS) proved the presence of both ligands on the gold nanoparticles' surface. For the reasons detailed above, FTIR in solution was chosen as the key technique to investigate the occurrence of photo-cross-linking at the gold nanoparticles' surface, that was finally not detected in the irradiation conditions in which was expected to take place.

It is worth remarking that the possibility to photo-modulate the nanoparticles' properties with high spatial and temporal control have previously led to studies in which nanoparticles have been functionalized with a monolayer

containing a photo-activable molecule.[28] The light irradiation, by triggering a change in the molecular properties of the photo-activable molecule, can lead to modifications in the nanoparticle properties.

A key point for such studies is that the photo-chemical reactions have to occur fast enough in order to avoid the quenching of the process by energy transfer to the gold core. Zhang et al.,[29] for instance, investigated the photo-isomerisation of azobenzene on 2.5 nm GNPs. The azobenzene was bound to alkane molecules of different chain lengths in order to study the dependence of the photo-isomerisation on the photo-chrome-gold distance; they asserted that the quenching of the photo-chemical reaction by the gold core is "distance-dependent through-bond"., they observed a strong reduction in the *trans-cis* conversion upon 350 nm irradiation if the azobenzene molecule was separated from the metal core by only 4 or 6 methylene groups, i.e. ~6 and 9 Å, respectively, but much less for longer linkers, i.e. 9 and 12 corresponding to ~14 and 18 Å, respectively. The *cis-trans* isomerisation of azobenzene was also exploited by Grzybowski's group[30] which functionalized ~5 nm GNPs with dodecylamine (DDA) and (11-mercaptoundecanoxy)azobenzene (MUA) and embedded them in an organic gel to create a rewritable and self-erasing material. When the azobenzene was in the *trans* form, the particles were red and monodispersed inside the gel. Upon 365 nm UV light irradiation (10 mW/cm^2) for periods of time varying from 0 to 10 sec, the azobenzene was switched into the *cis* form which presents a larger dipole moment: NP aggregates of 150 nm size were formed because of the increased dipole-dipole interactions and the color observed was now blue. The authors have been able to write and draw on the gel by applying UV masks. Exposure to visible light photo-switched the azobenzene back to the *trans* form and aggregates (and therefore writings and drawings) were no longer observed. This photo-switching process has been carried out for over 300 times. In their case, the distance to the gold surface was ~15 Å. Also, Ipe et al.[31] functionalized 2 nm GNPs with an alkyl chain presenting 5 methylene groups and the spiropyran molecule at one end. By photo-switching the ring opening-closure reaction, they were able to photo-modulate not only electrostatic interactions between the spiropyran, in its opened form, and various amino acids, but also the release of the residue upon ring closure, even though the photo-chemical molecule was at a distance from the gold surface of only ~6 Å.

In the case of the H-CVV(Bpa)T-ol peptide, the benzophenone photo-activable molecule can be estimated to be at least at ~10 Å from the 5 nm gold nanoparticles' surface. Thus, a possible explanation, for the fact that the photo-

cross-linking reaction was not observed on the gold nanoparticles' surface in the irradiation conditions in which was expected to take place, has probably not be traced in a complete quenching of the reaction from the gold core, but in a quantum yield significantly lower than the one for the photo-reaction between the free peptide and DMSO, which, as previously discussed, was already very low (i.e. lower than 0.3%). Moreover, a transient electron transfer between the Bpa-containing peptide (in its diradicaloid triplet state) and the GNP can be described as an alternative quenching mechanism. It has indeed been previously reported the efficient quenching occurring via electron transfer from conjugated polymers to GNPs up to 5 nm in size.[32] Thus, there was no evidence that the photoreaction did occur on the NP surface, even after 16 hours of irradiation.

Finally, the use of Bpa-containing peptide in this study did not provide insights into the molecular organization and compactness of mixed monolayers self-assembled on gold nanoparticles. However, we suggested, as also previously reported in the literature for monolayers of alkane thiols,[25] that LDI-MS can provide interesting information about ligands proximity within mixed SAMs on GNPs.

2.5 Materials and Methods

2.5.1 Materials

All peptides (H-C(Bpa)VVT-ol, H-CV(Bpa)VT-ol, H-CVV(Bpa)T-ol, H-CVVVT-ol) were purchased from Peptide Protein Research Ltd. PEGylated alkanethiol HS-EC_{11}-EG_4 (referred to as PEG) was purchased from ProChimia (ProChimia Surfaces Sp. z.o.o., Sopot, Poland). All the chemicals were purchased from Sigma Aldrich, including the standards (Des Arg Bradykinin, Angiotensin, Neurotensin, ACTH 1-17, ACTH, ACTH 7-38) and the α-CHCA (alpha-cyano-4-hydroxycinnamic acid) matrix used in MALDI experiments. 5 nm commercial gold nanoparticles were purchased from BBI Solutions.

1 liter of phosphate buffered saline (PBS) stock solution (10X) was prepared by adding 80 g NaCl, 2 g KCl, 11.5 g Na_2HPO_4 and 2 g KH_2PO_4 to water.

All aqueous solutions were prepared using ultrapure water from a MilliQ system (Millipore Synergy system).

2.5.2 Instruments

At the University of Liverpool, **UV irradiation** at ~350 nm was performed using a Xenon lamp. The beam coming from the Xe lamp was going through a

water filter in a glass cell which cut off all light at wavelengths under 340 nm as well as IR-light; the beam was then reflected (R>0.95 in the spectral range 330-380 nm at 45 deg) by an unpolarised 2" XeF-Excimer Laser Mirror (purchased from H-CVI Laser Ltd) and focused through a lens on the sample. In the case of GNPs solutions, a GG400 filter cutting the visible component of the light and some of the short-UV-wavelengths was positioned in front of the quartz cuvette. H-CV(Bpa)VT-ol peptide in DMSO was irradiated with an intensity of ~60 mW/cm^2 between 340 and 380 nm in an IR cell between two CaF_2 windows with 150 and 50 μm spacers, whereas H-CVV(Bpa)T-ol:PEG (70:30) capped GNPs were irradiated with an intensity of ~20 mW/cm^2 between 340 and 380 nm in a quartz cuvette (path length of 1 cm) and an absorbance at the plasmon band of ~0.2 (results not shown).

At the Institute of Materials Research and Engineering in Singapore, a quasi-cw 355 nm laser with 7 ns pulse duration and 10 kHz repetition rate (specification: MPL-F-355-100 mW) was used for the **UV irradiation**. The definition of the laser as quasi-cw arose from the estimate that a 5 nm GNP absorbed about 7 photons per pulse which lasted 7 ns. Hence, the average time between two photons to get absorbed was 1 ns and, taking into account that a 5 nm GNP typically takes[33] ~10 ps to dissipate the photon energy into the surrounding environment, the peptide-capped gold nanoparticles had sufficient time to relax between two consecutive photons. The beam coming from the laser was going through a UV broadband beam expander (purchased from Edmund Optics TECHSPEC) that expanded its size while an aperture cut its edges; the final beam was 1 cm in diameter. The beam power measured at the sample position was 55 mW, hence 70 mW/cm^2 in intensity. Both H-CVV(Bpa)T-ol peptide in DMSO and H-CVV(Bpa)T-ol:PEG (70:30) capped GNPs were irradiated in an IR cell between two CaF_2 windows with 150 μm spacer.

UV-Vis spectra were recorded on a SpectraMax Plus 384 microplate spectrophotometer using a quartz SUPRASIL cuvette (path length of 1 cm) purchased from Hellma or a 384 well plate or on a Perkin Elmer Lambda 25 spectrophotometer using an IR cell with two CaF_2 windows (path length of 150 μm).

At the University of Liverpool, **FTIR** spectra in solution were recorded on a BioRad FTS-40 spectrometer with a HgCdTe (MCT) detector. All spectra were averaged over 500 scans and a resolution of 1 cm^{-1} was used. Before each measurement, the spectrometer chamber was purged with dry air for 30 minutes. 75 μL of 1.9 mM H-CV(Bpa)VT-ol peptide in DMSO were placed in an IR

cell between two CaF_2 windows with 150 and 50 µm spacers. The FTIR spectra were recorded before UV irradiation and after different irradiation times.

At the Institute of Materials Research and Engineering in Singapore, the **FTIR** spectra in solution of H-CV(Bpa)VT-ol peptide in DMSO were taken on a PerkinElmer Spectrum 2000 spectrometer. All spectra were averaged over 64 scans and a resolution of 1 cm^{-1} was used. 50 µL of 4 mM H-CV(Bpa)VT-ol peptide in DMSO were placed in an IR cell between two CaF_2 windows with a 150 µm spacer. The FTIR spectra were recorded before UV irradiation and after different irradiation times. The **FTIR** spectra in solution of H-CVV(Bpa)T-ol:PEG (70:30) capped 5 nm GNPs in DMSO were taken on a Bruker Vertex 80 spectrometer with an MIR-MCT detector. All spectra were averaged over 1000 scans, a scanner velocity of 20 kHz and a resolution of 1 cm^{-1} were used. The optics compartment was kept under vacuum, while the sample compartment was purged with nitrogen during the measurements to keep the system dry and the acquired spectra free of water vapor absorption as much as possible. 50 µL of 25.5 µM H-CVV(Bpa)T-ol:PEG (70:30) capped 5 nm GNPs in DMSO were placed in an IR cell between two CaF_2 windows with a 150 µm spacer. The FTIR spectra were recorded before UV irradiation and after different irradiation times.

FTIR Microscope spectra were recorded on a Bruker Lumos FTIR Microscope. The 8x objective was used for measurements in transmission mode. 6 drops of ~3 µl each of H-CVV(Bpa)T-ol:PEG (70:30) capped ~5 nm GNPs (0.12 µM) were successively dried onto the same spot of ~4 mm diameter on a CaF_2 window. Also, one drop of 2 mM H-CVV(Bpa)T and PEG ligands was investigated in the FTIR microscope. The spectra were taken over different random sample areas of 125 µm x 125 µm and an image captured. All spectra were averaged over 1000 scans and a resolution of 2 cm^{-1} was used.

ES TOF MS^+ (Electron Spray Ionization Time of Flight Mass Spectrometry) in a positive mode was performed on a Micromass Q-Tof micro mass spectrometer for H-CV(Bpa)VT-ol peptide in DMSO before and after UV irradiation.

A Bruker Daltonics Ultraflextreme Maldi TOF mass spectrometer was used for the **LDI-MS** (Laser Desorption Ionization – Mass Spectrometry) and **MALDI-MS** (Matrix Assisted Laser Desorption Ionization – Mass Spectrometry) analyses. It is equipped with a 337 nm laser and different laser powers were used when acquiring the spectra (always above 33% of the maximum laser power). All mass spectra were acquired in reflection positive-ion mode. 1 µl of 0.12 µM H-CVV(Bpa)T-ol:PEG (70:30) capped ~5 nm GNPs was spotted on the stainless steel sample target and left drying before LDI-MS analysis. In some cases, 2 µl of citrate acidic buffer (pH=4.6) were added to 8 µl sample in order to enhance

the peptide's flight to the detector. In the case of MALDI-TOF analysis, 10 mg of α-CHCA matrix were dissolved in 0.1% trifluoroacetic acid, 50% acetonitrile and 50% water. The solution was then vortexed, sonicated for 10 min and centrifuged for 15 min at 13500 rpm. 1 µl of matrix was then spotted on top of 1 µl sample on the target plate. In some cases, spectra were acquired in the *sum* mode, i.e. several single spectra were summed. The *sum* mode is useful in order to detect ions that are not flying very well to the detector and therefore would result in small intensity peaks. However, two associated issues are the increase in background noise and decrease in peak resolution.

Transmission Electron Microscopy analysis was performed using a Tecnai G2 Spirit BioTWIN at 120 kV. 200 mesh hexagonal copper grids were coated by pioloform (polyvinyl butyral). 5 µl of sample were spotted on the grid and left drying at room temperature.

2.5.3 Methods

Gold Nanoparticles Synthesis

Before the synthesis of gold nanoparticles, all the glassware and magnetic stirrer bars were cleaned with aqua regia, ethanol, and water and dried in an oven.

~5 nm gold nanoparticles were synthesized as described by Haiss et al.[34] While heating at ~ 110 °C, 1 ml of 1% wt $HAuCl_4$ was added to 90 ml of milliQ. The solution was stirred for 1 min. 2 ml of 38.8 mM trisodium citrate was added and the solution stirred for another minute. 1 ml of freshly prepared 0.075% (wt/v) $NaBH_4$ in 38.8 mM trisodium citrate was added and the mixture stirred for 5 min. The solution was stirred for additional 10 min while cooling.
Both UV-Vis spectra and TEM confirmed a size of ~5 nm, i.e. 5.7 ± 0.9 nm from TEM.

It should be noted that only the results shown in **Fig. 2.14, 2.15** were obtained with synthesized ~5 nm GNPs.

Gold Nanoparticles Conjugation

When preparing 1.1 ml of capped GNPs, 900 µl of 5 nm GNPs were added to 100 µl ligand mix. The ligand mix contained either 70 µl of 2 mM H-CVVVT-ol, obtained by mixing 35 µl of 4 mM H-CVVVT-ol in 75:25 DMSO:water (v/v) with 35 µl of water, and 30 µl of 2 mM PEG (i.e. HS-EC_{11}-EG_4), obtained by mixing 6 µl of 10 mM PEG in ethanol with 12 µl of ethanol and 12 µl of water, in the case of H-CVVVT-ol:PEG (70:30) "mix-matrix"[11] capped GNPs; or 2 mM PEG in 60:40

ethanol:water (v/v), in the case of PEG-capped GNPs; or 70 µl of 2 mM H-CVV(Bpa)T-ol peptide in DMSO and 30 µl of 2 mM PEG, obtained by mixing 6 µl of 10 mM PEG in ethanol with 12 µl of ethanol and 12 µl of water, in the case of H-CVV(Bpa)T-ol:PEG (70:30) capped GNPs. After the ligand mix was vortexed and the GNPs added, 100 µl of 0.05% Tween20 in 10X PBS v/v were added and the solution left overnight on a rotating wheel. The nanoparticles were then concentrated using a 10K Nanosep centrifugal filter by centrifugation at 10000 rpm for 10 min. The concentrated sample was purified from the excess of ligand by size exclusion chromatography using Sephedex G25 as stationary phase and 0.005% Tween20 in 1X PBS v/v as eluent. To be sure to remove the excess of ligand, the column volume has to be at least 10 times bigger than the sample volume.

As for the H-CVV(Bpa)T-ol:PEG (70:30) capped GNPs just in water, after the ligand mix was vortexed and the GNPs added, 100 µl of 10X PBS were added and the solution left overnight on a rotating wheel. The GNPs were then purified from the excess of ligand by 10K Nanosep centrifugal filter. The particles underwent at least 7 centrifugation cycles at 10000 rpm for 6 min. After each centrifugation cycle, 300 µl of water were added in order to re-suspend the concentrated sample. To be sure to remove all the ligand excess, UV-Vis spectra of the flow-through (FT), i.e. the liquid going through the filter, were taken at each centrifugation step. Bpa-containing peptide absorbs strongly in the spectral region 240-300 nm. Therefore, the purification progress was monitored by the decrease in absorbance between 240-300 nm, corresponding to the π-π^* benzophenone transition, and between 180-230 nm, associated with the peptide bond. **Fig. 2.18** shows the decrease and disappearance of absorbance at ~265 nm and ~205 nm after 7 centrifugations (see FT7). GNP solutions were kept in a glass vial.

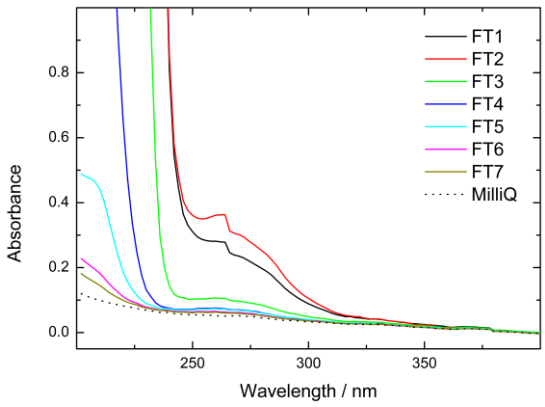

Fig. 2.18 – UV-Vis spectra of the liquid gone through the 10K Nanosep centrifugal filter used to purify H-CVV(Bpa)T-ol:PEG (70:30) capped GNPs from the excess of ligand. FT1-FT7 refer to the flow-through from the first to the seventh centrifugation, respectively.

The volume of H-CVV(Bpa)T-ol:PEG (70:30) capped 5 nm GNPs just in water prepared for taking the FTIR spectra of the nanoparticles in solution at different UV irradiation times was 55 ml; the ratio of ligands, GNPs and buffer for the conjugation were as those described above, as for the purification protocol. The solution was then freeze-dried and resuspended in 80 µl of DMSO after lyophilisation.

Is should be noted that the same protocols were adopted for both BBI and synthesized 5 nm GNPs.

Ligand Exchange Test (DTT Test)

The ligand exchange test was done as reported by Chen et al.[24] 1 M stock solution of dithiothreitol was freshly prepared in water and then diluted to give the following concentrations: 0.1, 1, 10, 100 mM. 57 µl of capped GNPs, 33 µl of 10X PBS and 10 µl of DTT at different concentrations (or water for the control experiment) were added to a 384 well plate. Each sample was done in duplicate.

UV-Vis spectra were taken after different incubation times, i.e. 20 min, 3h, 21h, 48h, at room temperature.

In order to compare the different samples' resistance to ligand exchange and therefore stability of the capping layer, an aggregation parameter (AP) was defined as A_{650nm}/A_{520nm} where A_{650nm} and A_{520nm} were the absorbance at 650 and 520 nm, respectively. The AP was calculated after baseline correction of UV-Vis spectra. To get the normalized aggregation parameter (NAP), the AP was divided by the AP of the control experiment, i.e. using neat water instead of DTT solution. Since each sample was done in duplicate, the mean of the two values with corresponding standard deviation are reported in **Fig. 2.12**.

References

(1) Dorman, G.; Prestwich, G. Benzophenone Photophores in Biochemistry. *Biochemistry* **1994**, *33*.

(2) Galardy, R. E.; Craig, L. C.; Jamieson, J. D.; Printz, M. P. Photoaffinity Labeling of Peptide Hormone Binding Sites. *J. Biol. Chem.* **1974**, *249*, 3510–3518.

(3) Kauer, J. C.; Erickson-viitanen, S.; Wolfe, H. R.; Degrado, W. F. P-Benzoyl-L-Phenylalanine, A New Photoreactive Amino Acid. *J. Biol. Chem.* **1986**, 10695–10700.

(4) Dorman, G.; Olszewski, J. Synthesis of Highly Tritiated 4-Benzoyl-L-Phenylalanine, a Photoactivatable Amino Acid. *J. Org. Chem.* **1995**, 2292–2297.

(5) Photochemistry https://www2.chemistry.msu.edu/faculty/reusch/virttxtjml/photchem.htm.

(6) MO description http://szerves.chem.elte.hu/oktatas/ea/Perczel/UV-VIS.pdf.

(7) Georg, H. C.; Coutinho, K.; Canuto, S. Solvent Effects on the UV-Visible Absorption Spectrum of Benzophenone in Water: A Combined Monte Carlo Quantum Mechanics Study Including Solute Polarization. *J. Chem. Phys.* **2007**, *126*, 34507.

(8) Dilling, W. The Effect of Solvent on the Electronic Transitions of Benzophenone and Its O-and P-Hydroxy Derivatives. *J. Org. Chem.* **1966**.

(9) Bennett, G.; Johnston, K. UV-Visible Absorbance Spectroscopy of Organic Probes in Supercritical Water. *J. Phys. Chem.* **1994**, 441–447.

(10) Prestwich, G. D.; Dorman, G.; Elliott, J. T.; Marecak, D. M.; Chaudhary, A. Benzophenone Photoprobes for Phosphoinositides , Peptides and Drugs. *Photochem. Photobiol.* **1997**, *65*, 222–234.

(11) Duchesne, L.; Gentili, D.; Comes-Franchini, M.; Fernig, D. G. Robust Ligand Shells for Biological Applications of Gold Nanoparticles. *Langmuir* **2008**, *24*, 13572–13580.

(12) Woodward, J. R.; Lin, T.; Sakaguchi, Y.; Hayashi, H. Biphotonic Photochemistry of Benzophenones in Dimethylsulphoxide: A Flash Photolysis EPR Study. *Mol. Phys.* **2002**, *100*, 1235–1244.

(13) Ilharco, L.; Garcia, A. Infrared Approach to the Study of Adsorption on Cellulose: Influence of Cellulose Crystallinity on the Adsorption of Benzophenone. *Langmuir* **1997**, *7463*, 4126–4132.

(14) Ilharco, L.; Garcia, A.; Silva, J. L. da. Ultraviolet-Visible and Fourier Transform Infrared Diffuse Reflectance Studies of Benzophenone and Fluorenone Adsorbed onto Microcrystalline Cellulose. *Langmuir* **1997**, *7463*, 3787–3793.

(15) Hong, K. H.; Liu, N.; Sun, G. UV-Induced Graft Polymerization of Acrylamide on Cellulose by Using Immobilized Benzophenone as a Photo-Initiator. *Eur. Polym. J.* **2009**, *45*, 2443–2449.

(16) Mathur, M.; Frenzel, C.; Bradley, E. Reinvestigation of the Raman Spectrum of Benzophenone Using a He-Ne Laser. *Spectrochim. Acta Part A* **1969**, *26*, 451–454.

(17) Coates, J. Interpretation of Infrared Spectra, A Practical Approach. In *Encyclopedia of Analytical Chemistry*; Meyers, R. A., Ed.; John Wiley & Sons, Ltd, 2006.

(18) Lévy, R.; Thanh, N. T. K.; Doty, R. C.; Hussain, I.; Nichols, R. J.; Schiffrin, D. J.; Brust, M.; Fernig, D. G. Rational and Combinatorial Design of Peptide Capping Ligands for Gold Nanoparticles. *J. Am. Chem. Soc.* **2004**, *126*, 10076–10084.

(19) Häkkinen, H. The Gold-Sulfur Interface at the Nanoscale. *Nat. Chem.* **2012**, *4*, 443–455.

(20) Love, J. C.; Estroff, L. A.; Kriebel, J. K.; Nuzzo, R. G.; Whitesides, G. M. Self-Assembled Monolayers of Thiolates on Metals as a Form of Nanotechnology. *Chem. Rev.* **2005**, *105*, 1103–1169.

(21) Demers, L. M.; Mirkin, C. A.; Mucic, R. C.; Reynolds, R. A.; Letsinger, R. L.; Elghanian, R.; Viswanadham, G. A Fluorescence-Based Method for Determining the Surface Coverage and Hybridization Efficiency of Thiol-Capped Oligonucleotides Bound to Gold Thin Films and Nanoparticles. *Anal. Chem.* **2000**, *72*, 5535–5541.

(22) Nicewarner Peña, S. R.; Raina, S.; Goodrich, G. P.; Fedoroff, N. V.; Keating, C. D. Hybridization and Enzymatic Extension of Au Nanoparticle-Bound Oligonucleotides. *J. Am. Chem. Soc.* **2002**, *124*, 7314–7323.

(23) Wilson, R.; Chen, Y.; Aveyard, J. One Molecule per Particle Method for Functionalising Nanoparticles. *Chem. Commun. (Camb).* **2004**, 1156–1157.

(24) Chen, X. Y.; Qoutah, W. W.; Free, P.; Hobley, J.; Fernig, D. G.; Paramelle, D. Features of Thiolated Ligands Promoting Resistance to Ligand Exchange in Self-Assembled Monolayers on Gold Nanoparticles. *Aust. J. Chem.* **2012**, *65*, 266–274.

(25) Yan, B.; Zhu, Z. J.; Miranda, O. R.; Chompoosor, A.; Rotello, V. M.; Vachet, R. W. Laser Desorption/ionization Mass Spectrometry Analysis of Monolayer-Protected Gold Nanoparticles. *Anal. Bioanal. Chem.* **2010**, *396*, 1025–1035.

(26) Zhu, Z. J.; Rotello, V. M.; Vachet, R. W. Engineered Nanoparticle Surfaces for Improved Mass Spectrometric Analyses. *Analyst* **2009**, *134*, 2183–2188.

(27) Chu, I.; Zhang, H.; Dearden, D. Macrocyclic Chemistry in the Gas Phase: Intrinsic Cation Affinities and Complexation Rates for Alkali Metal Cation Complexes of Crown Ethers and Glymes. *J. Am. Chem. Soc.* **1993**.

(28) Harbron, E. J. Photochromic Nanoparticles. **2011**, 211–227.

(29) Zhang, J.; Whitesell, J. K.; Fox, M. A. Photoreactivity of Self-Assembled Monolayers of Azobenzene or Stilbene Derivatives Capped on Colloidal Gold Clusters. *Chem. Mater.* **2001**, *13*, 2323–2331.

(30) Klajn, R.; Wesson, P. J.; Bishop, K. J. M.; Grzybowski, B. A. Writing Self-Erasing Images Using Metastable Nanoparticle "inks". *Angew. Chem. Int. Ed. Engl.* **2009**, *48*, 7035–7039.

(31) Ipe, B. I.; Mahima, S.; Thomas, K. G. Light-Induced Modulation of Self-Assembly on Spiropyran-Capped Gold Nanoparticles: A Potential System for the Controlled Release of Amino Acid Derivatives. *J. Am. Chem. Soc.* **2003**, *125*, 7174–7175.

(32) Fan, C.; Wang, S.; Hong, J. W.; Bazan, G. C.; Plaxco, K. W.; Heeger, A. J. Beyond Superquenching: Hyper-Efficient Energy Transfer from Conjugated Polymers to Gold Nanoparticles. *Proc. Natl. Acad. Sci. U. S. A.* **2003**, *100*, 6297–6301.

(33) Hu, M.; Hartland, G. V. Heat Dissipation for Au Particles in Aqueous Solution: Relaxation Time versus Size. *J. Phys. Chem. B* **2002**, *106*,

7029–7033.

(34) Haiss, W.; Thanh, N. T. K.; Aveyard, J.; Fernig, D. G. Determination of Size and Concentration of Gold Nanoparticles from UV-Vis Spectra. *Anal. Chem.* **2007**, *79*, 4215–4221.

CHAPTER 3

PROBING THE ACCESSIBILITY OF A FUNCTIONAL SITE WITHIN SELF-ASSEMBLED MONOLAYERS ON GOLD NANOPARTICLES WITH FLUORESCENTLY LABELLED PEPTIDES

3.1 Introduction

As highlighted in Chapter 1 and throughout this thesis, the elucidation of the structure and organization of self-assembled monolayers (SAMs) on gold nanoparticles (GNPs) is important to help toward the design of nanomaterials with well-defined bio-physicochemical properties. Also, for applications such as sensing, understanding and tuning the interactions of these bio-nanoconjugates with biomolecules is crucial.[1]

Here, gold nanoparticles were functionalized with a mixed self-assembled monolayer constituted of a functional peptide, bearing both an enzyme cleavage site and a fluorophore, and a main matrix peptide.

The high fluorescence quenching efficiency by GNPs, as well as the possibility to impart specific recognition properties to the monolayer, were exploited to detect the enzyme accessing the cleavage site within the different self-assembled monolayers investigated. Previous works by Hong et al.,[2] Lee et al.[3] and Free et al.[4] developed enzyme-sensitive gold nanoparticles detecting the enzymatic activity by fluorescence unquenching.

Thus, the fluorescence measurements, probing the accessibility of a functional site within SAMs, aim to help understanding the interactions between biomolecules and bio-nanoconjugates, as well as to indirectly probe the molecular environment of the functional peptide.

This chapter builds from the work of undergrad students and reports the effect of the monolayer composition, and some preliminary results on the effect of the monolayer capping density, on the accessibility of a thrombin cleavage site at different positions from the GNP surface.

3.1.1 Fluorescently Labelled Peptides

To probe the accessibility from an enzyme of a functional site at the surface of gold nanoparticles, four fluorescently labelled peptides were designed to be inserted into peptide self-assembled monolayers on GNPs.

The fluorescently labelled peptide sequences, listed in **Table 3.1**, can be divided into three segments, from left to right, according to the position of thrombin cleavage site LVPRGS (highlighted in red). The sequence of the segment prior to the cleavage site is based on CALNN peptide[5] and is progressively elongated of two amino acids. Also, cysteine is always the N-terminal residue because the thiol group is necessary to anchor the peptide to the gold surface.[6] As for the cleavage site LVPRGS, thrombin cleaves between arginine (R) and glycine (G) residues and thus, the four fluorescently labelled peptides are referred as P7, P9, P11 and P13, accordingly to the position of the arginine residue from the terminal cysteine. The last part of the sequence is constituted of a short linker and fluorescein-labelled lysine.

Table 3.1 – Amino acid sequence and notation employed for the fluorescently labelled peptides. Thrombin cleavage site is highlighted in red; K(*Flu*) denotes the fluorescein-labelled lysine.

Residue Sequence	Notation
CAALVPRGSGTAK(*Flu*)-NH_2	P7
CALNALVPRGSGTAK(*Flu*)-NH_2	P9
CALNNGALVPRGSGTAK(*Flu*)-NH_2	P11
CALNNGGGALVPRGSGTAK(*Flu*)-NH_2	P13

3.2 Experimental Outline

The experimental work was developed as follows. GNPs were capped with a self-assembled monolayer (SAM) constituted of CALNN penta-, or CCALNN hexa-, or CALNNGG hepta-peptide and the functional peptide P7, or P9, or P11, or P13 (**Table 3.1**), which can be cleaved by thrombin and is fluorescently labelled.

When the fluorescently-labelled peptides were intact and anchored to the gold surface, the fluorescence was quenched as a result of fluorescence resonance energy transfer (FRET) to the GNP.[7] Indeed, after purification from the excess of ligands, almost no fluorescence signal was emitted by the

fluorescently labelled peptides anchored to the GNPs (see **Fig. 3.6** in **Methods** section). Upon incubation in dithiothreitol (DTT), which displaces the initial ligands and leads to ligand exchange,[8–10] the fluorescently labelled ligands anchored to the gold surface were released and thus, the total amount of fluorescence present was unquenched and measured (see **Fig. 3.7** in **Methods** section).

Upon incubation and cleavage by thrombin, the fluorescently labelled peptide segments were released from the nanoparticles surface; hence, the corresponding increase in fluorescence was measured. Thus, the percentages of total fluorescence released over time (see **Methods** section for details on the calculations), upon incubation in different concentrations of thrombin, probed the accessibility of the cleavage site, within the different self-assembled monolayers investigated, from thrombin.

Furthermore, the effect of the SAM capping density on the accessibility of thrombin cleavage site was preliminarily investigated.

3.3 Experimental Results on the Accessibility of Thrombin Cleavage Site

3.3.1 Effect of the Monolayer Composition

To assess the effect of the monolayer composition on the accessibility of a functional site within self-assembled monolayers, GNPs were capped with a mixed SAM constituted of CALNN penta-, or CCALNN hexa-, or CALNNGG hepta-peptide and the functional peptide P7, or P9, or P11, or P13 (**Table 3.1**).

As mentioned in **Section 3.2** and detailed in the **Methods** section, upon purification from the excess of ligands, the total amount of fluorescence present was assessed by ligand exchange and thus, the percentages of total fluorescence released, upon incubation in different concentrations of thrombin, calculated.

Considering the GNPs capped with combinations of CALNN and fluorescently labelled peptides, **Fig. 3.1A** shows almost complete release of fluorescence at the lowest concentration of thrombin used, i.e. 0.5 U/ml, for CALNN:P13 self-assembled monolayer. Thus, P13's cleavage site appears to be easily accessed by thrombin in a CALNN monolayer.

It is worth noting how CALNN:P13 and CALNN:P11 monolayers were differently accessed by thrombin. For instance, whilst nearly all P13 ligands were cleaved with 0.5 U/ml thrombin after ~50 min of incubation, P11 ligands were still almost intact upon incubation in 0.5 U/ml thrombin over 250 min. Thus, the

results indicate that thrombin accessibility hence, cleavage, is extremely sensitive to the exact position of the cleavage site and that a difference of two residues produces a large effect. Also, **Fig. 3.1B** illustrates that thrombin kinetics for P11 is sensitive to the enzyme concentration.

No release in fluorescence was detected for the monolayers bearing thrombin cleavage site closer to the gold surface, i.e., CALNN:P7 and CALNN:P9. It is worth remarking that the addition of DTT to the solutions incubated for 250 min in 0.5 U/ml thrombin released the fluorescence associated to P7 and P9 ligands, thus confirming the peptides' functionality (**Fig. 3.1A**).

Therefore, whilst the inaccessibility of CALNN:P7 monolayer confirms the high packing of the inner part of CALNN monolayer, which is stabilized through hydrophobic interactions,[5] the fact that P9 cleavage was not observed suggests a monolayer conformation where the segments of fluorescently labelled peptides exceeding CALNN's length are back-folded onto the CALNN monolayer. The poor cleavage observed for P11 ligand, as well as its dependence on the enzyme concentration, further point to the conformation suggested above, which would prevent/hinder the enzyme from accessing the cleavage site. However, considering the ease of cleavage of P13 ligand, the boundary between a back-folded and extended conformation appears to be well-defined.

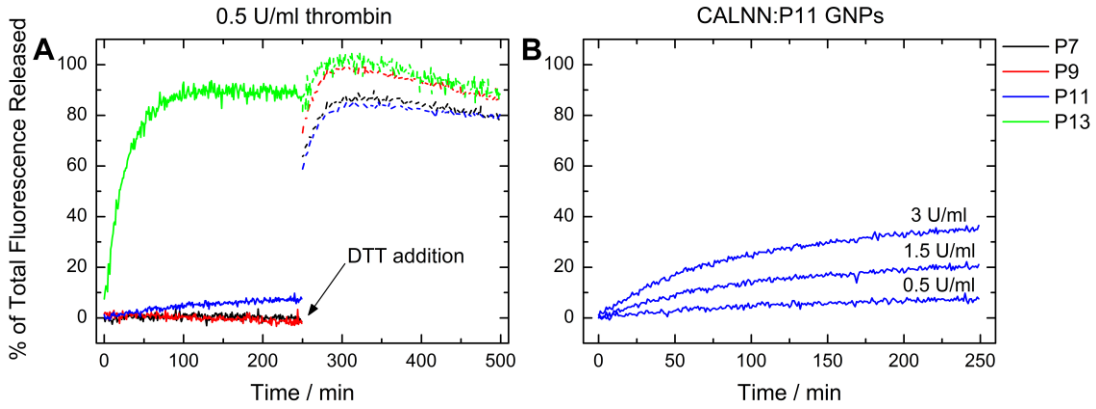

Fig. 3.1 – Percentage of total fluorescence released from GNPs capped by (**A**) CALNN and a fluorescently labelled peptide (P7-P13) in 98:2 ratio upon incubation in 0.5 U/ml thrombin and further addition of DTT; (**B**) CALNN and P11 in 98:2 ratio upon incubation in three different thrombin concentrations. The GNPs were conjugated with 1 mM ligand mix. The curves are the result of averaging over three measurements using the same batch of nanoparticles.

As for the self-assembled monolayers constituted of matrix peptides one-, i.e. CCALNN, or two-, i.e. CALNNGG, residues longer than CALNN, **Fig. 3.2** shows that only P13's outer site was accessed and cleaved by thrombin, and that

P13 was the only fluorescent peptide sensitive to different concentrations of thrombin.

Moreover, contrarily to CALNN:P13 monolayer, the increase in fluorescence was found to be more gradual and to reach a plateau over the 250 min in which was monitored, thus indicating higher molecular crowding and steric hindrance within these SAMs, as expected on the basis of the CALNN results shown and discussed above. Similarly, Free et al. investigated the effect that increasing amounts of PEGylated ligands within self-assembled monolayers on GNPs had on the cleavage of fluorescently labelled peptides from proteases. The authors found the enzymatic kinetics decreasing upon increase of the content of PEGylated ligands, thus highlighting the effect of molecular crowding on enzymatic activity.[4]

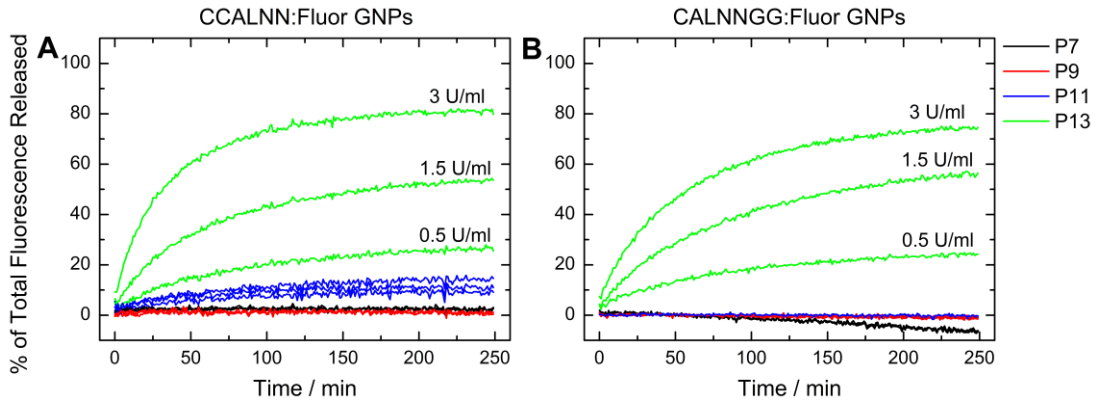

Fig. 3.2 – Percentage of total fluorescence released from GNPs capped by (**A**) CCALNN or (**B**) CALNNGG and a fluorescently labelled peptide (P7-P13) in 98:2 ratio upon incubation in three different thrombin concentrations. The GNPs were conjugated with 1 mM ligand mix. The curves are the result of averaging over three measurements using the same batch of nanoparticles.

Surprisingly, in all the monolayers investigated, the percentage of total fluorescence released converged to different amounts when incubated with different concentrations of thrombin. This observation is unexpected for an enzymatic reaction and might be ascribed to a loss of thrombin's cleavage ability, perhaps due to thrombin inhibition by the aromatic fluorescein compound.[11]

3.3.2 Effect of the Monolayer Capping Density

To preliminarily assess the effect of the monolayer capping density on the accessibility of thrombin cleavage site, GNPs were prepared with a 0.1 mM mixture of CALNN peptide and functional peptide P7, or P9, or P11, or P13, instead of 1 mM, used for the experiments described in the previous section (see **Methods** section for details on the conjugation).

Whilst in **Fig. 3.1A** an almost complete release of total fluorescence was observed for CALNN:P13 capped GNPs prepared with 1 mM ligand mix and incubated in 0.5 U/ml thrombin, the total fluorescence released from CALNN:P13 monolayer on GNPs prepared with 0.1 mM ligand mix and incubated in 0.5 U/ml thrombin was not found to increase overtime (**Fig. 3.3A**). However, **Fig. 3.3B** indicates that a small fraction of P13 ligands was rapidly cleaved upon thrombin addition and that the amount of fluorescence released from CALNN:P13 monolayer was affected, with some extent, by the concentration of thrombin used in the incubation.

A possible explanation for the small release observed for the low capping density CALNN:P13 monolayer might be traced into the lying-down of the fluorescently labelled ligand onto the gold surface, thus making the cleavage site less accessible. Previous FTIR investigations,[12,13] as well as part of Chapter 4 reported in this body of work, have indeed demonstrated that the peptide capping density does have an effect on the monolayer conformation. Moreover, Todorova et al., when investigating by all-atom molecular dynamics simulations the effect of TAT concentration, i.e., a cell-penetrating peptide, on the structure and compactness of a CALNN monolayer on GNPs, pointed out that the exposure towards the solvent of specific TAT residues was highly dependent on its concentration within the monolayer.[14]

No release in fluorescence was detected for CALNN:P7-P11 monolayers, but the further addition of DTT to the solutions incubated for 250 min in 0.5 U/ml thrombin did confirm the peptides' functionality (**Fig. 3.3A**).

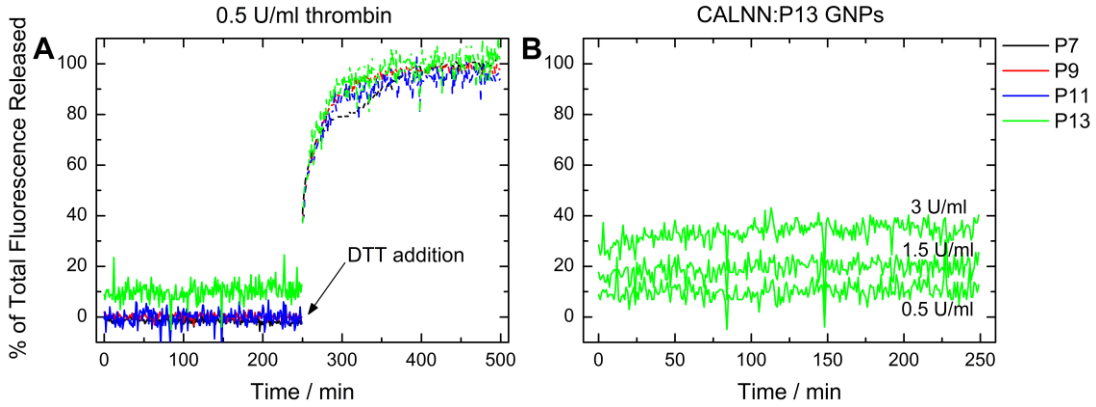

Fig. 3.3 – Percentage of total fluorescence released from GNPs capped by (**A**) CALNN and a fluorescently labelled peptide (P7-P13) in 98:2 ratio upon incubation in 0.5 U/ml thrombin and further addition of DTT; (**B**) CALNN and P13 in 98:2 ratio upon incubation in three different thrombin concentrations. The GNPs were conjugated with 0.1 mM ligand mix. The curves are the result of averaging over three measurements using the same batch of nanoparticles.

3.4 Conclusions

In this chapter, by exploiting the sensitivity of fluorescence quenching by gold nanoparticles, we have demonstrated that the possibility for an enzyme to access a functional site (here, cleavage site) is extraordinary sensitive to the precise position and surrounding environment.

For instance, we have highlighted that a difference of two residues in the position of the cleavage site, as well as in the length of the matrix peptide used, is quite relevant for the enzyme-substrate interactions.

Moreover, through comparison of the percentages of total fluorescence released, the molecular environment around the fluorescent peptides was probed, thus providing indirect information about the monolayer's structure. For instance, P13 cleavage was found to be affected by the length of the matrix peptide used hence, by the molecular crowdedness within the self-assembled monolayer. Furthermore, also the monolayer capping density was found to influence P13 cleavage.

Therefore, to fully exploit the possibility to control the interactions of nanomaterials with biomolecules and tune their properties, we suggest that these findings should be taken into account in the design of bio-nanoconjugates.

3.5 Materials and Methods

3.5.1 Materials

All peptides (CALNN, CCALNN, CALNNGG) and fluorescently labelled peptides (CAALVPRGSGTAK(*Flu*)-NH_2, CALNALVPRGSGTAK(*Flu*)-NH_2, CALNNGALVPRGSGTAK(*Flu*)-NH_2, CALNNGGGALVPRGSGTAK(*Flu*)-NH_2, referred to as P7, P9, P11, P13, respectively) with >70% purity were purchased from Peptide Protein Research Ltd. Bovine thrombin enzyme was purchased from Merck Millipore. All the chemicals were purchased from Sigma Aldrich.

1 liter of phosphate buffered saline (PBS) stock solution (10X) was prepared by adding 80 g NaCl, 2 g KCl, 11.5 g Na_2HPO_4 and 2 g KH_2PO_4 to water.

All aqueous solutions were prepared using ultrapure water from a MilliQ system (Millipore Synergy system).

3.5.2 Instruments

UV-Vis spectra were recorded on a SpectraMax Plus 384 microplate spectrophotometer using a quartz SUPRASIL cuvette (path length of 1 cm) purchased from Hellma or a 384-well plate.

Fluorescence spectra were recorded on a BMG Labtech POLARstar OPTIMA fluorometer with an excitation and emission wavelength of 485 and 520 nm, respectively, and a gain of 1000. All measurements were done at room temperature using a black 96-well plate from Greiner Bio-One. The fluorescence measurements over time were taken every 60 sec over 250 min.

Transmission Electron Microscopy analysis was performed using a Tecnai G2 Spirit BioTWIN at 120 kV. 200 mesh hexagonal copper grids were coated by pioloform (polyvinyl butyral). 5 µl of sample were spotted on the grid and left drying at room temperature.

The images were analyzed with ImageJ software.

3.5.3 Methods

Gold Nanoparticles Synthesis and Characterization

Before the synthesis of gold nanoparticles, all the glassware and magnetic stirrer bar were cleaned with aqua regia, ethanol, and water and dried in an oven.

~10 nm gold nanoparticles were synthesized as described by Bastús et al.[15] 150 ml of a solution of 2.2 mM sodium citrate were heated and stirred under

reflux in a three-necked round-bottomed flask. Once the solution started boiling, 6 min were waited before injecting 1 ml of 25 mM $HAuCl_4$ on one side of the flask. The color of the solution changed from pale yellow to red and then black, before turning to pink and finally to rubine red.

The GNPs UV-Vis spectrum is shown in **Fig. 3.4, left** and from the analysis of three TEM images, as the one reported in **Fig. 3.4, right**, an average size of 10.2 ± 1.6 nm was determined. A concentration of 6.4 nM was calculated using Haiss et al. method.[16]

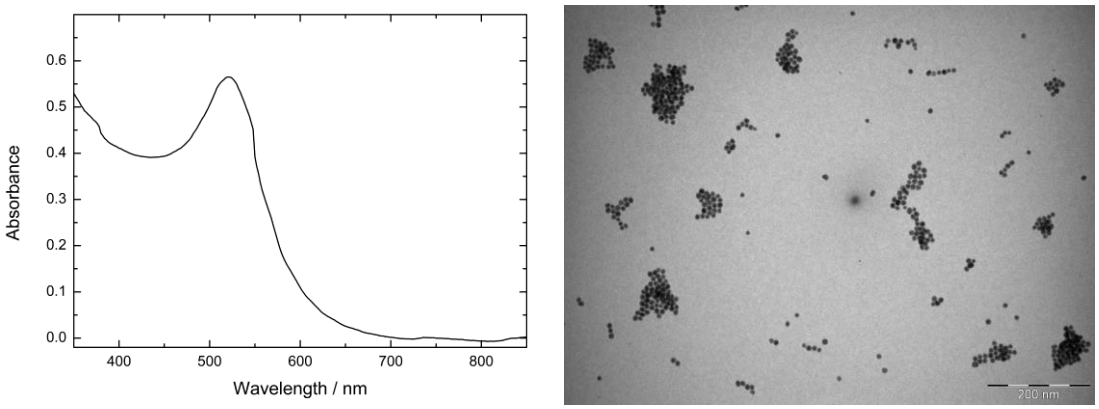

Fig. 3.4 – UV-Vis spectrum (**left**) and transmission electron microscopy image (**right**) of the synthesized 6.4 nM ~10 nm GNPs.

Gold Nanoparticles Conjugation and Purification

When preparing 1.1 ml of capped GNPs, 900 µl of ~10 nm GNPs were added to 100 µl of ligand mix. The ligand mix contained 98 µl of 1 (or 0.1) mM CALNN or CCALNN or CALNNGG prepared in 10X PBS, and 2 µl of 1 (or 0.1) mM fluorescently labelled peptide in DMSO (i.e., P7 or P9 or P11 or P13). After vortex-mixing the ligands and adding the GNPs, 100 µl of 10X PBS were added and the solution was left overnight on a rotating wheel in the dark, to prevent the photo-bleaching of the fluorescent peptides. The GNPs were then purified from the excess of ligands by centrifugation with 30K Nanosep centrifugal filters. The particles underwent at least 6 centrifugation cycles at 10000 rpm for 7 min. After each centrifugation cycle, 500 µl of 0.01% Tween20 in 1X PBS v/v were added in order to re-suspend the concentrated sample. To make sure to remove all the ligands excess, fluorescence measurements at 520 nm (excitation at 485 nm) of the flow-through, i.e. the liquid going through the filter, were taken at each centrifugation step. The fluorescent peptides, containing fluorescein-labelled lysine whose maximum absorption and emission is at 494 and 512 nm,

respectively, allowed monitoring the progress of the purification through the decrease in fluorescence at 520 nm (**Fig. 3.5**).

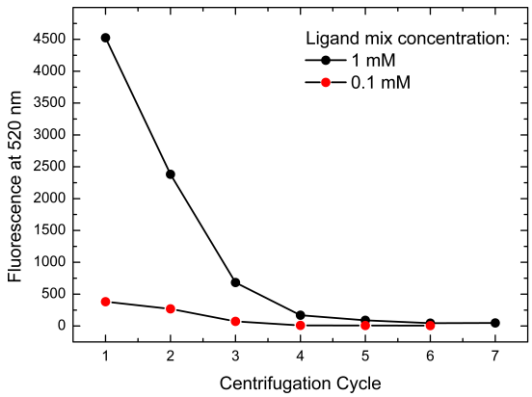

Fig. 3.5 – Fluorescence measurements at 520 nm (excitation at 485 nm) of the liquid gone through the 30K Nanosep centrifugal filter at each purification step for CALNN:P7 (98:2) capped GNPs, conjugated in the presence of 1 (black curve) or 0.1 (red curve) mM ligand mix.

The final pellet was re-suspended in 1X PBS and 0.01% Tween20 v/v to have a nominal value of absorbance at the plasmon band of ~0.3.

Analysis of Fluorescence and Thrombin Activity Measurements

The fluorescence signal from 90 µl of capped GNPs added to 10 µl of 1X PBS was measured as a control. Indeed, **Fig. 3.6** shows that, after removal of the excess of ligands, the fluorescence signal of the fluorescently labelled peptides anchored to the gold surface is quenched as a result of fluorescence resonance energy transfer (FRET) to the gold cores.[7] All the measurements were subtracted for the corresponding control experiment in 1X PBS, representing the baseline correction.

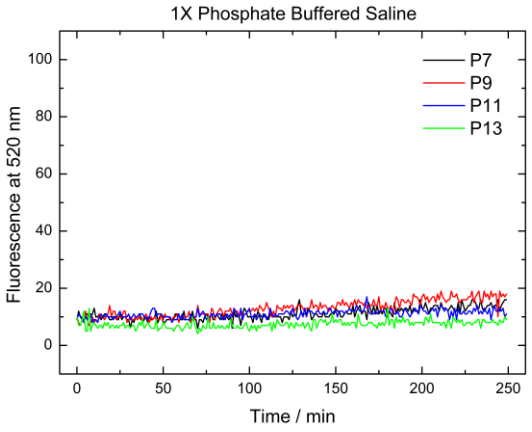

Fig. 3.6 – Fluorescence signal at 520 nm (excitation at 485 nm) over 250 min of GNPs capped by CALNN and a fluorescently labelled peptide (P7-P13) in 98:2 ratio in the presence of 1X PBS; the GNPs were conjugated with 1 mM ligand mix.

The total amount of fluorescence present on the GNPs was measured by adding 90 µl of capped GNPs to 10 µl of 1 M dithiothreitol (DTT) freshly prepared in water. **Fig. 3.7** is an example of the increase in fluorescence measured upon incubation in 1 M DTT, which leads to ligand exchange, hence release of the fluorescently labelled peptides.

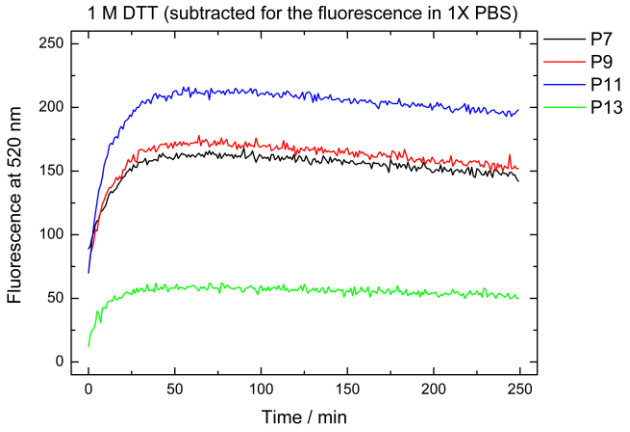

Fig. 3.7 – Fluorescence signal at 520 nm (excitation at 485 nm) over 250 min of GNPs capped by CALNN and a fluorescently labelled peptide (P7-P13) in 98:2 ratio upon incubation in 1 M DTT; the GNPs were conjugated with 1 mM ligand mix and the spectra reported are subtracted for the corresponding control experiment in 1X PBS.

The thrombin activity was measured by adding 90 µl of capped GNPs to 10 µl of thrombin in the following concentrations in water: 0.5, 1.5, 3 U/ml. Complete release of the fluorescent peptide from the capped GNPs was checked by further addition of 10 µl of 1 M DTT after 250 min of incubation in 0.5 U/ml thrombin. Each sample was done in triplicate using the same batch of nanoparticles.

In the chapter, the percentages of total fluorescence released from the GNPs, upon incubation in thrombin or further addition of DTT, were calculated by first correcting the measurements for the corresponding control experiment in 1X PBS and then by normalizing the obtained values for the total amount of fluorescence present on the GNPs, which was calculated by averaging the region of constant fluorescence upon DTT release, e.g., from 50 to 100 min in the case of the example reported in **Fig. 3.7**.

References

(1) Saha, K.; Agasti, S.; Kim, C.; Li, X.; Rotello, V. Gold Nanoparticles in Chemical and Biological Sensing. *Chem. Rev.* **2012**, *112*, 2739–2779.

(2) Hong, R.; Emrick, T.; Rotello, V. M. Monolayer-Controlled Substrate Selectivity Using Noncovalent Enzyme-Nanoparticle Conjugates. *J. Am. Chem. Soc.* **2004**, *126*, 13572–13573.

(3) Lee, S.; Cha, E.-J.; Park, K.; Lee, S.-Y.; Hong, J.-K.; Sun, I.-C.; Kim, S. Y.; Choi, K.; Kwon, I. C.; Kim, K.; *et al.* A Near-Infrared-Fluorescence-Quenched Gold-Nanoparticle Imaging Probe for In Vivo Drug Screening and Protease Activity Determination. *Angew. Chemie* **2008**, *120*, 2846–2849.

(4) Free, P.; Shaw, C. P.; Lévy, R. PEGylation Modulates the Interfacial Kinetics of Proteases on Peptide-Capped Gold Nanoparticles. *Chem. Commun.* **2009**, 5009–5011.

(5) Lévy, R.; Thanh, N. T. K.; Doty, R. C.; Hussain, I.; Nichols, R. J.; Schiffrin, D. J.; Brust, M.; Fernig, D. G. Rational and Combinatorial Design of Peptide Capping Ligands for Gold Nanoparticles. *J. Am. Chem. Soc.* **2004**, *126*, 10076–10084.

(6) Häkkinen, H. The Gold-Sulfur Interface at the Nanoscale. *Nat. Chem.* **2012**, *4*, 443–455.

(7) Sapsford, K. E.; Berti, L.; Medintz, I. L. Materials for Fluorescence Resonance Energy Transfer Analysis: Beyond Traditional Donor–Acceptor Combinations. *Angew. Chemie Int. Ed.* **2006**, *45*, 4562–4589.

(8) Love, J. C.; Estroff, L. A.; Kriebel, J. K.; Nuzzo, R. G.; Whitesides, G. M. Self-Assembled Monolayers of Thiolates on Metals as a Form of Nanotechnology. *Chem. Rev.* **2005**, *105*, 1103–1169.

(9) Chen, X. Y.; Qoutah, W. W.; Free, P.; Hobley, J.; Fernig, D. G.; Paramelle, D. Features of Thiolated Ligands Promoting Resistance to Ligand Exchange in Self-Assembled Monolayers on Gold Nanoparticles. *Aust. J. Chem.* **2012**, *65*, 266–274.

(10) Demers, L. M.; Mirkin, C. A.; Mucic, R. C.; Reynolds, R. A.; Letsinger, R. L.; Elghanian, R.; Viswanadham, G. A Fluorescence-Based Method for Determining the Surface Coverage and Hybridization Efficiency of Thiol-Capped Oligonucleotides Bound to Gold Thin Films and Nanoparticles. *Anal. Chem.* **2000**, *72*, 5535–5541.

(11) Lu, T.; Tomczuk, B.; Bone, R.; Murphy, L.; Salemme, F. R.; Soll, R. M. Non-Peptidic Phenyl-Based Thrombin Inhibitors: Exploring Structural Requirements of the S1 Specificity Pocket with Amidines. *Bioorg. Med. Chem. Lett.* **2000**, *10*, 83–85.

(12) Shaw, C. P.; Middleton, D. A.; Volk, M.; Lévy, R. Amyloid-Derived Peptide Forms Self-Assembled Monolayers on Gold Nanoparticle with a Curvature-Dependent β-Sheet Structure. *ACS Nano* **2012**, *6*, 1416–1426.

(13) Krpetić, Z.; Davidson, A. M.; Volk, M.; Lévy, R.; Brust, M.; Cooper, D. L. High-Resolution Sizing of Monolayer-Protected Gold Clusters by Differential Centrifugal Sedimentation. *ACS Nano* **2013**, *7*, 8881–8890.

(14) Todorova, N.; Chiappini, C.; Mager, M.; Simona, B.; Patel, I. I.; Stevens, M. M.; Yarovsky, I. Surface Presentation of Functional Peptides in Solution Determines Cell Internalization Efficiency of TAT Conjugated Nanoparticles. *Nano Lett.* **2014**, *14*, 5229–5237.

(15) Bastús, N. G.; Comenge, J.; Puntes, V. Kinetically Controlled Seeded

Growth Synthesis of Citrate-Stabilized Gold Nanoparticles of up to 200 Nm: Size Focusing versus Ostwald Ripening. *Langmuir* **2011**, *27*, 11098–11105.

(16) Haiss, W.; Thanh, N. T. K.; Aveyard, J.; Fernig, D. G. Determination of Size and Concentration of Gold Nanoparticles from UV-Vis Spectra. *Anal. Chem.* **2007**, *79*, 4215–4221.

CHAPTER 4

MANUSCRIPT: EXPERIMENTAL AND COMPUTATIONAL INVESTIGATION OF THE STRUCTURE OF PEPTIDE MONOLAYERS ON GOLD NANOPARTICLES

4.1 Preface

Chapter 4 is constituted of the manuscript and associated Supporting Information, entitled "Experimental and Computational Investigation of the Structure of Peptide Monolayers on Gold Nanoparticles", submitted to the *Journal of the American Chemical Society*.

This work has been conducted nearly entirely during the 2 years of my PhD spent at the A*STAR Institute of Materials Research and Engineering (IMRE) and at the A*STAR Institute of High Performance Computing (IHPC) in Singapore. The design of the study was done in collaboration with Dr Michael Sullivan and Dr CHEN Qiubo, who wrote the scripts to create the initial structures, as well as some (Dr Martin Volk wrote others) of the custom-written software used to analyze the data.

As already stated, to envision the assembly of peptide-capped gold nanoparticles into protein-like structures, the monolayer structural characterization is of fundamental importance. Thus, considering the challenges and limitations associated to the experimental characterization of the molecular structure of three dimensional peptide self-assembled monolayers on GNPs, in this Chapter a molecular dynamics computational model that can predict the secondary structure of peptide self-assembled monolayers on gold nanoparticles is presented. The model, validated on the basis of experimental findings, provided detailed insights into the peptides' structural and dynamic properties.

Moreover, it is worth noting that, hoping to contribute to the further development of this field and considering the reproducibility crisis in science, we are making available in an on-line repository of the University of Liverpool the computational data and the custom-written software from this work (now only accessible by the referees, but fully open from the date of publication).

4.2 Experimental and Computational Investigation of the Structure of Peptide Monolayers on Gold Nanoparticles

Elena Colangelo,[a,b,c,‡] Qiubo Chen,[c,‡] Adam M. Davidson,[d] David Paramelle,[b] Michael B. Sullivan,[c] Martin Volk,[d,e,*] Raphaël Lévy[a,*]

[a]Institute of Integrative Biology, University of Liverpool, Crown Street, L69 7ZB Liverpool, United Kingdom

[b]Institute of Materials Research and Engineering, A*STAR (Agency for Science, Technology and Research), 2 Fusionopolis Way, #08-03 Innovis, Singapore 138634

[c]Institute of High Performance Computing, A*STAR (Agency for Science, Technology and Research), 1 Fusionopolis Way, #16-16 Connexis North, Singapore 138632

[d]Department of Chemistry, University of Liverpool, Liverpool L69 7ZD, United Kingdom

[e]Surface Science Research Centre, Department of Chemistry, Abercromby Square, University of Liverpool, Liverpool L69 3BX, United Kingdom

ABSTRACT: The self-assembly and self-organization of small molecules at the surface of nanoparticles constitute a potential route towards the preparation of advanced protein-like nanosystems. However, their structural characterization, critical to the design of bio-nanomaterials with well-defined biophysical and biochemical properties, remains highly challenging. Here, a computational model for peptide-capped gold nanoparticles is developed using experimentally characterized CALNN- and CFGAILSS-capped gold nanoparticles as a benchmark. The structure of CALNN and CFGAILSS monolayers is investigated by both structural biology techniques and molecular dynamics simulations. The calculations reproduce the experimentally observed dependence of the monolayer secondary structure on peptide capping density and on nanoparticle size, thus giving us confidence in the model. Furthermore, the computational results reveal a number of new features of peptide-capped monolayers, including the importance of sulfur movement for the formation of secondary structure motifs, the presence of water close to the gold surface even in tightly packed peptide monolayers, and the existence of extended 2D parallel β-sheet domains in CFGAILSS monolayers. The model developed here provides a predictive tool that may assist in the design of further bio-nanomaterials.

Introduction

The electronic and optical properties[1] of gold nanoparticles (GNPs), together with the possibility of tuning their colloidal and (bio)chemical properties by functionalization with small ligands, such as alkyl thiols and peptides, has led extensive research over the last 20 years, targeted towards potential applications in bio-imaging and biomedicine,[2] sensing and catalysis.[3] These ligands, through gold-thiol chemistry,[4] bind to the GNP surface and form compact self-assembled

monolayers (SAMs).[5] Breakthroughs were made in the early '90s by studies reporting straightforward synthesis methods[6–8] to prepare GNPs of desired size, stabilized by alkyl thiols. Ten years later, we introduced peptide self-assembled monolayers on GNPs, starting from the design of CALNN, a pentapeptide developed from general protein folding principles.[9] We have described peptide-capped GNPs as building-blocks which could potentially be assembled in complex networks and engineered into protein-like objects using a "bottom-up" approach.[10] Controlling and characterizing the structure of peptide SAMs with molecular details is a fundamental prerequisite to envision building such artificial nanosystems. Attempts at determining the monolayer structure of such systems include the study of Fabris et al., where peptides based on α-aminoisobutyric acid units were found to form 3_{10}-helical secondary structure motifs both in solution and at the surface of 1-2 nm GNPs by IR and NMR spectroscopies which also indicated the presence of both intra- and inter-peptide hydrogen bonds.[11] Rio-Echevarria et al. used circular dichroism to confirm that the helical secondary structure of an undecapeptide was maintained both in solution and at the surface of 1-2 nm GNPs.[12]

While elucidating the structure of peptide monolayers with experimental techniques remains challenging, combining experimental and computational approaches can shed light on the structures with molecular details. Alkyl thiol-capped GNPs have been investigated more extensively than peptide-capped GNPs and different classical force fields (FF) have been reported in the literature describing the interactions of alkyl thiols on gold.[13–16] The first FF specifically designed for biomolecules on Au(111) surface dates only from 2008.[17] For such systems, not only the secondary interactions between the amino acids and the gold surface, but also the gold polarization induced by the biomolecule and surrounding water molecules should be taken into account for a compelling description.[18] The first study using atomistic molecular dynamics (MD) simulations to investigate the structure of alkane thiols on gold nanoparticles as a function of temperature, GNP size and length of the ligand dates from 2007;[19] investigations of the structure and properties of GNPs capped with a monolayer constituted of two alkane thiols differently organized also followed.[20–22] However, no MD simulations have been conducted yet to assess the structure of SAMs of peptides on spherical gold nanoparticles while taking into account both the self-organization of peptides and the gold atoms' polarizability. Examples of simpler descriptions that did not consider such aspects are Duchesne et al.'s work, where MD simulations were used to

determine the volume probed by a functional peptide embedded in a mixed SAM peptide monolayer constituting a surface with a curvature appropriate for a 10 nm GNP[23] and Todorova et al.'s investigation of the effect of TAT concentration, i.e., a cell-penetrating peptide, on the structure and compactness of a CALNN monolayer anchored to 3 nm GNPs built from neutral carbon-type atoms.[24] Also, Lee et al. looked at the effect that conjugating a single peptide to a GNP had on its structure.[25]

Here, a computational model for peptide-capped gold nanoparticles is presented for which the GolP-CHARMM[26] force field, parameterized for both Au(100) and Au(111) surfaces and accounting for the dynamic polarization of gold atoms produced by the interactions with the biomolecules and the surrounding environment, was adopted.

In particular, the model is developed using experimentally characterized CALNN-[9] and CFGAILSS-[27] capped GNPs as a benchmark and simulations are carried out by means of molecular dynamics. The model's results for the secondary structure of the monolayers in the simulated systems are compared to those of two independent experimental studies, the first reported here, and the second previously published.[27] In the first, the effect of capping density on the secondary structure of the CALNN monolayer on GNPs was investigated by Fourier transform infrared (FTIR) spectroscopy. In the second study, the effect of the nanoparticle curvature on the secondary structure and intermolecular interactions of CALNN and CFGAILSS peptide monolayers on GNPs of different sizes was determined by a combination of FTIR and solid-state NMR spectroscopies.[27] Following validation of the computational model against these experimental studies, detailed insights into the peptides' structural and dynamic properties are obtained, including the importance of sulfur movement for the formation of secondary structures, the presence of water close to the gold surface even in tightly packed peptide monolayers, and the existence of extended 2D parallel β-sheet domains in CFGAILSS monolayers.

Computational Model

Molecular dynamics simulations were performed using GROMACS package,[28–31] version 4.6.5. A combination of the GolP-CHARMM[26] force field and its predecessor GolP[17] was adopted to describe the peptides, the gold atoms and the peptide-

surface interactions. For the latter, the GolP-CHARMM Lennard Jones parameters for the Au(100) surface were used.

The initial structures for the simulations were prepared as follows: the nanoparticle was modelled as a sphere of the desired size, where the constituting gold atoms, within the GolP-CHARMM force field description, are represented by a real gold atom and a virtual site, called AU and AUC, respectively, where AU is fixed whereas AUC can move (for more details see Supporting Information, section S1.1). AU and AUC are constrained at a distance of 0.07 nm and the mass of each is equal to half the mass of a single gold atom, i.e., 196.97/2 amu. AU and AUC are partially charged, i.e., -0.3 and +0.3, respectively, and thus account for the dynamic polarization of the gold surface. We note that in the original GolP force field, AUC had a mass of 0.5 amu whereas AU of 196.967 amu.[17] Even though the original description of the gold atom was more realistic, we argue that the gold atom representation employed in this work still accounts for the dynamic polarization of the gold surface, and, more importantly, does not affect the peptide-surface interactions, mainly determined by electrostatic interactions. Indeed, the interactions between the peptide atoms and AUC are described only in terms of Coulombic electrostatic interactions, whereas those with AU include both Coulombic and van der Waals interactions; the latter are described by 12-6 Lennard-Jones (LJ) potentials.

The starting coordinates of CALNN (Cys-Ala-Leu-Asn-Asn) and CFGAILSS (Cys-Phe-Gly-Ala-Ile-Leu-Ser-Ser) peptides were created using the Materials Studio program. A linear geometry for the peptide backbone was chosen. The peptides, in zwitterionic form, were oriented with the N-terminus toward the gold nanoparticle surface and the C-terminus located radially away from the nanoparticle. The Cys sulfur atom is deprotonated and bears an extra electron to simulate the strong binding between sulfur atoms and the polarizable gold surface. Overall, the high interaction energy between the charged sulfur atoms and the gold nanoparticle surface is constituted of attractive and repulsive Coulomb terms (S^- with AUC and AU, respectively) and a 12-6 LJ potential term (S^- with AU, ε of 6.90 kJ/mol and σ of 0.30 nm for AU-S sulfide).[26] Thus, the cysteine sulfur atoms are responsible for anchoring the peptide on the gold nanoparticle surface, but because they are not directly bound, the computational model developed here has the advantage of accounting for the motion of the sulfur atoms over the nanoparticle surface.[32] The initial distance between the Cys sulfur atoms and the gold surface was set to 0.25

nm, within the range of 0.22 - 0.26 nm determined by X-ray diffraction analysis for a *p*-mercaptobenzoic acid-capped GNP.[33] The average distributions in distance between AU and sulfur atoms in the equilibrated systems (Fig. S2 in the Supporting Information) show, taking into account the uneven GNP surface, that after equilibration the sulfur atoms remain at the expected distance from the nominal surface. Moreover, we note that, because of the polarizable gold atoms, not only the deprotonated thiol group, but also the charged amino and carboxylate functional peptide groups interact with the GNP surface, but with somewhat weaker van der Waals interaction energies than the thiol group. Indeed, the amino groups are found at similar distance to the GNP surface as the sulfur atoms (Fig. S2). This is in agreement with the experimental observation that protonated amino groups interact with gold surfaces[34] and contribute to anchoring the peptides on the GNP.[9]

It is worth highlighting that the representation of the gold-thiolate bond with negatively charged sulfur atoms is not realistic; the negative charge is there simply to simulate tight binding to the surface and yet allow for mobility over the surface. Indeed, it is known that the sulfhydryl functional group (SH) in a thiol ligand (RSH), when interacting with the gold surface, gets deprotonated forming a thiyl radical, i.e., $S^{\bullet}$, which then form the gold-thiolate (RS-Au) bond, responsible for anchoring the SAM on the gold surface.[4] The reaction for the chemisorption of thiol ligands on gold can be written as follows:

$$RS\text{-}H + Au_n \rightarrow RS\text{-}Au + Au_n + \tfrac{1}{2}\, H_2$$

However, we note that the negative charge on the sulfurs is countered by the positive charge on the adjacent protonated N-termini. Thus, there is no net charge at the nanoparticle-peptide interface, which is most likely realistic. Moreover, the deprotonated C-termini are flexible and free to move and hence, they are not as close together as the N-termini. Also, we do note that we observe a distribution of the sodium counterions very similar to the distance distribution between the N- and C- peptide terminal atoms (data not shown), indicating that they are largely countering the repulsive interactions between the termini.

Taking into account the experimentally determined peptide capping density to be modelled, a number of peptides (for symmetry reasons limited to values of $4n^2+2$, where n is an integer) was roughly equidistantly placed around a gold nanoparticle of desired size.

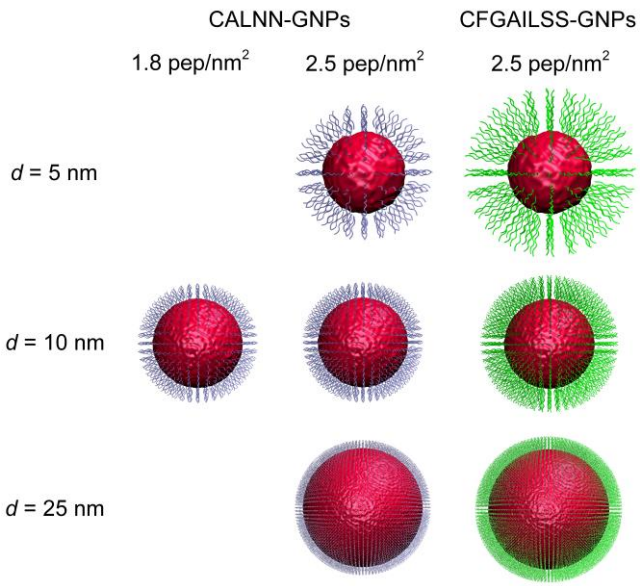

Figure 1. Snapshots of CALNN- and CFGAILSS-capped gold nanoparticle starting structures; (left) CALNN-capped 10 nm GNP at a capping density of ~1.8 peptides/nm^2; (center) CALNN-capped 5, 10 and 25 nm GNPs at a capping density of ~2.5 peptides/nm^2; (right) CFGAILSS-capped 5, 10 and 25 nm GNPs at a capping density of ~2.5 peptides/nm^2. For clarity, water and sodium ions are not shown and the display scales are adjusted for each particle size.

To investigate the effect of the capping density on the structure of a CALNN monolayer on a GNP, molecular dynamics (MD) simulations for CALNN-capped GNPs at high and low capping density were performed. CALNN peptides were arranged around a spherical GNP of diameter 10 nm at a capping density of either 2.5 ($N_{peptide}$ = 786) or 1.8 ($N_{peptide}$ = 578) peptides/nm^2. These structures were placed in a cubic box with sides of length 17 nm; 786 or 578 sodium ions were added to neutralize the system. Water molecules were placed around the CALNN-capped gold nanoparticle to obtain a water density of ~1 g/cm^3 after full equilibration. A schematic representation of the starting structures of the two systems is shown in Figure 1.

To study the effect of GNP curvature on the structure of CALNN and CFGAILSS monolayers on gold nanoparticles, MD simulations for CALNN- and CFGAILSS-capped GNPs of 5, 10 and 25 nm in diameter were carried out. The peptide capping density was kept as close as possible to the experimental values[27,35] of 2.4 and 2.55 peptides/nm^2 for CALNN- and CFGAILSS-capped GNPs, respectively ($N_{peptide}$ = 198, 786, and 4626 (CALNN) or 4902 (CFGAILSS) for the three nanoparticle sizes). These structures were placed in a cubic box with sides of length 12, 17 or 32 nm, respectively. Similarly to the previous systems, sodium ions were added to

neutralize the system and the water density was ~1 g/cm^3 after full equilibration. It is worth remarking that the size of the cubic box was chosen in order for all the systems to have roughly the same distance between the fully extended peptide and the walls of the box. A schematic representation of the starting structures of the six systems is shown in Figure 1.

The peptide-capped GNP was first energy-minimized in vacuum with the steepest descendent method. Consecutive NVT ensembles were then applied using the Berendsen method[36] to couple the temperature at 298 K; the gold nanoparticle and the peptides were coupled separately. The Verlet cut-off scheme at 1.2 and 1.4 nm for short and long-range neighbor lists was used and the lists were updated every 100 fs. Both Coulomb and van der Waals interactions were calculated with a cut-off at 1.2 nm. The peptide-capped GNP was then solvated using the TIP3P water model[37] at a density of ~1 g/cm^3 and the negative charges of the carboxylate functional groups neutralized by addition of sodium ions. Equilibration of the whole system in an NVT ensemble was carried out using the Berendsen method[36] to maintain the temperature at 298 K and coupling the gold nanoparticle, the peptides, and the solvent together with the ions in three separated groups. The short-range and long-range neighbor lists had a cut-off at 1.2 and 1.4 nm using the group cut-off scheme and were updated every 20 fs. Long-range electrostatic interactions were treated with the Particle-mesh Ewald method[38] with a Fourier grid spacing of 0.12 nm. The short-range van der Waals interactions were calculated using a switching function between 1.0 and 1.2 nm. The bond lengths were constrained via the LINCS algorithm,[39] a time step of 1 fs was used and periodic boundary conditions were adopted. Depending on the system size, equilibrium was reached after different simulation times, as assessed by macroscopic parameters, such as the total energy, being constant over time. Hence, structures with 5 nm GNPs required at least 20 ns to equilibrate, whereas those with 10 or 25 nm GNPs took more than 30 or 40 ns, respectively; data were then collected for the subsequent 10 ns ("production run"). Furthermore, in order to test the reproducibility of the computational results, the CFGAILSS-capped 10 nm GNP was also simulated with different starting conditions, i.e., using the Berendsen method[36] to couple the temperature at 348 K for the first set of NVT ensembles applied on the gold nanoparticle and the peptides. All the analyses were done using programs in the GROMACS package and custom-written software. For secondary structure assignment, the DSSP algorithm[40] was employed. Visual Molecular Dynamics

version 1.9.1[41] was used to visualize and render the structures and create the movie available in the SI.

Results and Discussion

Effect of Capping Density on the Structure of a CALNN Monolayer (Experimental Investigation).

The CALNN pentapeptide was designed to form a self-assembled monolayer around GNPs and thus impart colloidal stability.[9] Amino-acid analysis revealed that the peptide capping density, hence the monolayer compactness, is dependent on the concentration of peptide used during the ligand exchange procedure.[35] We previously investigated the secondary structure of CALNN monolayer by FTIR spectroscopy and reported both a random coil[27] and a straight conformation.[42] In the latter work, we hypothesized a difference in the peptide capping density to underlie these divergent observations. Here, a more systematic experimental study on CALNN-capped GNPs at different capping densities is presented in parallel with molecular dynamics simulations.

FTIR spectroscopy was employed, first, to estimate the CALNN capping density and, second, to characterize the secondary structure of the monolayer. In particular, the amide I' region (1600 to 1700 cm^{-1}), mainly associated with the backbone carbonyl stretching vibration, which gives information on the backbone conformation,[43] was analyzed. The amide I' band area was used to estimate the peptide capping density (Supporting Information for details and unscaled FTIR spectra, Figure S3), taking into account the GNP concentration, as determined by UV-vis spectroscopy, and the IR surface selection rules, which quantitatively describe the strength of the IR-active modes of small molecules bound to a metal surface or nanoparticle, as described in detail previously.[42] The estimated capping density for CALNN-capped GNPs at high and low capping density are 2.1 and 1.4 peptides/nm^2, in reasonable agreement with those reported previously, using amino-acid analysis, for CALNN-GNPs prepared with the same ligand exchange procedures (2.4 and 1.7 peptides/nm^2, respectively).[35] The FTIR spectra of CALNN peptide in solution and of CALNN-capped GNPs at high and low capping density are shown in Figure 2. The amide I' band of CALNN peptide at 1651 cm^{-1}, corresponding to a random coil conformation,[44] shifts to 1648 cm^{-1} and 1641 cm^{-1} when constituting the low and high capping density monolayer, respectively. The position

of the former is still indicative of a largely disordered peptide monolayer, whereas the latter is denoting a straight conformation, either polyproline II (PPII) or β-strand;[45–47] although one of the bands observed for parallel β-sheets is at a very similar position,[27] the accompanying high-frequency band is missing here, allowing us to rule out this structure. The PPII motif[48] is not only found in proline-rich polypeptides, but also in nominally disordered polypeptides[45,49] and is characterized by the lack of internal hydrogen bonding. As for the β-strand, it corresponds to a single peptide strand in a β-conformation, i.e., a quite extended structure lacking the stabilizing cross-strand hydrogen bonds that would form a β-sheet. In the absence of an internal network of stabilizing hydrogen bonds, both motifs are thought to be stabilized by hydrogen bonds between the peptide backbone and the surrounding water molecules[50] and the amino acids within such structures expose to the solvent 60% more polar surface area compared to other residues.[51] Hence, the amide I' band in the IR spectrum of CALNN-capped GNPs with low capping density indicates a capping layer consisting of largely disordered peptides, whereas that of high capping density CALNN-capped GNPs, while indicating a straight conformation, is not in agreement with a β-sheet-like structure; however, the experimental results cannot distinguish between PPII and β-strand conformations for this system.

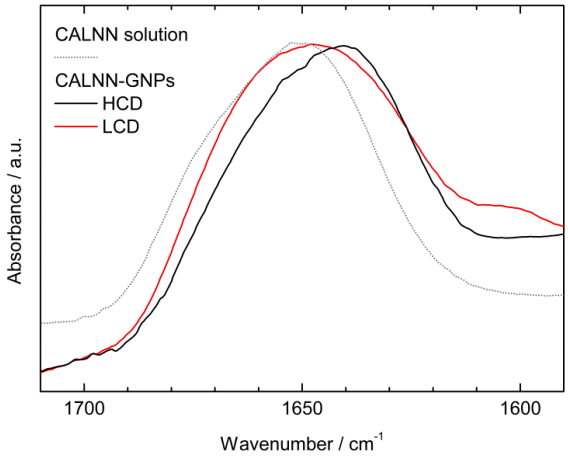

Figure 2. FTIR spectra in the amide I' region of CALNN peptide in solution and of 11 nm CALNN-capped gold nanoparticles at high and low capping density (HCD and LCD, respectively). All spectra have been scaled to the same maximum absorbance.

Effect of Capping Density on the Structure of a CALNN Monolayer (Computational Investigation).

Molecular dynamics simulations of two systems that model the high and low capping density CALNN-capped GNPs were performed. The former and the latter had a CALNN capping density of 2.5 and 1.8 peptides/nm^2 on a GNP of 10 nm diameter, respectively (see Computational Model section), to roughly reflect the ~30% difference in capping density of the CALNN-capped GNPs analyzed by FTIR spectroscopy. The starting structures of the two simulated systems are shown in Figure 1.

To establish the validity of the computational model, the secondary structure of the simulated high and low capping density CALNN monolayers on GNPs was compared to the IR experimental findings. The time-evolving secondary structure of CALNN peptides within the high and low capping density monolayers, based on DSSP assignment,[40] is shown in the top panels of Figure 3 (see Supporting Information, section S4, for comments on the DSSP algorithm). It is worth noting that the secondary structure is stable over time in both simulated systems (Figures 3A,B). The overall content of well-defined structures, as identified by the DSSP algorithm, is very small in both systems, with more than 90% of the content identified as "random coil". On the other hand, there is a noticeable difference between the low and high capping density monolayers - whereas for the former less than 2% of the residues are found in β-structures (i.e. β-sheet or β-bridge), slightly more (5%) are in these conformations for the latter. Thus, the high capping density monolayer appears to be more structured. However, as discussed above, the amide I' band in the FTIR spectrum of high capping density CALNN-capped GNPs is indicative of a PPII or β-strand conformation, both extended secondary structure motifs lacking intermolecular hydrogen bonding. Because the DSSP secondary structure assignment[40] is mostly based on the recognition of hydrogen bonds and therefore fails in the identification of such motifs, the backbone φ and ψ torsion angles for the two simulated systems were also analyzed to gain more detailed information on the local backbone conformation (Figure 3, bottom; see also section S5 in the Supporting Information for details of the residues considered and a quantitative analysis of the Ramachandran plots). Characteristic φ and ψ ranges are associated with well-defined secondary structure motifs.[52] For instance, typical values for antiparallel β-sheets are φ = -147°, ψ = +145°,[53] for parallel β-sheets φ

= -116°, ψ = +112°,[53] for PPII φ = -75°, ψ = +145° and for right-handed α-helices φ = -60°, ψ = -45°. Thus, extended backbone structures are found near the top left corner of the Ramachandran plot. Figures 3 C and D show that a significant fraction of residues are found in this region for both systems. However, there is a significant shift of population from the helical region to the region of extended conformations, indicating a "straightening" of the peptides, upon increasing the capping density. It should be noted that Ramachandran plots show the conformation of individual residues and population in the α-helical region does not indicate formation of helical secondary structures, which does not occur for CALNN, see Figure 3A,B. Thus, the structure information arising from DSSP and Ramachandran analyses are complementary and indicate a more structured monolayer with more extended peptides in the case of GNPs with a higher capping density of CALNN peptide; most of these extended peptides, however, do not form hydrogen-bonded β-sheets. All of these results are in good agreement with the conclusions drawn from the experimental FTIR spectra. Moreover, the Ramachandran plot suggests that the extended β-strand conformation is somewhat preferred over the PPII conformation in high capping density CALNN monolayers, although both conformations are found.

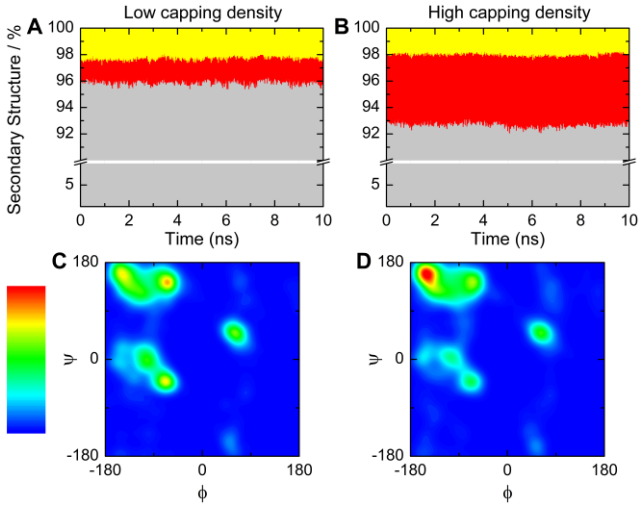

Figure 3. Secondary structure of CALNN monolayers, based on (top) DSSP assignment over time and (bottom) Ramachandran analysis of the final structure for 10 nm CALNN-capped GNPs at low (A,C) and high (B,D) capping density. Secondary structure color code in A and B: grey, random coil; red, β-structures (i.e., β-sheet or β-bridge); yellow, turn. The Ramachandran plots are colored by occupancy; the intensity scale range is from 0 (dark blue) to 0.00012 (red) residue probability/angle^2.

The fact that the simulated secondary structure content well reflects the IR experimental findings supports the validity of the computational model, from which further insights into the monolayers can be gained.

To estimate how extended the CALNN peptides are, the distance distribution between the N- and C- peptide terminal atoms was examined (Figure 4A). For both systems, a similar fraction of peptides was found to be significantly folded back onto themselves ($d_{N\text{-}C} \leq \sim 1$ nm). On the other hand, in the region of more extended conformations ($d_{N\text{-}C} \geq \sim 1$ nm), there are clear differences; for the high capping density system, the $d_{N\text{-}C}$ distribution is narrower and shifted towards the straight conformation ($d_{N\text{-}C} \sim 1.6$ nm for an antiparallel β-strand[53] or ~ 1.5 nm for a PPII structure[54] consisting of 5 residues), reflecting the need for more ordered conformations in a monolayer of higher compactness. These findings are supported by visual inspection of the structures, see the snapshots in Figure 4, which show that both high (Figure 4B) and low (Figure 4D) capping density monolayers are characterized not only by some back-folding of peptide chains, but also by peptides in an extended conformation, although the latter are more dominant in the high capping density system.

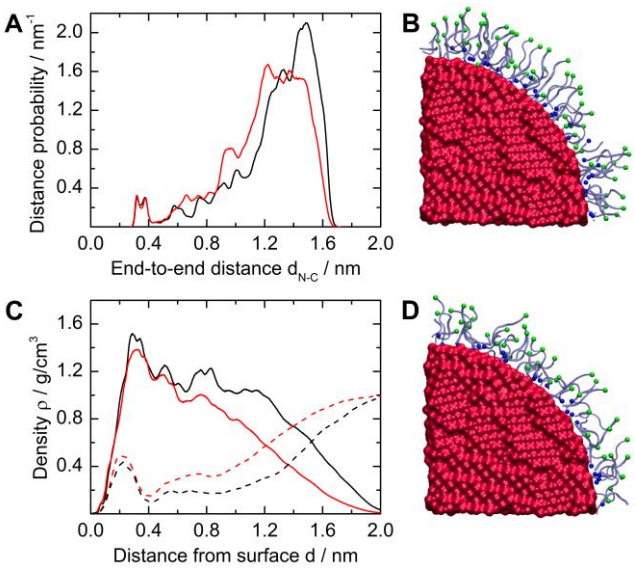

Figure 4. Extension of CALNN peptides analyzed by (A) distribution of the distance $d_{N\text{-}C}$ between the peptide N- and C-terminal atoms and (C) radial density of peptide (solid lines) and water (dashed lines) atoms at distance d from the surface of the GNP. Black and red curves refer to the high and low capping density system, respectively. All results were averaged over 10 ns simulation. Snapshots of final structures of 10 nm CALNN-capped GNPs at high and low capping density are illustrated in B and D, respectively (shown is one-eighth of the structure); the peptide N- and C-terminal atoms are rendered in blue and green, respectively.

Further information about the internal structure of the monolayers can be gained from the radial density profiles of peptide and water atoms shown in Figure 4C. For the high capping density system, the density profile of peptide atoms (Figure 4C, solid black line) shows an almost constant value of ~1.2 g/cm^3 up to ~1.2 nm from the GNP surface, which is close to the widely accepted density for polypeptides[55] of 1.4 g/cm^3; the radial density profile of water atoms (Figure 4C, dashed black line) indeed shows that not much solvent is present in this region, confirming the presence of a compact peptide monolayer. The gradual decay of the peptide atom density at larger distances from the gold surface reflects the mobility and disorder of the peptide carboxyl ends. For the low capping density system (Figure 4C, red lines), on the other hand, no such region of constant peptide atom density was found; the decay is more gradual and is accompanied by a more gradual increase of the water content in the capping layer, confirming the significantly more disordered nature of the low capping density monolayer, in spite of the fact that the capping density is reduced by only 26%. It is interesting to note, however, that almost the same amount of water appears to be trapped near the GNP surface for both monolayers.

The radial density profiles also allow the determination of an effective capping layer thickness, which is a quantity that could be compared to experimental results, obtained e.g., by Dynamic Light Scattering or Differential Centrifugal Sedimentation (DCS) techniques. For the sake of avoiding ambiguity, we here define the effective thickness as the distance from the GNP surface at which the peptide atoms have the same density as the solvent, which yields values of 1.21 and 1.52 nm for high and low capping density CALNN-capped GNPs, respectively. Interestingly, this estimated thickness of the high capping density system is only slightly less than the predicted length of 1.7 nm for an antiparallel β-strand consisting of 5 residues,[53] and in very good agreement with the predicted length of a 5-residue PPII structure.[54]

Thus, FTIR spectroscopy showed that even a relatively small change of the CALNN capping density does have a significant effect on the structure of the monolayer on a GNP, suggesting that CALNN peptides have to adopt a more extended structure in order to organize in a monolayer with high capping density. The computational model proposed here does not only fully reproduce this effect, but also allows more detailed insight into the secondary structure motifs and structural properties of CALNN monolayers at different capping densities. This provides molecular details which have not yet been observed experimentally,

including a pocket of water close to the gold surface and a small proportion of peptides in a loop configuration with their C-terminus in contact with the gold surface.

Effect of Surface Curvature on the Structure of CALNN and CFGAILSS Monolayers.

In previous experimental work,[27] we investigated the secondary structure of CALNN and CFGAILSS peptide monolayers on GNPs of different sizes, i.e., 5, 10 and 25 nm in diameter, by means of FTIR and solid-state nuclear magnetic resonance (ssNMR) spectroscopies. CALNN was found to adopt a random coil conformation independent of the GNP size, whereas CFGAILSS, which forms extended amyloid fibers with antiparallel β-sheet conformation in solution, showed a propensity to form parallel β-sheets when attached to GNPs which depended on GNP size, i.e., curvature, with almost no β-sheets observed on 5 nm GNPs, some β–sheet formation on 10 nm GNPs, and significant β–sheet propensity on the 25 nm large nanoparticles. A geometrical model was proposed in order to rationalize the role of the nanoparticle curvature on the secondary structure of CFGAILSS. According to this model, the number of adjacent peptides that can form hydrogen bonds and therefore be involved in parallel β-sheets is dictated by the nanoparticle curvature. Thus, more extended parallel β-sheets are observed on the larger nanoparticles, presenting the lower curvature. In the IR investigation of Mandal et al., a Leu-rich peptide was found to be more prone to form α-helices on gold nanoparticles presenting lower curvature, possibly because of a greater inter-peptide distance.[56] Therefore, these IR studies highlighted the importance of the peptide sequence and nanoparticle size when designing peptide-capped gold nanoparticles with well-defined secondary structure motifs.

Here, the experimentally characterized CALNN- and CFGAILSS-capped GNPs with 5, 10 and 25 nm diameter were translated into six computational systems illustrated in Figure 1. The peptide capping density reflected as closely as possible the experimental values[27,35] measured by amino acid analysis of 2.4 and 2.55 peptides/nm^2 for CALNN- and CFGAILSS-capped GNPs, respectively (see Computational Model section).

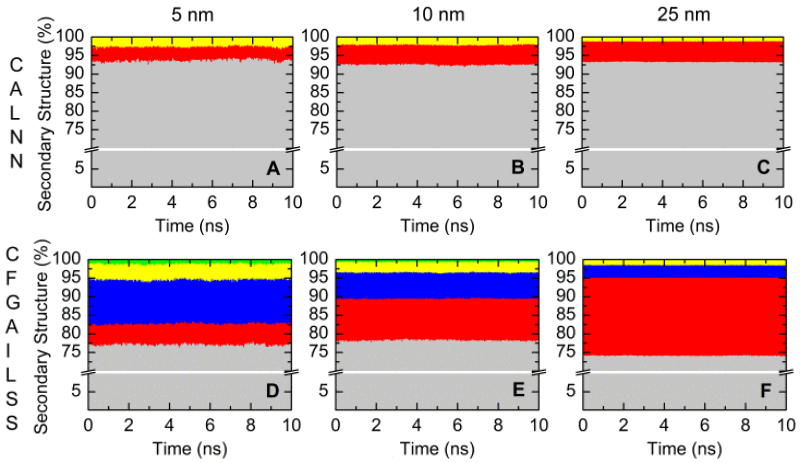

Figure 5. Time-evolving secondary structure for CALNN (top) and CFGAILSS (bottom) monolayers on 5 (A,D), 10 (B,E) and 25 nm (C,F) GNPs, based on DSSP assignment. Secondary structure color code: grey, random coil; red, β-structures (i.e., β-sheet or β-bridge); blue, bend; yellow, turn; green, helix.

The peptide secondary structures found in the computational model can be directly compared to the experimental results. Figure 5 illustrates that the secondary structure remains constant over the 10 ns "production run" in all systems and that significant differences between GNPs of different sizes can be observed for CFGAILSS monolayers. For instance, with the increase of the GNP diameter from 5 to 10 nm (Figure 5D,E), the content in β-structures in CFGAILSS monolayers sees a moderate growth from ~5.5 to 11%, whereas a more dramatic increase to ~21% can be observed upon increasing the GNP size to 25 nm (Figure 5E,F). This increase of β-structures is accompanied by a loss of bending conformations. For CALNN monolayers, the changes in secondary structure motifs with an increase in GNP size are much smaller (Figure 5A-C). Thus, based on DSSP secondary structure assignment, the simulations are in remarkably good agreement with the FTIR and ssNMR observations of ref. [27]. In the case of CFGAILSS systems, they confirm a small difference in the amount of β-structures between 5 and 10 nm GNPs and that the highest β-content is on the GNP with lower curvature, i.e., the 25 nm GNP. In the case of CALNN monolayers, they indicate a small increase in β-structures on the larger GNPs, but confirm a mostly random coil conformation, independent of the nanoparticle size. However, as previously mentioned, the DSSP secondary structure assignment is mostly based on the recognition of hydrogen bonds between amino acids,[40] and thus cannot account for secondary structure motifs that are not denoted by intermolecular hydrogen bonding, such as PPII and β-strand structures.

To derive conclusions on these structures, the backbone φ and ψ torsion angles were analyzed. With an increase of the GNP diameter from 5 to 10 nm, the Ramachandran plots of CALNN systems (Figure 6A,C, see also Table S1 in the Supporting Information for a quantitative analysis of the Ramachandran plots) indicate a shift of population from the PPII (φ = -75°, ψ = +145°) and particularly the right-handed α-helical (φ = -60°, ψ = -45°) regions to the antiparallel β-sheet region (φ = -147°, ψ = +145°), indicating a "straightening" of the peptides. Thus, decreasing the curvature forces the peptides into a more extended conformation, similar to the effect of increasing the capping density on 10 nm GNPs, as discussed above. On the other hand, almost no difference is observed between 10 and 25 nm CALNN-capped GNPs (Figure 6C,E), in agreement with the DSSP analysis results of Figure 5. In the case of the CFGAILSS systems, a similar, but much more pronounced shift of population from the right-handed α-helical to the extended region, and within the extended region a shift from the PPII to the antiparallel and parallel β-sheet regions is observed with an increase of the GNP size, (Figure 6B,D,F); it is particularly noteworthy that the increase from 10 to 25 nm GNP diameter leads not only to a significant increase of population in the β-sheet region in general, but to a pronounced redistribution of the β-sheet conformations towards the parallel β-sheet region (φ = -116°, ψ = +112°). Thus, the structural information arising from DSSP and Ramachandran analyses support each other, and show that the simulations are in good agreement with the conclusions which had been drawn from FTIR and ssNMR spectroscopy.

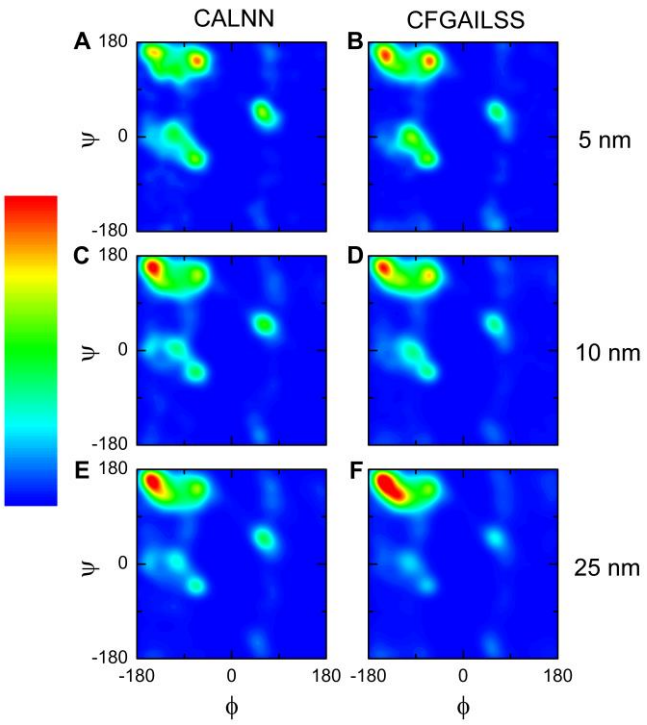

Figure 6. Ramachandran plots of the final structure for CALNN (left) and CFGAILSS (right) monolayers on 5 (A,B), 10 (C,D) and 25 nm (E,F) GNPs. The plots are colored by occupancy; the intensity scale range is from 0 (dark blue) to 0.00012 (red) residue probability/angle^2.

The fact that the simulated secondary structure content well reflects the experimental findings supports the validity of the computational model, from which further insights into the monolayers can be gained.

To assess the structure at the peptide level, the distance distribution between the N- and C- peptide terminal atoms was examined. The profiles for CALNN-capped GNPs (Figure 7A) highlight that a portion of CALNN peptides is back-folding on the GNP surface ($d_{N\text{-}C} \leq \sim 1$ nm). Also, they confirm, in line with the results for the secondary structure, that with an increase of GNP size, hence a decrease of curvature, there is some degree of "straightening" – with increasing GNP size, the $d_{N\text{-}C}$ distribution narrows and shifts towards the straight conformation ($d_{N\text{-}C}$ ~1.6 nm for an antiparallel β-strand[53] or ~1.5 nm for the PPII structure[54] consisting of 5 residues). This curvature-induced straightening is comparable to the effect of increasing the capping density, see above; here, the reduced curvature of the larger GNPs pushes the peptide C-termini together, which leads to a more compact capping layer and thus requires a more ordered peptide conformation. It is noteworthy that most of this effect occurs upon an increase of the GNP diameter

from 5 to 10 nm, whereas a further increase has almost no effect on the distribution of d_{N-C}. In contrast, CFGAILSS-capped GNPs (Figure 7B) show much less peptide back-folding, with almost no population in the region $d_{N-C} \leq \sim 1.5$ nm, and a much more pronounced shift to almost fully extended peptide conformations (d_{N-C} = 2.7 nm for an antiparallel β-strand consisting of 8 residues)[53] with increasing GNP size; unlike CALNN, the effect is more pronounced when comparing 10 and 25 nm GNPs. This again is in full agreement with the secondary structural analysis of the simulations, as well as with the experimental results for a CFGAILSS capping layer on GNPs of increasing size. Thus, in addition to the higher compactness of the capping layer as a consequence of decreased GNP surface curvature, which is observed even for an unstructured peptide like CALNN, there is another effect operating for CFGAILSS: this peptide has a significant propensity for forming β-sheets, but when the N-termini are attached to a high curvature surface, the backbones of adjacent peptides are too far shifted relative to each other to allow inter-strand hydrogen bond formation. Increasing the GNP size, and hence decreasing the surface curvature, reduces this misalignment and thus leads to increased β-sheet formation which provides an additional "driving force" for peptide straightening. Although some β -sheet formation already can occur on 10 nm GNPs, the surface curvature still prevents formation of extended β-sheets; only on the 25 nm GNPs can this be observed.

To gain more information about the structure of the monolayer and to estimate its thickness, the radial density of peptide and water atoms was analyzed (Figures 7C,D). As discussed before, CALNN peptides in a high capping density monolayer on a 10 nm GNP display a compact monolayer characterized by a peptide density which is close to the widely accepted density for polypeptides[55] of 1.4 g/cm^3 and low water content. Almost the same density profile is found for the larger 25 nm GNPs, whereas for the small (5 nm) GNPs, a less compact peptide layer, characterized by a more gradual decay of the peptide density and higher water content, was found, which is reminiscent of the low capping density CALNN layer on 10 nm GNPs. The effective thickness, i.e., the distance from the GNP surface at which the peptide and water density are equal, increases from 1.25 nm for the 5 nm GNPs to 1.52 nm (10 nm GNPs) and 1.67 nm (25 nm GNPs). On the other hand, the effect of nanoparticle curvature on the compactness of a CFGAILSS monolayer, as indicated by the radial density, is much more pronounced than for a CALNN monolayer. While the two monolayers show a similar gradual decrease of peptide density on 5 nm GNPs, on

10 nm GNPs the CFGAILSS monolayer is less compact, with a significantly lower peptide density, than a CALNN monolayer with the same capping density. Only for 25 nm GNPs does the CFGAILSS capping layer become as compact and dense as the CALNN monolayer, with a high peptide density close to that of polypeptides and low water content up to ~2 nm from the GNP surface. The effective CFGAILSS layer thickness increases from 1.71 nm for the 5 nm GNPs to 2.01 nm (10 nm GNPs) and 2.50 nm (25 nm GNPs). The latter value is in good agreement with the length of a parallel β-sheet consisting of 8 residues (2.60 nm).[53] As already noted above for CALNN monolayers of varying packing density, some water appears to be trapped near the GNP surface also for CFGAILSS monolayers, with some decrease of the water density near the surface as the GNP curvature decreases.

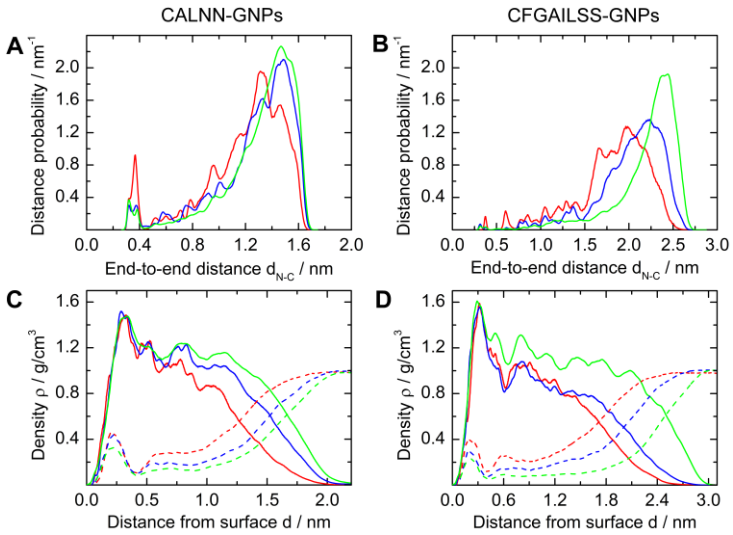

Figure 7. Extension of CALNN (left) and CFGAILSS (right) peptides analyzed by (A,B) distribution of the distance d_{N-C} between the peptide N- and C-terminal atoms and (C,D) radial density of peptide (solid lines) and water (dashed lines) atoms at distance d from the surface of the GNP for CALNN- and CFGAILSS-capped 5 (red lines), 10 (blue lines) and 25 nm (green lines) GNPs, averaged over 10 ns simulation.

Insights into the β-structures within CFGAILSS Monolayers.

Since, as discussed above, most of the straightening of CALNN peptide is not accompanied by inter-strand hydrogen bonding and hence is not well captured by DSSP analysis, we focused on CFGAILSS monolayers to gain more detailed insights into secondary structure motifs. Figure 8 shows the percentage of secondary structure, as identified by DSSP analysis,[40] for each residue in CFGAILSS peptide chain (due to DSSP analysis limitations no secondary structures are assigned to the

first and the final two residues, see Supporting Information, section S4, for more comments on the DSSP analysis). The profiles illustrate that decreasing the GNP curvature leads to an increase of β-structures and decrease of bending predominantly for the inner segment Phe-Ile, with Gly-Ala having the largest β-content. Moreover, the average length of β-structures is 1.3, 1.8 and 2.3 residues for 5, 10 and 25 nm CFGAILSS-capped GNPs, respectively. Hence, more extended segments of peptide participate in β-structure formation on the nanoparticles with lower curvature, i.e., larger size.

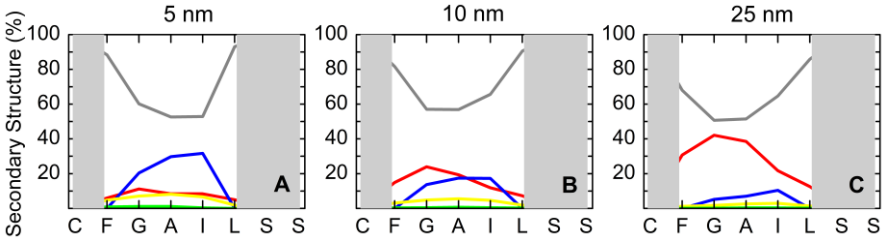

Figure 8. Secondary structure content per amino acid for CFGAILSS monolayer on 5 (A), 10 (B) and 25 nm (C) GNPs, based on DSSP assignment, averaged over the last 2 ns of the simulation. The grey areas depict the amino acids not identifiable with secondary structure motifs due to limitations of the DSSP algorithm. Secondary structure color code: grey, random coil; red, β-structures (i.e., β-sheet or β-bridge); blue, bend; yellow, turn; green, helix.

The snapshots in Figure 9 show that not only does the number of parallel β-sheets increase with a decrease in nanoparticle curvature, but they also appear to associate into more extended parallel β-sheet domains.

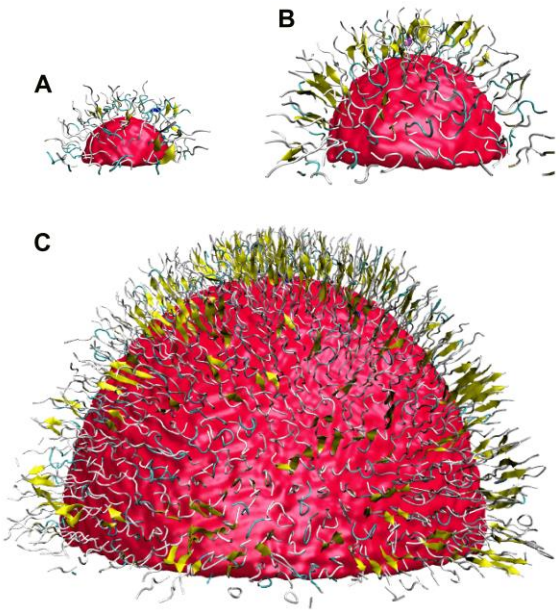

Figure 9. Snapshots of a portion of the final structures of CFGAILSS-capped 5 (A), 10 (B) and 25 (C) nm GNPs. Peptides are rendered with the VMD "New Cartoon" drawing method and colored per secondary structure motif; β-sheets are illustrated as yellow arrows. The images are to scale and shown in perspective.

To explore the existence of such supra-molecular domains within CFGAILSS monolayers, the distribution of β-structure probability is displayed on polar charts (Figure 10; polar charts of the other hemispheres are shown in the Supporting Information, Figure S5). The black dots indicate the position of the backbone center of mass for each peptide. The local distributions of β-structure probability clearly illustrate that a high nanoparticle curvature (Panel A) limits the size of β-structure domains to not more than two or three peptides, since the curvature leads to misalignment of neighboring peptide backbones, whereas a low nanoparticle curvature allows the formation of extended β-structure domains (Panel C). Also, the β-structures appear to be randomly distributed across the nanoparticles. It is worth noting that the spatial distribution of β-structures does not change much during the 10 ns "production run", indicating that the full conformational landscape is not accessed over the ns-timescale of molecular dynamics simulations, in agreement with the known time scales of secondary structure equilibration dynamics, see below. The results for a CFGAILSS-capped 10 nm GNP simulated with different starting conditions (see Computational Model section for details), show indeed a similar β-structure content as the 10 nm CFGAILSS-capped GNP previously discussed, i.e., 9 and 11%, respectively, but a different spatial distribution of β-

structures, see Figure S7 in the Supporting Information. This structure represents another one of the many local minima on the shallow conformational landscape with different local structures, but very similar average properties, which make up the equilibrium ensemble. Because of the time scale of secondary structure equilibration dynamics, see below, transitions between these local minima occur on longer time scales than those available to molecular dynamics simulations. However, the observation that the average properties of the two structures simulated with different starting conditions are highly similar confirms that the results obtained here are valid and relevant for comparison with experimental results, which necessarily are ensemble averages. For reference, the polar charts for the CALNN monolayers are reported in Figure S6; these show significantly lower β-structure probabilities, in agreement with the results presented above, and consequently no extended β-structure domains.

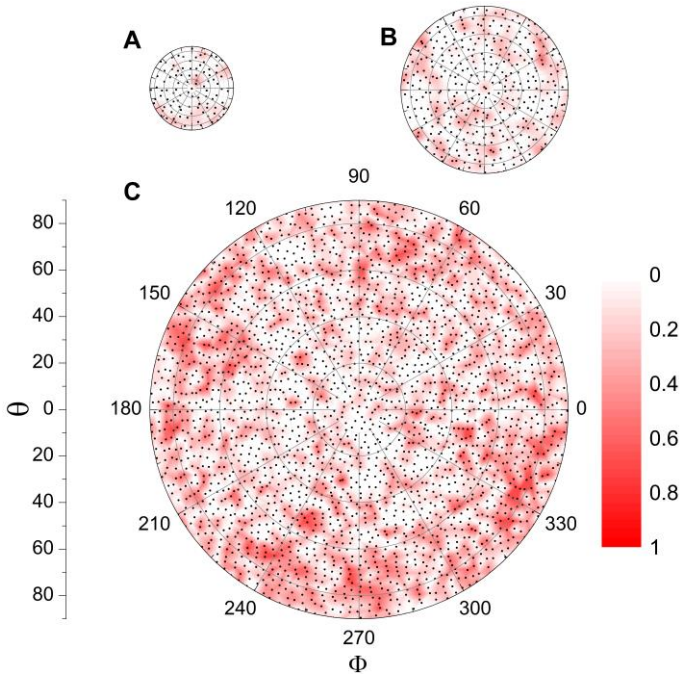

Figure 10. Spatial distribution of β-structure probability, as assessed by DSSP analysis, displayed on polar charts, where Φ and θ indicate the azimuthal and polar angle in spherical coordinates, respectively, for the final structures of CFGAILSS-capped 5 (A), 10 (B) and 25 nm (C) GNPs. The black points indicate the polar position of the backbone center of mass of each peptide; the color contour shows the local β-structure probability.

Close inspection of the distribution of peptides in the domains of high β-structure content within the CFGAILSS capping layer on 25 nm GNPs suggests that

these peptides arrange in regular repeat patterns in two dimensions (Figure 11B). Many of these peptides are found in lines with a typical inter-peptide distance of ~0.5 nm, which is in good agreement with the distance between two β-strands in a parallel β-sheet, i.e., 0.47 nm. Furthermore, these lines of peptides often run parallel to each other, with a distance on the order of ~1 nm, corresponding to the inter-β-sheet distance in amyloid fibrils, which consist of stacked β-sheets.[57] Thus, we suggest that on 25 nm GNPs CFGAILSS peptides arrange in an amyloid-like structure consisting of stacked parallel β-sheets. The stacking of parallel β-sheets is in contrast to most amyloid structures, including those formed by CFGAILSS peptides in solution,[27] which consist of antiparallel β-sheets; however, binding of the peptides to the GNP surface by their N-terminus necessarily prevents the formation of antiparallel β-sheets. For a more quantitative confirmation of this suggestion, the radial distribution function of the backbone-backbone distances was analyzed (Figure 11A). The nearest neighbor distribution for peptides with no β-structures shows a maximum at ~0.78 nm; interestingly, this corresponds to a capping density of less than 2 peptides/nm^2, which is much smaller than the average capping density (2.5 peptides/nm^2), showing that formation of β-sheets occurs in domains of increased capping density, which leads to depletion of the remaining surface. This suggests that movement of the sulfur atoms on the gold surface may be critical to the formation of secondary structure motifs. Simulations in which sulfur atoms were strongly bound to the gold surface were also performed (for details of these simulations, see Supporting Information, section S2). In contradiction to the experimental findings[27] and the results obtained using the GolP-CHARMM force field, CFGAILSS-capped 10 nm GNP simulated with this computational model showed no significant secondary structure formation (Figure S8), thus confirming the importance of the mobility of peptides on the surface (from the starting to the final structure, the sulfur atoms moved on average by ~0.1 nm in the CHARMM-METAL model and by ~0.4 nm in the GolP-CHARMM model).

In contrast, the radial distribution functions for peptides with high β-content (>0.7) are characterized by maxima at 0.5 and 0.95 nm, corresponding to the inter-β-strand and inter-β-sheet distances found in amyloid fibrils, which confirms the conclusion drawn above from a visual inspection of the polar plot. Figure 11C shows a snapshot of such parallel β-sheets on the nanoparticle surface that illustrates the amyloid-like arrangement of peptides within some β-structures domains. For reference, the radial distribution function of the backbone-backbone distances for

the CALNN-capped 25 nm GNP is reported in Figure S9; it shows a similar distribution for peptides with no β-structures as found for the CFGAILSS-capped 25 nm GNP, whereas no maximum at ~1 nm is found even for peptides with the highest β-sheet content, in agreement with the absence of amyloid-like structures concluded on by visual inspection of the structure.

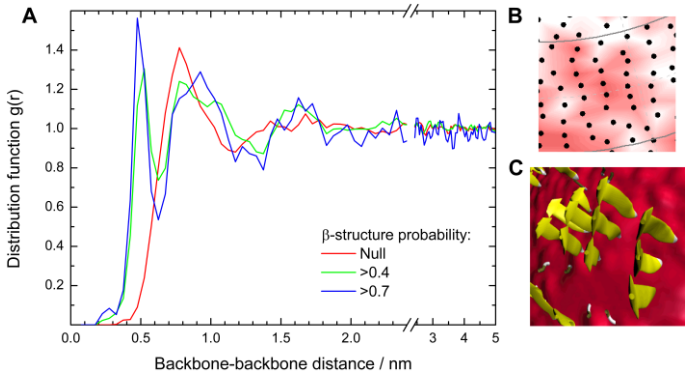

Figure 11. (A) Radial distribution functions of the backbone-backbone distances for peptides with different β-structure probabilities in a CFGAILSS-capped 25 nm GNP; the profiles are the result of averaging over six equilibrated structures; (B) example of a β-structure domain denoted by an amyloid-like arrangement of peptides (zoom-in of Fig. 10C); (C) top-view snapshot of parallel β-sheets on gold surface, showing amyloid-like structure.

Peptide Dynamics.

The Supporting Information contains a movie of the CFGAILSS-capped 10 nm GNP, in which the secondary structure of CFGAILSS monolayer is visualized every ps over the last 100 ps of the 10 ns "production run" (the peptides are rendered with the VMD "New Cartoon" drawing method and colored per secondary structure motif; β-sheets are illustrated as yellow arrows and, for clarity, water and sodium ions are not shown). This clearly shows that the β-structures and in particular the supra-molecular domains into which they associate do not change much over time; this is valid for the full 10 ns "production run", as evidenced by the spatial distributions of β-structure probability at different times shown in Figure S10 in the Supporting Information. Moreover, as previously discussed, the CFGAILSS monolayer on a 10 nm GNP simulated with different starting conditions revealed a similar average content of β-structures, but with a completely different spatial distribution (Figure S7), which again was found to be largely constant on the 10 ns time scale. Thus, it can be concluded that over the ns-timescale which is available

to molecular dynamics simulations the individual peptides do not probe the full conformational landscape which they would sample over longer time scales. Instead, the system remains within a local minimum of the conformational landscape, corresponding to a particular distribution of β-structures. This is not surprising, since it is well known from experimental evidence that equilibration of secondary structures is slower than 10 ns. Thus, the folding/unfolding dynamics of α-helices occur on the 100 ns time scale[45] and those of β-sheet structures are even slower.[58,59] Hence, the simulations reported in this study can be considered as equilibrated with respect to the overall properties (ensemble averages), but are not ergodic, i.e., the localization of CFGAILSS β-structures averaged over the production run is not representative of an ensemble average (which would be homogenous over the surface due to the spherical symmetry). For a further analysis, the time autocorrelation of the β-structure probability for each of the five residues in the CFGAILSS peptides which can be analysed by DSPP was calculated and is shown in Figure 12.

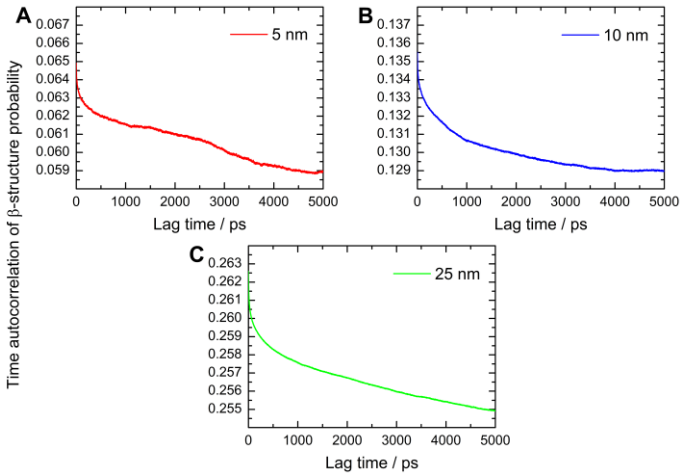

Figure 12. Time autocorrelation of β-structure probability resulting from the average of the time autocorrelation functions for F,G,A,I,L residues, averaged over all peptides, for CFGAILSS monolayer on 5 (A), 10 (B) and 25 nm (C) GNPs; β-structure probability extracted from DSSP analysis in time steps of 1 ps over the 10 ns production run.

Fig. 12 shows that only the onset of the autocorrelation decay is captured. Hence, since there is no reason to assume any particular functional time dependence for the autocorrelation functions, no exact quantitative analysis is possible, such as the determination of an autocorrelation time. However, analysis of

the onset allows the prediction that autocorrelation times exceed several 100 ns, in full agreement with the expectations for β-sheet (un)folding.[58,59]

Conclusions

Here, we have presented a computational model for peptide-capped gold nanoparticles that account for the motion of sulfur atoms over the nanoparticle surface and dynamic polarization of gold atoms. We have pointed out the crucial importance of the cysteine sulfur atoms' mobility for the formation of secondary structure motifs and described the set-up and validation of the computational model using experimentally well-characterized systems as benchmarks. Furthermore, we have shown that MD simulations provide insights not only into the peptides' structural and dynamic properties, but also into the distribution of secondary structure domains on the gold surface and into the peptides' arrangement within such domains. Therefore, while elucidating the structure of peptide monolayers on gold nanoparticles is experimentally challenging and the detailed insights attainable often limited, our study shows that a combination of experiments and modelling is quite compelling for determining the monolayer structure at different molecular levels. In the future, the computational model proposed here will be used to predict the structure of other peptide monolayers on gold nanoparticles and help with the experimental design of peptide-capped gold nanoparticles with well-defined structure motifs, which could also be assembled into objects with complexity similar to the one found in proteins.

Materials and Methods

Gold Nanoparticles. Citrate-stabilized spherical gold nanoparticles (diameter 11 nm, as determined by Differential Centrifugal Sedimentation, using a DC24000 disk centrifuge from CPS Ltd.) were synthesized following a modified Turkevich-Frens method.[60,61] In brief, 20 mL of a hot 40 mM trisodium citrate solution in Milli-Q water were added to a boiling solution of 200 μmol $HAuCl_4$ trihydrate in 200 mL Milli-Q water and refluxed under vigorous stirring for 60 min, the solution was then cooled overnight under stirring and filtered.

CALNN-Capped Gold Nanoparticles. For GNP functionalization, CALNN peptide (Peptide Protein Research Ltd., used as received) was dissolved in Milli-Q water to

give two stock solutions of 1 mg/mL and 0.05 mg/mL, respectively. To 0.5 mL of the GNP solution, 0.5 mL of Milli-Q water and 111.1 μL of the peptide stock solution were added and left overnight, the excess peptide was then removed by repetitive cycles of centrifugation and redispersion in fresh Milli-Q water, reducing the final volume to 0.5 mL.

Sample Preparation for FTIR. In total, 18 mL of each GNP colloidal dispersion (using stock solutions with high and low CALNN concentration, respectively) were prepared. These were concentrated to a volume of 1 mL by lyophilisation and re-dispersion in Milli-Q water and cleaned by dialysis against Milli-Q water, using a 10 kDa cut-off membrane. For FTIR spectroscopy, the solvent was exchanged to D2O to avoid the strong H2O absorbance which overlaps with the amide I band; this was achieved by repeated cycles of lyophilisation and re-suspension in D_2O. The GNP concentrations in the final samples were ~3 μM. as determined by UV-vis spectroscopy, using a sample diluted by a factor 400. A 10 mg/mL solution of CALNN in D_2O was used to record the FTIR spectrum of free peptide.

Fourier Transform Infrared Spectroscopy. FTIR spectra were recorded on a Bio-Rad FTS-40 FTIR spectrometer, averaging 1000 scans with 1 cm^{-1} resolution, using an IR cell with CaF2 windows and 50 μm spacer.

Associated Content

Supporting Information. Additional information on computational models with mobile or bound sulfur atoms; determination of CALNN capping density by FTIR; comments on the DSSP algorithm; construction and quantitative analysis of Ramachandran plots; polar charts of β-structure probability for CALNN and CFGAILSS monolayers; secondary structure analysis of CFGAILSS-capped 10 nm GNP simulated with different starting conditions; comparison of β-structure probability in CFGAILSS-capped 10 nm GNP simulated with the two computational models; distribution of backbone-backbone distances in CALNN-capped 25 nm GNP; temporal change of spatial β-structure distribution; movie of CFGAILSS-capped 10 nm GNP showing secondary structure assignment every ps over the last 100 ps of the 10 ns "production run" in AVI format. This material is available free of charge via the Internet at http://pubs.acs.org/.

Data access statement: The computational data and the custom-written software from this paper are available in an on-line repository of the University of Liverpool

at DOI: 10.17638/datacat.liverpool.ac.uk/184 *[During the peer review process, the data can be accessed with the username 'levypeerreviewer' and the password 'ForestPandaTreetop'; it will be fully open from the date of publication]*

Author Information

Corresponding Authors

rapha@liverpool.ac.uk

m.volk@liverpool.ac.uk

Author Contributions

‡These authors contributed equally.

Notes

The authors declare no competing financial interest.

Acknowledgements

The authors acknowledge A*STAR Computational Resource Centre, the University of Liverpool and ARCHER UK National Supercomputing Service (http://www.archer.ac.uk) for the availability of high-performance computing resources. A.M.D. acknowledges support from EPSRC (DTP studentship). D.P. acknowledges support from A*STAR Joint Council Office (Grant number 14302FG094).

References

(1) Link, S.; El-Sayed, M. A. *Annu. Rev. Phys. Chem.* **2003**, *54*, 331.

(2) Dreaden, E. C.; Alkilany, A. M.; Huang, X.; Murphy, C. J.; El-Sayed, M. A. *Chem. Soc. Rev.* **2012**, *41*, 2740.

(3) Daniel, M.-C.; Astruc, D. *Chem. Rev.* **2004**, *104*, 293.

(4) Häkkinen, H. *Nat. Chem.* **2012**, *4*, 443.

(5) Love, J. C.; Estroff, L. A.; Kriebel, J. K.; Nuzzo, R. G.; Whitesides, G. M. *Chem. Rev.* **2005**, *105*, 1103.

(6) Giersig, M.; Mulvaney, P. *Langmuir* **1993**, *9*, 3408.

(7) Brust, M.; Walker, M.; Bethell, D.; Schiffrin, D. J.; Whyman, R. *J. Chem. Soc. Chem. Commun.* **1994**, 801.

(8) Brust, M.; Fink, J.; Bethell, D.; Schiffrin, D. J.; Kiely, C. *J. Chem. Soc. Chem. Commun.* **1995**, *98*, 1655.

(9) Lévy, R.; Thanh, N. T. K.; Doty, R. C.; Hussain, I.; Nichols, R. J.; Schiffrin, D. J.; Brust, M.; Fernig, D. G. *J. Am. Chem. Soc.* **2004**, *126*, 10076.

(10) Shaw, C. P.; Fernig, D. G.; Lévy, R. *J. Mater. Chem.* **2011**, *21*, 12181.

(11) Fabris, L.; Antonello, S.; Armelao, L.; Donkers, R. L.; Polo, F.; Toniolo, C.; Maran, F. *J. Am. Chem. Soc.* **2006**, *128*, 326.

(12) Rio-Echevarria, I. M.; Tavano, R.; Causin, V.; Papini, E.; Mancin, F.; Moretto, A. *J. Am. Chem. Soc.* **2011**, *133*, 8.

(13) Hautman, J.; Klein, M. L. *J. Chem. Phys.* **1989**, *91*, 4994.

(14) Tupper, K. J.; Brenner, D. W. *Thin Solid Films* **1994**, *253*, 185.

(15) Mahaffy, R.; Bhatia, R.; Garrison, B. J. *J. Phys. Chem. B* **1997**, *101*, 771.

(16) Gerdy, J. J.; Goodard, W. A. *J. Am. Chem. Soc.* **1996**, *118*, 3233.

(17) Iori, F.; Di Felice, R.; Molinari, E.; Corni, S. *J. Comput. Chem.* **2009**, *30*, 1465.

(18) Iori, F.; Corni, S. *J. Comput. Chem.* **2008**, *29*, 1656.

(19) Ghorai, P. K.; Glotzer, S. C. *J. Phys. Chem. C* **2007**, *111*, 15857.

(20) Van Lehn, R. C.; Alexander-Katz, A. *J. Phys. Chem. C* **2013**, *117*, 20104.

(21) Velachi, V.; Bhandary, D.; Singh, J. K.; Cordeiro, M. N. D. S. *J. Phys. Chem. C* **2015**, *119*, 3199.

(22) Fetisov, E. O.; Siepmann, J. I. *J. Phys. Chem. B* **2016**, *120*, 1972.

(23) Duchesne, L.; Wells, G.; Fernig, D. G.; Harris, S. A.; Lévy, R. *Chembiochem* **2008**, *9*, 2127.

(24) Todorova, N.; Chiappini, C.; Mager, M.; Simona, B.; Patel, I. I.; Stevens, M. M.; Yarovsky, I. *Nano Lett.* **2014**, *14*, 5229.

(25) Lee, K. H.; Ytreberg, F. M. *Entropy* **2012**, *14*, 630.

(26) Wright, L. B.; Rodger, P. M.; Corni, S.; Walsh, T. R. *J. Chem. Theory Comput.* **2013**, *9*, 1616.

(27) Shaw, C. P.; Middleton, D. A.; Volk, M.; Lévy, R. *ACS Nano* **2012**, *6*, 1416.

(28) Hess, B.; Kutzner, C.; Van der Spoel, D.; Lindahl, E. *J. Chem. Theory Comput.* **2008**, *4*, 435.

(29) Van Der Spoel, D.; Lindahl, E.; Hess, B.; Groenhof, G.; Mark, A. E.; Berendsen, H. J. C. *J. Comput. Chem.* **2005**, *26*, 1701.

(30) Lindahl, E.; Hess, B.; Spoel, D. van der. *Mol. Model. Annu.* **2001**, *7*, 306.

(31) Berendsen, H. J. C.; van der Spoel, D.; van Drunen, R. *Comput. Phys. Commun.* **1995**, *91*, 43.

(32) Boal, A. K.; Rotello, V. M. *J. Am. Chem. Soc.* **2000**, *122*, 734.

(33) Jadzinsky, P. D.; Calero, G.; Ackerson, C. J.; Bushnell, D. A.; Kornberg, R. D. *Science* **2007**, *318*, 430.

(34) Zhang, J.; Chi, Q.; Nielsen, J. U.; Friis, E. P.; Andersen, J. E. T.; Ulstrup, J. *Langmuir* **2000**, *16*, 7229.

(35) Duchesne, L.; Gentili, D.; Comes-Franchini, M.; Fernig, D. G. *Langmuir* **2008**, *24*, 13572.

(36) Berendsen, H. J. C.; Postma, J. P. M.; van Gunsteren, W. F.; DiNola, A.; Haak, J. R. *J. Chem. Phys.* **1984**, *81*, 3684.

(37) Jorgensen, W. L.; Chandrasekhar, J.; Madura, J. D.; Impey, R. W.; Klein, M. L. *J. Chem. Phys.* **1983**, *79*, 926.

(38) Darden, T.; York, D.; Pedersen, L. *J. Chem. Phys.* **1993**, *98*, 10089.

(39) Hess, B.; Bekker, H.; Berendsen, H. J. C.; Fraaije, J. G. E. M. *J. Comput. Chem.* **1997**, *18*, 1463.

(40) Kabsch, W.; Sander, C. *Biopolymers* **1983**, *22*, 2577.

(41) Humphrey, W.; Dalke, A.; Schulten, K. *J. Mol. Graph.* **1996**, *14*, 33.

(42) Krpetić, Z.; Davidson, A. M.; Volk, M.; Lévy, R.; Brust, M.; Cooper, D. L. *ACS Nano* **2013**, *7*, 8881.

(43) Arrondo, J. L. R.; Muga, A.; Castresana, J.; Goñi, F. M. *Prog. Biophys. Mol. Biol.* **1993**, *59*, 23.

(44) Barth, A.; Zscherp, C. *Q. Rev. Biophys.* **2002**, *35*, 369.

(45) Petty, S. A.; Volk, M. *Phys. Chem. Chem. Phys.* **2004**, *6*, 1022.

(46) Gooding, E. A.; Sharma, S.; Petty, S. A.; Fouts, E. A.; Palmer, C. J.; Nolan, B. E.; Volk, M. *Chem. Phys.* **2013**, *422*, 115.

(47) Chirgadze, Y. N.; Brazhnikov, E. V. *Biopolymers* **1974**, *13*, 1701.

(48) Cowan, P. M.; McGavin, S. *Nature* **1955**, *176*, 501.

(49) Tiffany, M. L.; Krimm, S. *Biopolymers* **1968**, *6*, 1379.

(50) Sreerama, N.; Woody, R. W. *Proteins* **1999**, *36*, 400.

(51) J. Stapley, B.; P. Creamer, T. *Protein Sci.* **1999**, *8*, 587.

(52) Hovmöller, S.; Zhou, T.; Ohlson, T. *Acta Crystallogr. Sect. D Biol. Crystallogr.* **2002**, *58*, 768.

(53) Salemme, F. R. *Prog. Biophys. Mol. Biol.* **1983**, *42*, 95.

(54) Arnott, S.; Dover, S. D. *Acta Crystallogr. Sect. B Struct. Crystallogr. Cryst. Chem.* **1968**, *24*, 599.

(55) Fischer, H.; Polikarpov, I.; Craievich, A. F. *Protein Sci.* **2004**, *13*, 2825.

(56) Mandal, H. S.; Kraatz, H.-B. *J. Am. Chem. Soc.* **2007**, *129*, 6356.

(57) Sawyer, E. B.; Claessen, D.; Gras, S. L.; Perrett, S. *Biochem. Soc. Trans.* **2012**, *40*, 728.

(58) Xu, Y.; Bunagan, M. R.; Tang, J.; Gai, F. *Biochemistry* **2008**, *47*, 2064.

(59) Krejtschi, C.; Huang, R.; Keiderling, T. A.; Hauser, K. *Vib. Spectrosc.* **2008**, *48*, 1.

(60) Turkevich, J.; Stevenson, P. C.; Hillier, J. *Discuss. Faraday Soc.* **1951**, No. 11, 55.

(61) Frens, G. *Nat. Phys. Sci.* **1973**, *241*, 20.

Insert Table of Contents artwork here

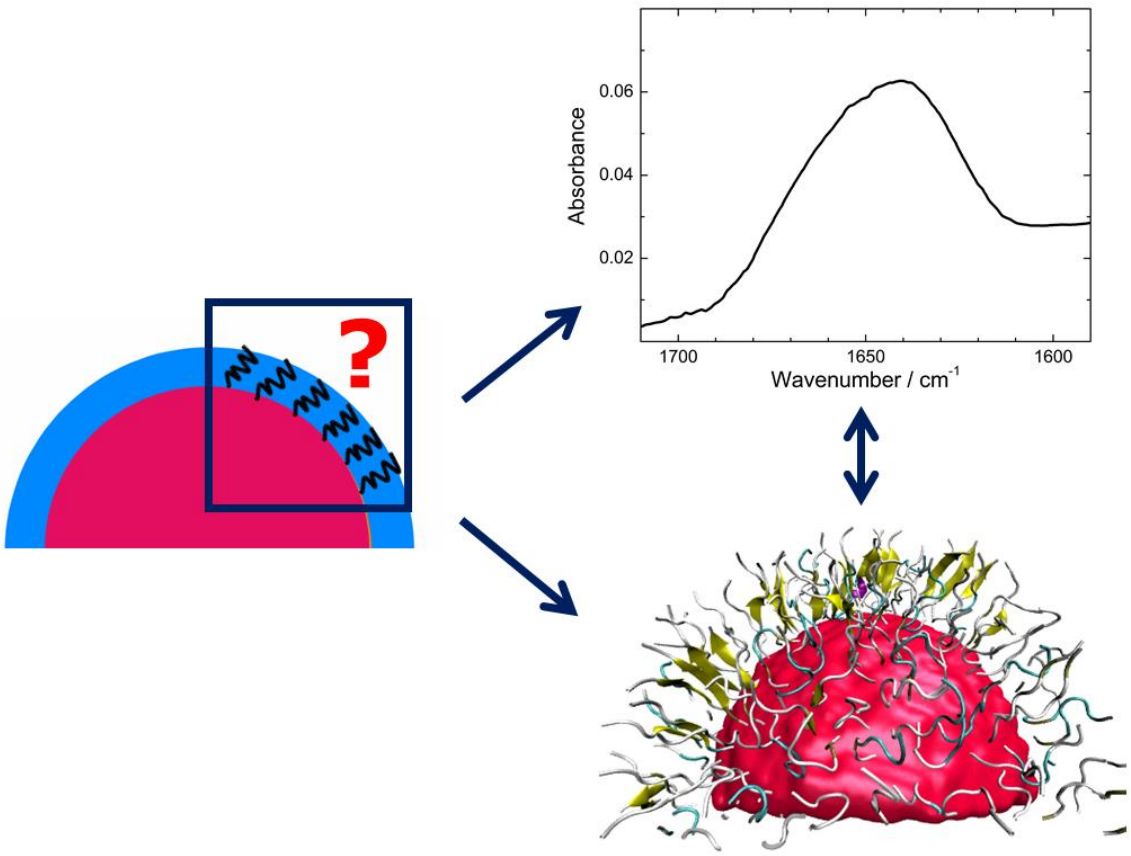

4.3 Supporting Information for: Experimental and Computational Investigation of the Structure of Peptide Monolayers on Gold Nanoparticles

Elena Colangelo,[a,b,c,‡] Qiubo Chen,[c,‡] Adam M. Davidson,[d] David Paramelle,[b] Michael B. Sullivan,[c] Martin Volk,[d,e,*] Raphaël Lévy[a,*]

[a]Institute of Integrative Biology, University of Liverpool, Crown Street, L69 7ZB Liverpool, United Kingdom

[b]Institute of Materials Research and Engineering, A*STAR (Agency for Science, Technology and Research), 2 Fusionopolis Way, #08-03 Innovis, Singapore 138634

[c]Institute of High Performance Computing, A*STAR (Agency for Science, Technology and Research), 1 Fusionopolis Way, #16-16 Connexis North, Singapore 138632

[d]Department of Chemistry, University of Liverpool, Liverpool L69 7ZD, United Kingdom

[e]Surface Science Research Centre, Department of Chemistry, Abercromby Square, University of Liverpool, Liverpool L69 3BX, United Kingdom

‡These authors contributed equally.

*m.volk@liverpool.ac.uk, rapha@liverpool.ac.uk

Table of Contents

S1. Computational Model – Mobile Sulfur Atoms

S1.1 Gold nanoparticle construction

To model the gold nanoparticle, equilibration in an NPT ensemble of gold atoms in a cubic box was first performed. The gold atoms, as per the GolP-CHARMM force field description,[1] were constituted of a real gold atom and a virtual site, each with a mass equal to half the mass of a single gold atom, i.e., 196.97/2 amu, constrained at a distance of 0.07 nm, and called AU and AUC, respectively. AU and AUC are partially charged, i.e., -0.3 and +0.3, respectively, and thus account for the dynamic polarization of the gold surface. After equilibration, the density in the cubic box was 19.14 g/cm^3, in excellent agreement with the density of gold, i.e., 19.3 g/cm^3, validating the accuracy of the force field.

Gold nanoparticles of diameter 5, 10 and 25 nm were then constructed by selecting all gold atoms out of the cubic box for which either the AU or the AUC centre of mass was at a distance from the centre of the box less than 2.5, 5.0 and 12.5 nm, respectively. It is worth noting that during all following simulations the positions of all AU atoms were fixed, whereas the AUC sites were allowed to move within the constraint of 0.07 nm from their AU atom.

The criteria adopted in the construction of the nanoparticles result in a gold surface that is amorphous to account for the fact that there is not yet a force field able to describe gold nanoparticles as multifaceted objects.[2,3] The surface of the resulting nanoparticles is uneven because AUC virtual sites can move. Also, the gold nanoparticles are slightly larger than the stated nominal size, i.e., diameters of 5, 10 and 25 nm, not only because the centre of mass of the AUC virtual sites can move up to 0.14 nm beyond the selected distance from the centre of the nanoparticle, as shown in Fig. S1, but also because the finite extension of the gold atoms (van der Waals radius of 0.2 nm) is ignored during the construction of the nanoparticles. Hence, we argue that the effective radius of the nanoparticles is 0.1-0.2 nm larger than the nominal one.

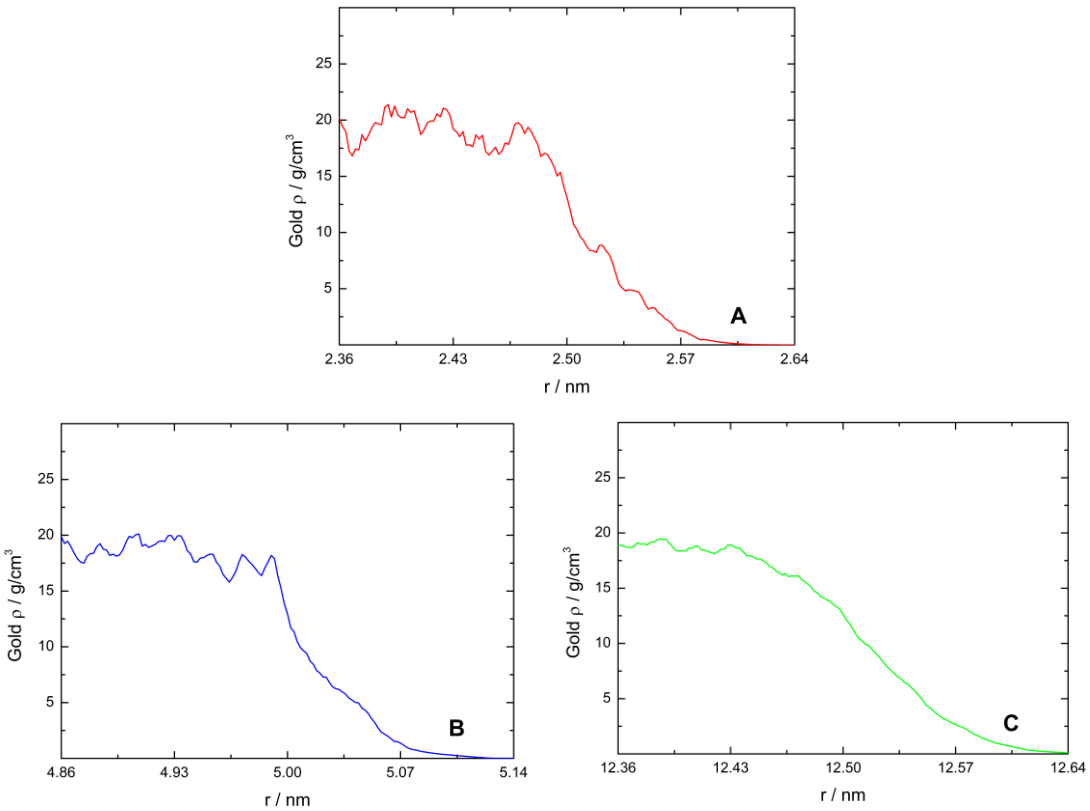

Figure S1. Gold atom mass density from the centre of the simulated 5 (A), 10 (B) and 25 nm (C) diameter gold nanoparticle, averaged over the 10 ns "production run" and 0.02 nm smoothed. All profiles are shown over a 0.28 nm radius range at the edge of the nanoparticle.

S1.2 Distribution of cysteine sulfur and nitrogen atoms

Figure S2 shows the local volume number density profiles of cysteine sulfur and nitrogen atoms against distance from the surface of the nanoparticle, which was calculated from the distance from the center of the nanoparticle by subtracting the nominal nanoparticle radius. Taking into account the above considerations about the uneven gold nanoparticle surface and the fact that the effective nanoparticle radii are 0.1-0.2 nm larger than the nominal ones, it can be seen that after equilibration the sulfur atoms are at a realistic distance from the surface, i.e., within 0.22 – 0.26 nm, as determined by X-ray diffraction analysis for a *p*-mercaptobenzoic acid-capped GNP.[4] It should also be noted that a significant number of sulfur atoms are closer to the nominal nanoparticle surface than expected (significantly less than 0.2 nm). This is due to the fact that the GolP-CHARMM force field describes the gold-sulfur bond mostly by electrostatic interactions, so that a sulfur atom simultaneously interacts with more than one gold atom, which leads to strong binding of the sulfur to the nanoparticle surface without preventing them from moving over the surface, which is an important experimentally observed effect.[5] At the same time, this

leads to sulfur atoms not lying on-top of a single gold atom, but more likely in-between several gold atoms, and thus closer to the nominal surface. This effect had already been described in the original publication of the GolP-CHARMM force field[1] and is readily visible when visualising the structures.

The cysteine nitrogen atoms are found at only slightly larger distances from the nanoparticle surface (dashed lines in Fig. S2), confirming the significant interaction between the charged N-terminus amino groups and the gold atoms, caused by the partial charges of the gold atoms in GolP-CHARMM force field description. This interaction is in good agreement with experimental observations.[6,7]

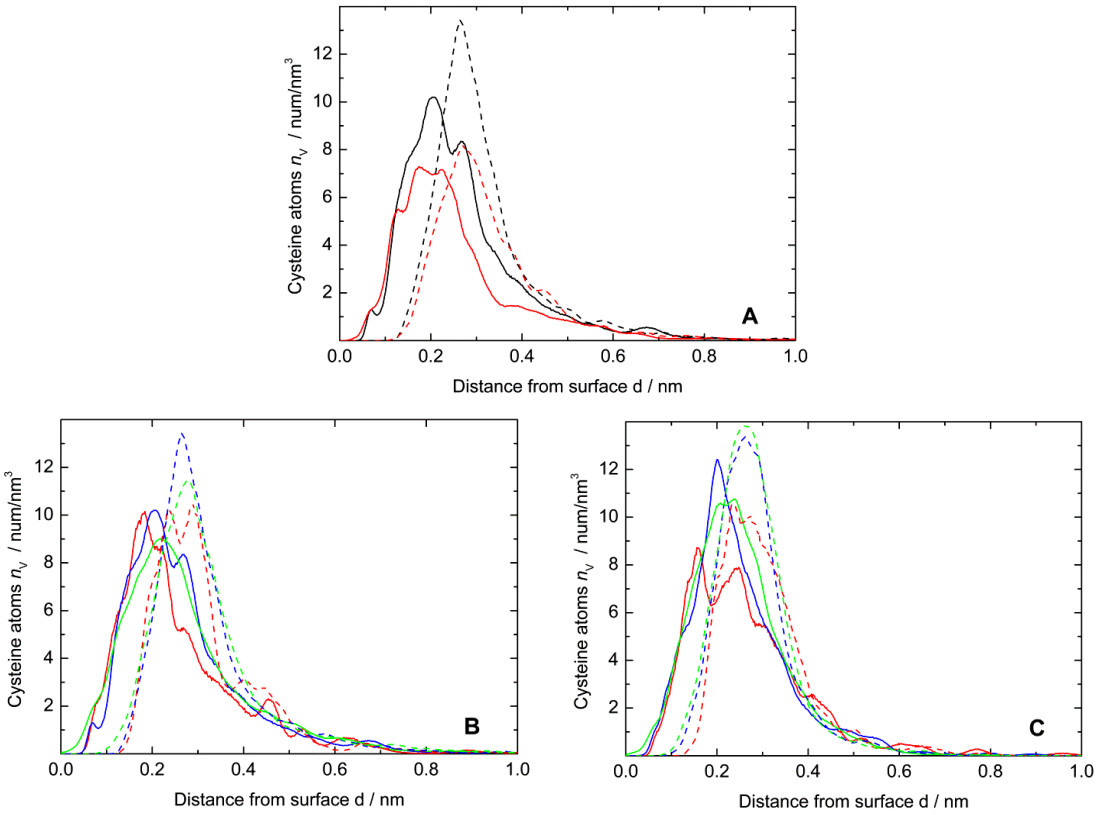

Figure S2. Local volume number density profiles of cysteine sulfur (solid lines) and nitrogen (dashed lines) atoms against the distance from the surface of the nanoparticle of the simulated (A) 10 nm CALNN-capped gold nanoparticle at high (black lines) and low (red lines) capping density, (B) CALNN- and (C) CFGAILSS-capped 5 (red lines), 10 (blue lines) and 25 nm (green lines) gold nanoparticles, averaged over the 10 ns "production run".

S2. Computational Methods – Bound Sulfur Atoms

Molecular dynamics simulations in which the sulphur atoms were bound to the gold nanoparticle, preventing motion over the nanoparticle surface, were performed using the CHARMM[8]-METAL[9] force field.

A gold nanoparticle of diameter 10 nm was modelled with frozen real gold atoms in a face-centered cubic arrangement and mass of 196.97 amu. A linear geometry of CFGAILSS (Cys-Phe-Gly-Ala-Ile-Leu-Ser-Ser) peptide was chosen as starting structure. The peptide, in zwitterionic form, was oriented with the N-terminus toward the gold nanoparticle surface and the C-terminus located radially away from the nanoparticle. The interactions between the real gold atoms and the peptide atoms were described using CHARMM-METAL force field. However, noting that the surface of the gold nanoparticle was not smooth, yet containing various lattice planes, the Cys sulfur atom was covalently bound with bond strength of 106553.4 kJ mol^{-1} nm^{-2} to a virtual site on the gold nanoparticle surface at a distance of 0.25 nm. The virtual sites were evenly placed at the surface nominal edge (i.e. r = 5.0 nm) and frozen during the simulation. In addition, they had zero mass and zero interaction with other atoms.

As for the computational model discussed in the main manuscript, 786 CFGAILSS peptides were roughly equidistantly placed around the 10 nm gold nanoparticle and the structure was placed in a cubic box with length of 17 nm. A number of TIP3P water[10] molecules was added to the box to ensure a water density of ~1 g/cm^3 after full equilibration, then the system was energy-minimized with the steepest descendent method. Consecutive NVT ensembles were then applied using the Berendsen method[11] to couple the temperature of peptides and solvent at 298 K separately. The short-range and long-range neighbor lists had a cut-off at 1.2 and 1.4 nm using the group cut-off scheme and were updated every 20 fs. Long-range electrostatic interactions were treated with the Particle-mesh Ewald method[12] with a Fourier grid spacing of 0.12 nm. The short-range van der Waals interactions were calculated using a switching function between 1.0 and 1.2 nm. A time step of 1 fs was used and periodic boundary conditions were adopted. The simulated system equilibrated in about 10 ns and data were analysed over the subsequent 10 ns production run.

S3. Determination of CALNN Capping Density by FTIR

The capping density of CALNN monolayers on gold nanoparticles was estimated as described previously.[13] Briefly, the gold nanoparticle concentration was determined from the absorbance at the maximum of the plasmon resonance band near 520 nm,[14] using the gold nanoparticle size of 11 nm measured by Differential Centrifugal Sedimentation,[13] whereas the peptide concentration was estimated from the amide I' band area in the unscaled FTIR spectra (Figure S3).

From the UV-Vis spectra a concentration of 2.7 and 3.1 μM for CALNN-capped gold nanoparticles with high and low capping density was calculated, respectively. Considering these similar gold nanoparticle concentrations, the difference in absorbance in the amide I' region (Fig. S3) directly confirms that these nanoparticles, prepared using high and low peptide concentrations during peptide layer formation, respectively, had significantly different peptide capping densities.

For a more quantitative estimate, the amide I' band areas were measured using band fitting of the (unscaled) FTIR spectra in Origin (Microcal).[13] The fit function comprised a linear background and several pseudo-Voigt functions, consisting of the sum of a Gaussian and a Lorentzian band with identical full-width-at-half-maximum (fwhm). For each band, four parameters were allowed to vary freely, namely the band area, position of the band maximum, fwhm and relative contribution of the Gaussian/Lorentzian band. For both samples, two bands were found to be sufficient to yield satisfactory fits in the amide I region, located at ~1640 and ~1660 cm^{-1}, in agreement with expectations for PPII and random coil structures, although an additional band was added to the fit routine to account for the asymmetric carboxylate (COO^-) stretch of the ionized C-terminus (1595 cm^{-1}); the area of this additional band was ignored for the calculation of peptide concentrations. The amide I band areas thus determined were converted to peptide concentration using literature values for the molar band intensities of peptide bonds of the backbone in random coil/PPII conformation[15] and in the asparagine side chain.[16] However, a further correction has to be applied to account for the effects of the so-called surface selection rules which arise from the distortion of external electric fields in the vicinity of a metal surface. Briefly, no tangential electric field component can be present at the metal surface, whereas radial components are significantly enhanced, so that the IR absorbance of vibrations with transition dipole moments oriented radially to a metal nanoparticle are significantly enhanced, whereas the absorbance of vibrations with transition dipole moments parallel to the surface are suppressed. We have previously estimated that for CALNN on 11 nm gold nanoparticles this

effect leads to a reduction of the amide I band intensity by a factor of ~0.78.[13] Taking into account this correction, peptide concentrations of ~2.2 mM and ~1.6 mM for our samples of CALNN-capped gold nanoparticles at high and low capping density, respectively, were estimated from the FTIR spectra shown in Fig. S3. Together with the nanoparticle concentrations given above, these yield capping densities of 2.1 and 1.4 peptides/nm^2.

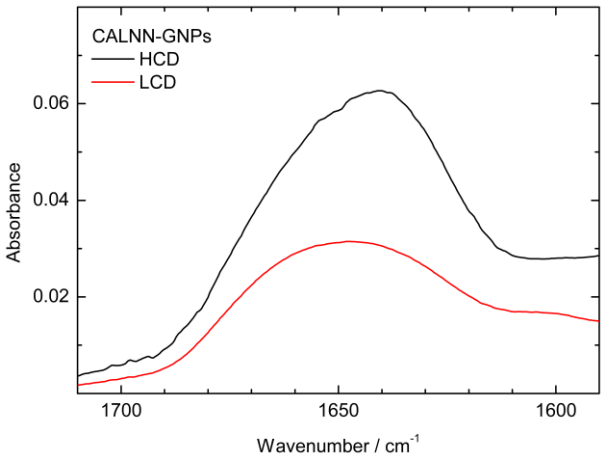

Figure S3. Unscaled FTIR spectra in the amide I' region of 11 nm CALNN-capped gold nanoparticles at high and low capping density (HCD and LCD, respectively).

S4. Comments on the DSSP Algorithm

Briefly, the Dictionary of Protein Secondary Structure (DSSP) algorithm[17] assigns secondary structure motifs mostly based on hydrogen bond patterns, where hydrogen bonds between carbonyl and amide groups are identified based on the electrostatic interaction energies of the partial charges on the carbonyl and amide atoms. In addition, bends are identified as non-hydrogen bonded peptide sections with high curvature.

In Figure 8 of the manuscript, the secondary structure content per amino acid based on DSSP assignment is shown without information on the N-terminal residue and the two final residues at the C-terminus (depicted as grey areas), due to the way DSSP identifies residues and secondary structures. Thus, the C-terminal residue of a peptide is not even identified as a residue because it has no peptide bond to a consecutive residue. Moreover, structure assignment to the *remainder* of the peptide is based on hydrogen bond patterns; however, the DSSP algorithm does not assign any secondary structure to either of the terminal residues. This is because of the way DSSP identifies "turns" and "bridges" which are the basic building blocks of the common secondary structure elements. For

instance, a *n*-turn is identified by a hydrogen bond between the carbonyl CO group of amino acid *i* and the amino NH group of amino acid *i*+*n* (*n*= 3,4,5), but only the residues between *i* and *i*+*n* will be classed as having *turn* structure, whereas the hydrogen-bonded residues *i* and *i*+*n* themselves will be classed as *coil*, unless they are part of other structures. The same holds for inter-strand bridges, where end residues are always classed as *coil*.

Thus, the C-terminal residue is not even shown in the DSSP analysis, whereas the N-terminal residue (cysteine) and the next-to-final C-terminal residue will always be identified as *coil*, the DSSP assignment reflecting the absence of any recognized pattern. We therefore did not include these residues in Fig. 8.

S5. Construction and Quantitative Analysis of Ramachandran Plots

The Ramachandran plots shown in Figures 3 and 6 of the main paper were constructed from the final structures, i.e. the structures at the end of the 10 ns "production run", by calculating the ϕ and ψ angles of the "inner" residues (ALN for CALNN peptide and FGAILS for CFGAILSS peptide - the ϕ angle of the N-terminal residue and the ψ angle of the C-terminal residue are not defined) of all peptides on the nanoparticle surface. For displaying the results, the distribution was smoothed with a 2-dimensional (ϕ and ψ angles) Gaussian with a hwhm-width of 12^{o}.

For a quantitative analysis, some regions of the Ramachandran plot around the positions generally accepted for the ideal structures[18] were assigned to parallel and anti-parallel β-sheets and PPII structures, respectively, as indicated in Fig. S4. Tab. S1 gives the fraction of residues found within these regions for the final structures of all nanoparticles investigated here.

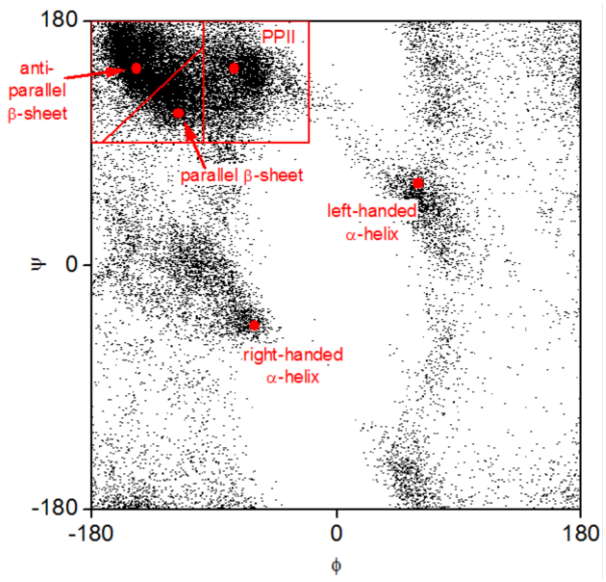

Figure S4. Ramachandran plot of the final structure for a CFGAILSS monolayer on a 25 nm gold nanoparticle; the dots show the ϕ and ψ angles for each residue. The red dots indicate the ϕ and ψ angles of ideal parallel and antiparallel β-sheets, PPII structures, and right and left-handed α-helices, and the solid red lines indicate the regions assigned to parallel and antiparallel β-sheets and PPII structures, respectively, for the analysis provided in Tab. S1.

Table S1. Fraction of residues found in different regions of the Ramachandran plot for different capping layers on gold nanoparticles of different diameters[a]

	d/nm[b]	$\beta_{antiparallel}$	$\beta_{parallel}$	PPII
CALNN (LCD)[c]	10	20.0%	8.9%	19.1%
CALNN (HCD)[c]	5	19.0%	9.1%	20.2%
	10	25.5%	9.5%	18.5%
	25	27.5%	9.6%	18.8%
CFGAILSS	5	21.6%	7.4%	21.2%
	10	24.5%	9.2%	21.9%
	25	30.8%	13.5%	18.3%

[a]antiparallel β-sheet: $\phi \sim$ -147°, $\psi \sim$ +145°,[18] parallel β-sheet: $\phi \sim$ -116°, $\psi \sim$ +112°,[18] PPII: $\phi \sim$ -75°, $\psi \sim$ +145°. See Fig. S4 for the exact definition of the regions of the Ramachandran plot assigned to each structure.

[b]nanoparticle diameter

[c]LCD: low capping density; HCD: high capping density

S6. Polar Charts of β-Structure Probability

S6.1 CFGAILSS monolayers

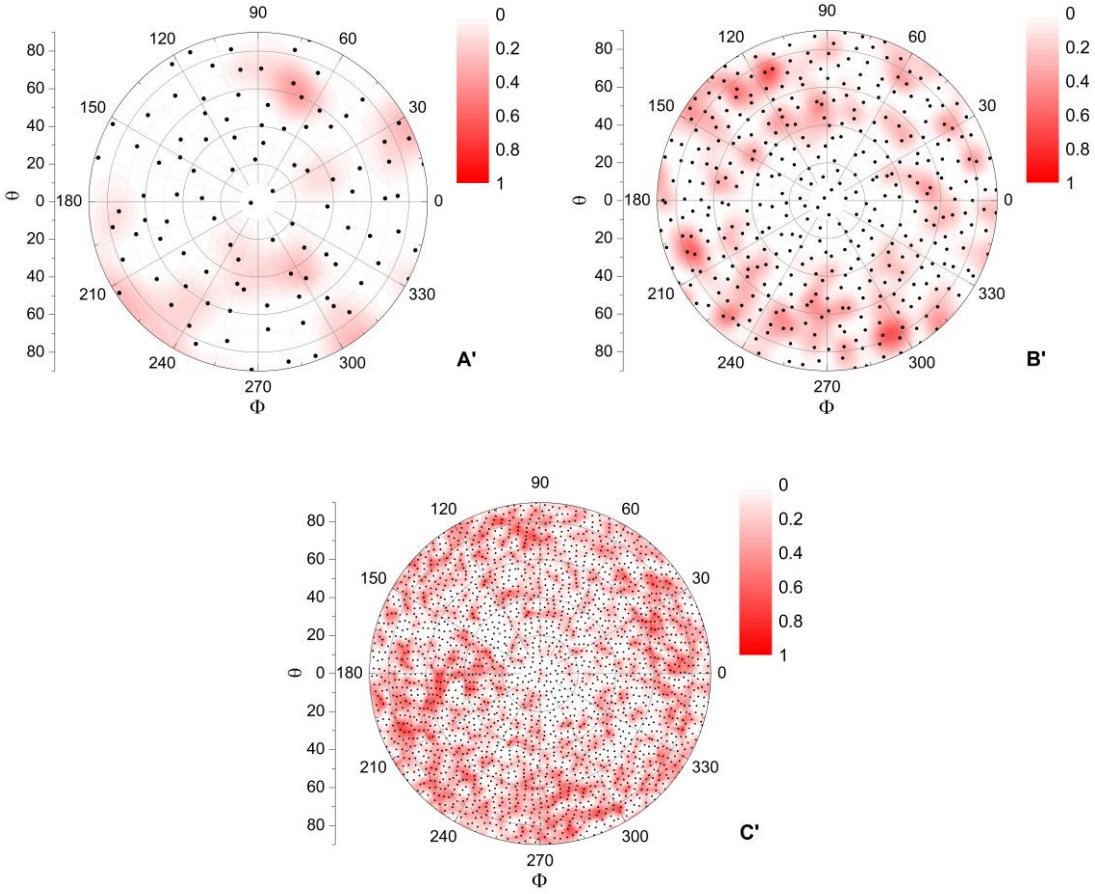

Figure S5. Spatial distribution of β-structure probability, as assessed by DSSP analysis, displayed on polar charts, where Φ and θ indicate the azimuthal and polar angle in spherical coordinates, respectively, for the final structures of CFGAILSS-capped 5 (A'), 10 (B') and 25 nm (C') GNPs; displayed here are the hemispheres opposite to those shown in Figure 10 of the main article. The black points indicate the polar position of the backbone center of mass of each peptide; the color contour shows the local β-structure probability.

S6.2 CALNN monolayers

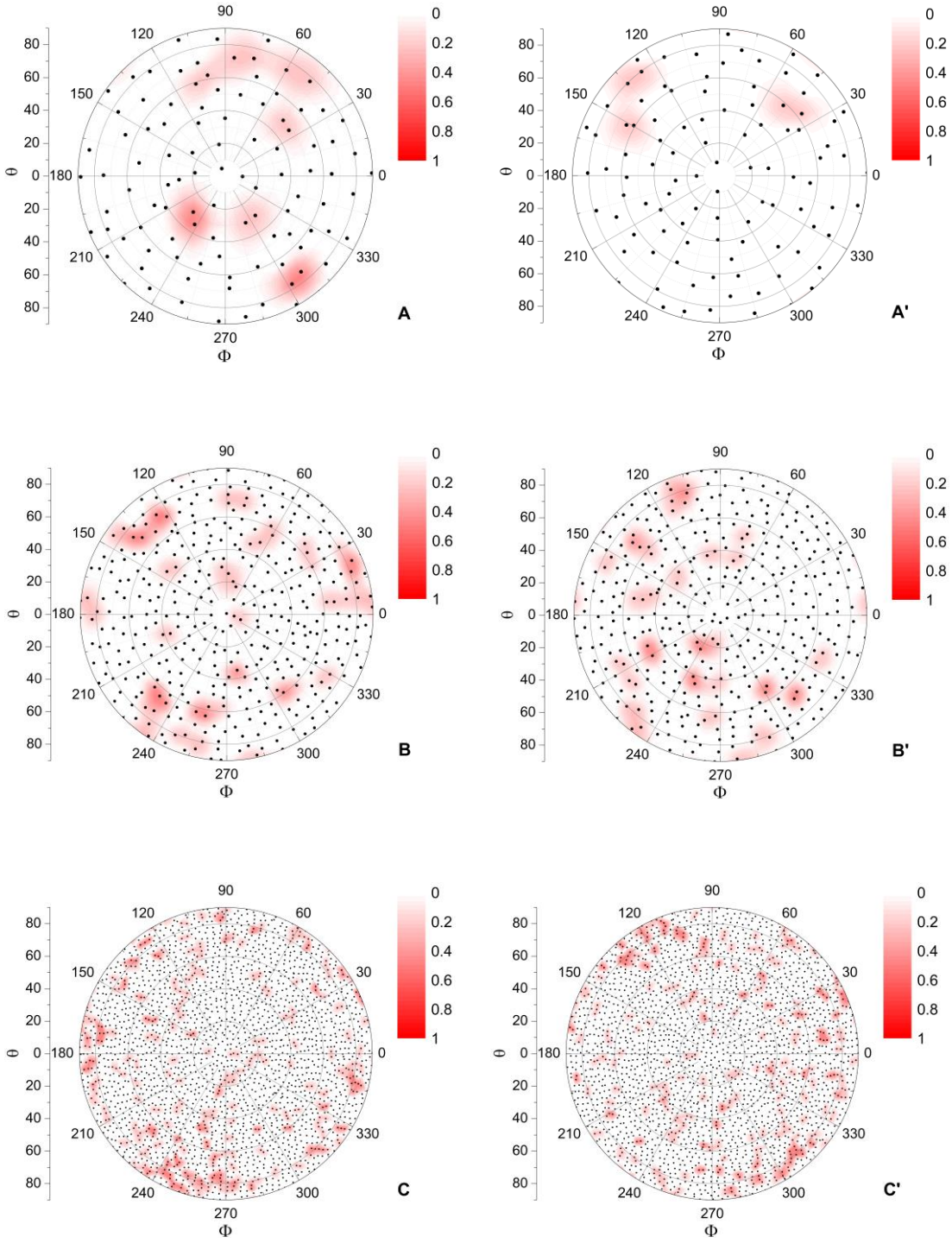

Figure S6. Spatial distribution of β-structure probability, as assessed by DSSP analysis, displayed on polar charts, where Φ and θ indicate the azimuthal and polar angle in spherical coordinates, respectively, for both hemispheres of the final structures of CALNN-capped 5 (A,A'), 10 (B,B') and 25 nm (C,C') GNPs. The black points indicate the polar position of the backbone center of mass of each peptide; the color contour shows the local β-structure probability.

S7. Secondary Structure Analysis of CFGAILSS-Capped 10 nm GNP Simulated with Different Starting Conditions

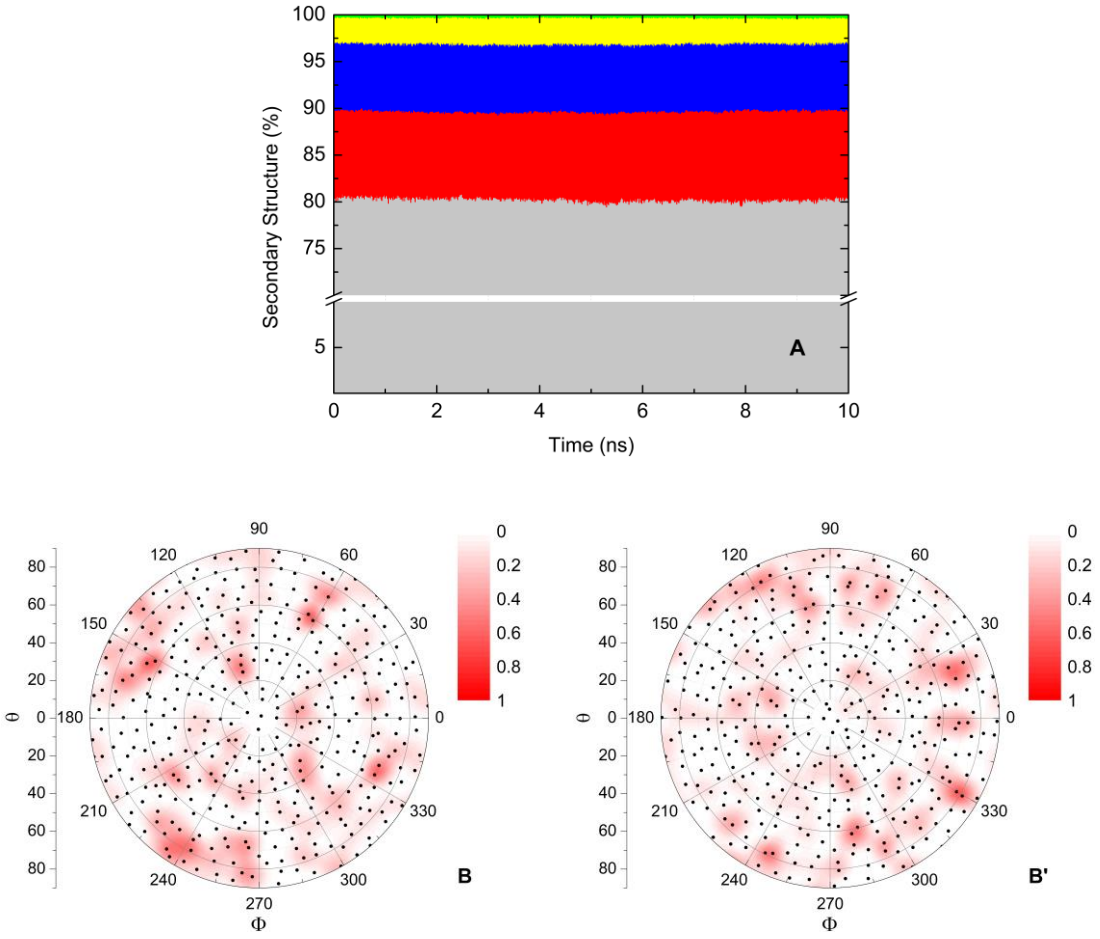

Figure S7. CFGAILSS monolayer on 10 nm GNP simulated with different starting conditions analysed by DSSP: (A) time-evolving secondary structure; secondary structure color code: grey, random coil; red, β-structures (i.e., β-sheet or β-bridge); blue, bend; yellow, turn; green, helix; (B,B') spatial distribution of β-structure probability, displayed on polar charts, where Φ and θ indicate the azimuthal and polar angle in spherical coordinates, respectively, for both hemispheres of the final structure. The black points indicate the polar position of the backbone center of mass of each peptide; the color contour shows the local β-structure probability.

S8. Comparison of β-Structure Probability in CFGAILSS-Capped 10 nm GNP Simulated with the Two Computational Models

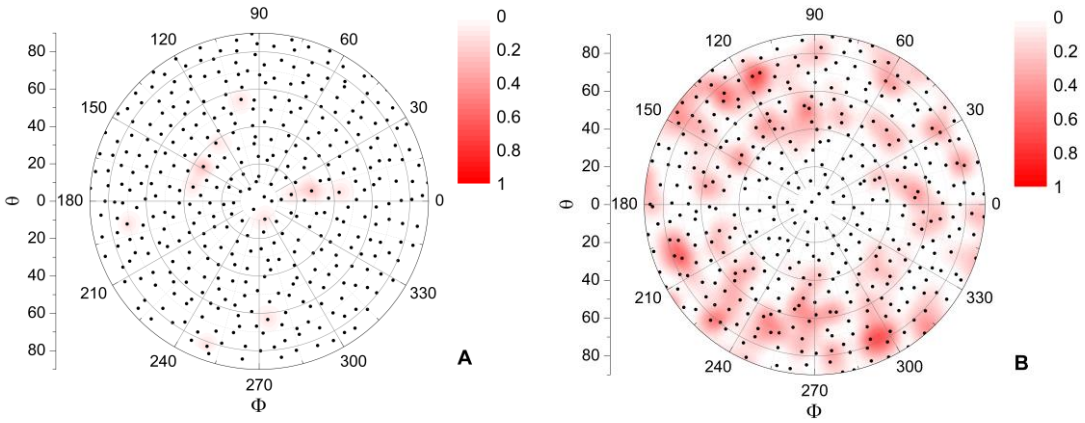

Figure S8. Spatial distribution of β-structure probability, as assessed by DSSP analysis, displayed on polar charts, where Φ and θ indicate the azimuthal and polar angle in spherical coordinates, respectively, for one hemisphere of the final structures of CFGAILSS-capped 10 nm GNPs simulated with the computational model using bound (A) or mobile (B) sulfur atoms. The black points indicate the polar position of the backbone center of mass of each peptide; the color contour shows the local β-structure probability.

S9. Distribution of Backbone-Backbone Distances in CALNN-Capped 25 nm GNP

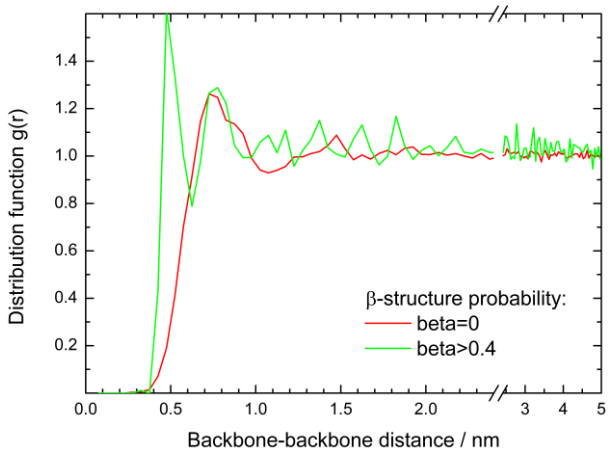

Figure S9. Radial distribution functions of the backbone-backbone distances for peptides with different β-structure probabilities in a CALNN-capped 25 nm GNP; the profiles are the result of averaging over two equilibrated structures.

S10. Temporal Change of Spatial β-Structure Distribution

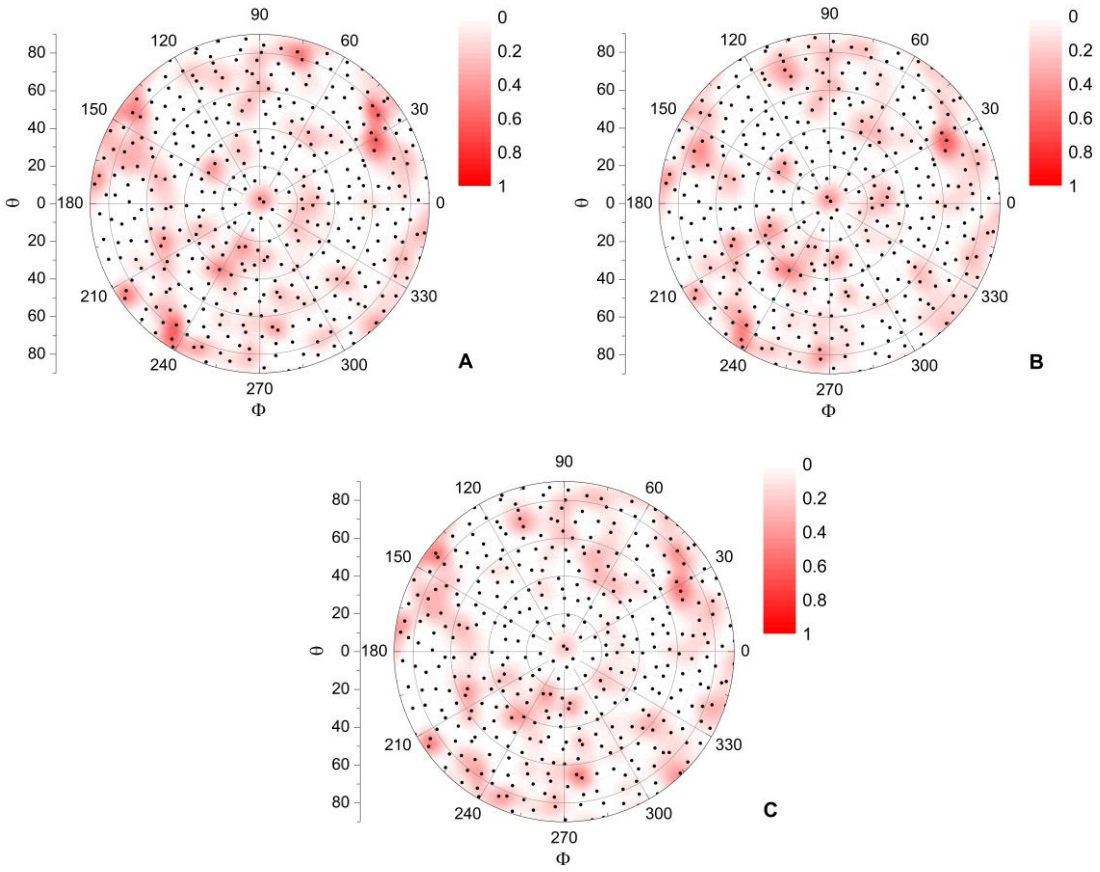

Figure S10. Spatial distribution of β-structure probability, as assessed by DSSP analysis, displayed on polar charts, where Φ and θ indicate the azimuthal and polar angle in spherical coordinates, respectively, for a hemisphere of CFGAILSS-capped 10 nm GNP at 0 (A), 5 (B) and 10 (C) ns over the production run. The black points indicate the polar position of the backbone center of mass of each peptide; the color contour shows the local β-structure probability.

References

(1) Wright, L. B.; Rodger, P. M.; Corni, S.; Walsh, T. R. *J. Chem. Theory Comput.* **2013**, *9*, 1616.

(2) Marks, L. D. *Reports Prog. Phys.* **1994**, *57*, 603.

(3) Roduner, E. *Chem. Soc. Rev.* **2006**, *35*, 583.

(4) Jadzinsky, P. D.; Calero, G.; Ackerson, C. J.; Bushnell, D. A.; Kornberg, R. D. *Science* **2007**, *318*, 430.

(5) Boal, A. K.; Rotello, V. M. *J. Am. Chem. Soc.* **2000**, *122*, 734.

(6) Zhang, J.; Chi, Q.; Nielsen, J. U.; Friis, E. P.; Andersen, J. E. T.; Ulstrup, J. *Langmuir* **2000**, *16*, 7229.

(7) Lévy, R.; Thanh, N. T. K.; Doty, R. C.; Hussain, I.; Nichols, R. J.; Schiffrin, D. J.; Brust, M.; Fernig, D. G. *J. Am. Chem. Soc.* **2004**, *126*, 10076.

(8) MacKerell, A. D.; Bashford, D.; Bellott, M.; Dunbrack, R. L.; Evanseck, J. D.; Field, M. J.; Fischer, S.; Gao, J.; Guo, H.; Ha, S.; Joseph-McCarthy, D.; Kuchnir, L.; Kuczera, K.; Lau, F. T.; Mattos, C.; Michnick, S.; Ngo, T.; Nguyen, D. T.; Prodhom, B.; Reiher, W. E.; Roux, B.; Schlenkrich, M.; Smith, J. C.; Stote, R.; Straub, J.; Watanabe, M.; Wiórkiewicz-Kuczera, J.; Yin, D.; Karplus, M. *J. Phys. Chem. B* **1998**, *102*, 3586.

(9) Heinz, H.; Vaia, R. A.; Farmer, B. L.; Naik, R. R. *J. Phys. Chem. C* **2008**, *112*, 17281.

(10) Jorgensen, W. L.; Chandrasekhar, J.; Madura, J. D.; Impey, R. W.; Klein, M. L. *J. Chem. Phys.* **1983**, *79*, 926.

(11) Berendsen, H. J. C.; Postma, J. P. M.; van Gunsteren, W. F.; DiNola, A.; Haak, J. R. *J. Chem. Phys.* **1984**, *81*, 3684.

(12) Darden, T.; York, D.; Pedersen, L. *J. Chem. Phys.* **1993**, *98*, 10089.

(13) Krpetić, Z.; Davidson, A. M.; Volk, M.; Lévy, R.; Brust, M.; Cooper, D. L. *ACS Nano* **2013**, *7*, 8881.

(14) Haiss, W.; Thanh, N. T. K.; Aveyard, J.; Fernig, D. G. *Anal. Chem.* **2007**, *79*, 4215.

(15) Chirgadze, Y. N.; Shestopalov, B. V.; Venyaminov, S. Y. *Biopolymers* **1973**, *12*, 1337.

(16) Chirgadze, Y. N.; Fedorov, O. V.; Trushina, N. P. *Biopolymers* **1975**, *14*, 679.

(17) Kabsch, W.; Sander, C. *Biopolymers* **1983**, *22*, 2577.

(18) Salemme, F. R. *Prog. Biophys. Mol. Biol.* **1983**, *42*, 95.

CHAPTER 5

CONCLUSIONS AND PERSPECTIVES

In this body of work, the three approaches reported are connected by the thread of providing tools to elucidate the structure and organization of peptide self-assembled monolayers on gold nanoparticles.

Whilst the photo-activable benzophenone-containing peptides did not provide insights into the mixed monolayer's molecular organization and compactness, we have shown, as also previously reported in the literature,[1,2] that LDI-MS and FTIR techniques allow characterizing the composition of the capping layer at the gold nanoparticles surface. Moreover, while Yan et al. focused on GNPs capped by alkane thiols,[1] in Chapter 2 we have demonstrated the successful use of LDI-MS to analyse peptide self-assembled monolayers on GNPs and potentially answer the question of ligands proximity and segregation on the gold surface.

Fluorescence measurements have revealed that the accessibility of a specific site within a self-assembled monolayer is extremely sensitive to the exact position and surrounding environment. Thus, these findings, as well as the methodology adopted, can be relevant to the design of further functional peptides. One potential other application would be to use the functional group to indirectly probe its surrounding environment and thus, have some indirect evidence of the self-assembled monolayer's structure at the gold nanoparticles surface.

The molecular dynamics computational model for peptide self-assembled monolayers on gold nanoparticles, validated by the remarkable agreement with experimental results, could not only be used to predict the structure of peptide monolayers at different capping densities on gold nanoparticles of different sizes, thus helping in the design of new bio-nanomaterials, but also be combined to experimental findings, in order to obtain deeper insights into the monolayer's structure and organization at the molecular level.

Moreover, considering the depth and richness of the data sets, we decided to share the data thinking that further information could be extracted by other scientists.

In conclusion, from this body of work it appears clear that not only a combination of several techniques, but also a combination of several approaches is needed to draw a compelling picture of the nano-systems investigated. For instance, in the same way the computational model described provided insights into features that could not have been assessed experimentally, such as the peptides' arrangement within secondary structure domains on GNPs, other computational investigations can be foreseen to shed light into the phase separation and conformation of ligands on nanoparticles. Such elucidation is essential to envision controlling the structure and organization of ligand monolayers and hence, designing nanoscale building blocks with well-defined structural and (bio)-physicochemical properties, which could potentially self-organize into more complex nanomaterials from a "bottom-up" approach. With more development, peptide-capped GNPs have the potential to organize in protein-like objects via a "bottom-up" approach, taking inspiration from the self-organization and self-assembly, leading to the tertiary and quaternary structure, of proteins.

References

(1) Yan, B.; Zhu, Z. J.; Miranda, O. R.; Chompoosor, A.; Rotello, V. M.; Vachet, R. W. Laser Desorption/ionization Mass Spectrometry Analysis of Monolayer-Protected Gold Nanoparticles. *Anal. Bioanal. Chem.* **2010**, *396*, 1025–1035.

(2) Krpetić, Z.; Davidson, A. M.; Volk, M.; Lévy, R.; Brust, M.; Cooper, D. L. High-Resolution Sizing of Monolayer-Protected Gold Clusters by Differential Centrifugal Sedimentation. *ACS Nano* **2013**, *7*, 8881–8890.